Study of the Gasdynamic Mirror (GDM) Propulsion System

by

Ricky Tang

A dissertation submitted in partial fulfillment
of the requirements for the degree of
Doctor of Philosophy
(Aerospace Engineering)
in the University of Michigan
2011

Doctoral Committee:

Professor Alec D. Gallimore, Co-Chair
Professor Emeritus Terry Kammash, Co-Chair
Associate Professor John E. Foster
Lecturer Timothy B. Smith

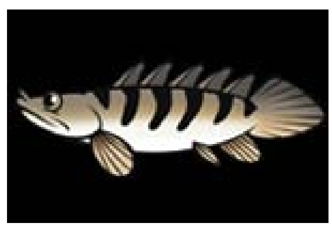

Acknowledgements

Finally, here we are. When I first began this document, I decided that I would save this section for last, to mark the end (or close to it anyway) of the writing process. And as I am writing this, I am reminded of all the guidance and support I received throughout the years, without which this thesis would not have been possible.

I would like to begin by thanking my advisors, Professors Alec Gallimore and Terry Kammash. It has been my honor and privilege to work under them. They have offered me great academic freedom while at the same time providing me with the necessary guidance. I met Professor Kammash during my graduate school tenure when I took his advanced space propulsion class, and it was there that I first learned of the concept of the gasdynamic mirror. I am grateful for the opportunity to begin working with him and Reisz Engineers on the project later. Under his guidance, it eventually evolved into my dissertation topic. And even though he is technically retired, he decided to take me on as a student and serve as my co-chair, and for this I shall be ever grateful. I met Professor Gallimore in the undergraduate propulsion course here at the University of Michigan. It was then that I became interested in the field of propulsion, especially space propulsion. Later, I had the pleasure of taking other classes with him, and it was an amazing experience every time. With his guidance during my time here at U of M, I learned about research, and with his advice and support, I was able to devise an experiment to complement other aspects of my research. Even though it took some time and trial-and-error before I got the setup working, he was nothing but supportive throughout the entire process. And I shall forever be grateful for this and other things.

I also would like to thank other members of my dissertation committee, Professors Tim Smith and John Foster. Tim has been incredibly helpful since I joined PEPL. He has always given me insightful hints and tidbits on how to work more efficiently and safely around the lab, and his expertise has served me well on many occasions. Professor Foster has always made himself available to answer my questions while I was trying to set up my microwave source and work out the kinks in the overall design. Without his expertise and advice, this would not have been possible.

Within the Aerospace Engineering department, there are various people I would like to give special thanks to. Professor Bram van Leer, I am deeply grateful for your help and everything you have done for me over the years. Suzanne Smith, thanks for always being there to help me order stuff. Denise Phelps, you have always been extremely helpful in making sure everything is squared away and taken care of so I have one thing less to worry about. Within the Nuclear Engineering department, I would like to give special thanks to Peggy Gramer and Shannon Thomas for always being there to handle all the paperwork and administrative stuff and working with the Aerospace Engineering staff to make sure everything was in order.

Support for this research came from various sources. First I would like to acknowledge the NASA GSRP for offering me a fellowship, and I would like to thank NASA MSFC and Dr. Bill Emrich for serving as my fellowship sponsor. At this juncture, I would also like to thank Dr. Jonathan Jones from NASA MSFC, Dr. Jerry Brainerd and Mr. Al Reisz from Reisz Engineers for their help during my visit to MSFC.

I learned a lot about microwave source operation while I was there, which helped me tremendously when I was trying to build my own setup here at PEPL. I would also like to acknowledge Reisz Engineers for their financial support while I was working with them and Professor Kammash on their GDM project under the NASA STTR program. Finally, additional funding came from the Rackham Graduate School and various GSI positions within the Aerospace Engineering department.

I have had the pleasure to work with a group of incredibly brilliant students and researchers at PEPL and EDA. Kristina Lemmer, Sonca Nguyen, Bailo Ngom, Bryan Reid, Prashant Patel, Pete Peterson, and Dean Massey, thank y'all over the years. Sonca, thanks for showing me the ropes around the lab. Kristina, thanks for helping me locate your micro-RPA…almost two years after you left. I would also like to thank the current PEPL students: Kimberly Trent (for helping me debug the motion tables while you were on vacation), Adam Shabshelowitz (for lending me your magnets and taking the time to switch over the endcaps, which made this thesis possible), Laura Spencer (because you also needed a microwave power supply, you saved me the trouble of trying to build one out of a microwave oven which probably wouldn't work out quite so well), Tom Liu and Robbie Lobbia (for both of your insightful ideas and suggestions, and sorry Robbie that I have yet to make it to your movie nights), Rohit Shastry and Ray Liang (for helping me with the diagnostics), Roland Florenz (for lending a sympathetic ear when I needed to vent and all the help during my setup/testing, I am deeply grateful), and David Huang, Mike McDonald, Chris Durot, and Mike Sekerak for the help around the lab.

On a personal note, I would like to express my gratitude to my family. I'd like to thank my mom, my dad and my aunt for their love over the years. You give me the

freedom to pursue my dreams, and I could not have done this without your unconditional support and sacrifices. I'd also like to thank my brother for keeping me company all these years at school. Last but certainly not least, I thank my grandparents, who are no longer with us but continue to watch over us. I also must thank my fish for giving me the much needed distraction all these years; there is nothing like staring into the tanks and watching them swim around or just chilling there. And of course all of our puppies, past and present, that never fail to put a smile on my face; they truly are man's best friend.

Finally, I would like to give thanks to all the friends I've made over the years who not only keep me sane, but also give me a life outside of research. First, I'd like to thank the fish crew, in particular Solomon and Double D, who understand this obsession as well as I do. Next but not least, I'd like to thank the UM Taekwondo club for giving me some of the most joyous and memorable moments. Naji, Jacque, Ryan, James, Makiko, Laurie, Matt, Kristen, Laura, Jen, Denar, Aaron, Sadegh, and all the rest of the gang (I apologize I couldn't list everyone since the list would be too long), thank you so very much. From after-practice dinners to tournaments to stinking up the racquetball court for the dance squad, it has been a great bonding experience. As you say, Naji, years from now, these are the times we will remember.

So, to end this with a line from one of the best animes,

"See you space cowboy…"

Table of Contents

List of Figures

List of Tables

Nomenclature

Symbols

A_0	Mirror throat area
A_c	Central region area in GDM
A_p	Langmuir probe tip surface area
A_s	Sheath area
B	Magnetic field strength
B_c	Central magnetic field strength
B_m	Mirror magnetic field strength
$\vec{B}_0$	Applied magnetic field vector
B_0	Magnetic field strength in vacuum
B_p	Magnetic field strength in plasma
B_{pc}	Central magnetic field strength in plasma
B_{pm}	Mirror magnetic field strength in plasma
c_{μ}	Number of catalyzed D-T fusion per negative muon
dE/dx	Antiproton energy loss per unit path
dp/dx	Annihilation per unit length
D_e	Electron diffusion coefficient
D_{ij}	Ion diffusion coefficient
$\vec{E}$	Electric field
$\vec{E}_1$	Electric field (polarization) vector of electromagnetic wave
E	Electric field strength; Particle energy

E_0	Initial energy
E_{ch}	Energy carried by charged particles per fusion reaction
E_f	Energy release per fusion reaction
E_{in}	Injection energy
E_{Le}	Average electron escape energy
E_{Lij}	Average ion escape energy
E_{LiD}, E_{LiT}	Average ion escape energy at direct converter/thrusting end of GDM
$\overline{E}_\alpha$	Mean kinetic energy of confined alpha particles
E_α	Alpha particle energy, 3.5 MeV
F	Fraction of charged particles to direct converter
f	Fraction of antiproton annihilated after penetrating a distance x
f_{ii}, f_{ie}	Fraction of injection energy to ions/electrons
$f_{\alpha i}, f_{\alpha e}$	Fraction of alpha energy to ions/electrons
I_e	Electron current
I_i	Ion current
$I_{i,sat}$	Ion saturation current
I_{sp}	Specific impulse
K_n	Knudsen number
$\vec{k}$	Wave propagation vector
k	Density profile length scale; Wave vector magnitude
L	Plasma length
$\dot{m}$	Propellant mass flow rate
m	Particle mass
m_0	Rocket wet mass
m_e	Electron mass
m_f	Rocket dry mass

m_i , M_i	Ion mass
m_{inc}	Mass of incident particle
$m_{\bar{p}}$	Antiproton mass
m_p	Proton mass
m_{prop}	Propellant mass
m_α	Mass of alpha particle
N	Index of refraction
N_α	Number density of confined alpha particles
n	Plasma number density
n_e	Electron number density
n_i	Ion number density
$n_{i,OML}$	OML ion number density
$n_{i,TS}$	Thin-sheath ion number density
n_{inc}	Number density of incident particle
$n_{\bar{p}}$	Antiproton number density
$n_\alpha(E)$	Alpha particle energy distribution function
n_μ	Negative muon number density
P_a	Auxiliary power
P_c	Charged particle power
P_D	Direct converter power density
$P_{DT/DHe^3/DD}$	Fusion power density for D-T/D-He^3/D-D
P_f	Fusion power
P_G	Gross electric power
P_i	Injected power
P_{in}	Input power
P_n	Neutron power

P_{net}	Net electric power
P_r	Radiative (Bremsstrahlung and synchrotron) power
P_T	Thrust power; Thrust power density
P_α	Portion of fusion power to alpha particles per unit volume
$p(E)$	Antiproton annihilation as a function of energy
Q	Gain factor
R	Mirror ratio; Ratio of antiproton density to electron density
R'	Ratio of incident particle density to electron density
R_D	Plasma mirror ratio at direct converter end of GDM
R_p	Plasma mirror ratio
R_T	Plasma mirror ratio at thrusting end of GDM
r_c	Cyclotron radius
r_m	Mirror throat radius
r_p	Plasma radius; Langmuir probe tip radius
S	Ion injection rate per unit volume
T	Thrust; Plasma temperature
T_e	Electron temperature
T_i	Ion temperature
u_e	Propellant exhaust velocity
v	Particle velocity
$v_c\left(v_{c\perp}, v_{c//}\right)$	Particle velocity at the center of the device (corresponding perpendicular and parallel component to B field)
v_e, v_i	Electron/Ion velocity
$v_m\left(v_{m\perp}, v_{m//}\right)$	Particle velocity at the mirror throat (corresponding perpendicular and parallel component to B field)
v_{th}	Particle thermal velocity
$v_\perp$	Perpendicular (to B field) component of particle velocity
$v_{//}$	Parallel (to B field) component of particle velocity

V_B	Langmuir probe bias voltage
$\dot{W}$	Propellant weight flow rate
W	Total kinetic energy of particle
W_c	Total kinetic energy of particle at the center of the device
W_{ie}	Energy exchange rate from ions to electrons
$W_m\left(W_{m\perp}\right)$	Total kinetic energy of particle at the mirror throat (corresponding component perpendicular to B field)
$W_\perp$	Perpendicular (to B field) component of particle kinetic energy
$W_{//}$	Parallel (to B field) component of particle kinetic energy
Z	Particle charge number
ΔE	Energy increment
ΔV	Velocity increment
α	Loss cone angle
β	Ratio of plasma pressure to magnetic field pressure
Γ_{ej}, Γ_{ij}	Total electron/ion flux
γ_{ej}, γ_{ij}	Monoenergetic electron/ion flux
$\ln \Lambda$	Coulomb logarithm
ϕ	Ambipolar potential
η_D	Direct converter efficiency
η_i	Injector efficiency
η_T	Thrust efficiency
η_t	Thermal converter efficiency
λ, λ_{mfp}	Collision mean free path
λ_D	Debye length
μ	Magnetic moment
μ_e	Electron mobility
μ_i	Ion mobility

ν_{ei}	Electron ion collision frequency
σ	Collisional cross section
$\langle \sigma v \rangle$	Fusion reaction rate, averaged over Maxwellian distribution
τ	Confinement time; Heating time
τ_{ei}	Electron ion thermalization time
τ_H	Total heating time
τ_{ij}, τ_j	Confinement time; i.e. particle loss rate
τ_D, τ_T	Confinement time for direct converter/thrusting end of GDM
τ_μ	Muon lifetime
ω	Wave frequency
ω_{ce}, ω_{ci}	Electron/ion cyclotron frequency
ω_L	Left-hand circularly polarized wave cutoff frequency
ω_p	Plasma frequency
ω_{pe}, ω_{pi}	Electron/ion plasma frequency
ω_R	Right-hand circularly polarized wave cutoff frequency
ω_{UH}	Upper hybrid frequency

Constants

c	Speed of light, 3×10^{8} m/s
g	Gravitational acceleration at Earth's surface, 9.81 m/s^2
k, k_B	Boltzmann constant, 1.381×10^{-23} J/K
q, e	Elementary charge, 1.6022×10^{-19} C
r_0	Classical electron radius, 2.82x10^{-13} cm
α	Fine structure constant, 1/137
ε_0	Vacuum permittivity, 8.854×10^{-12} F/m
μ_0	Vacuum permeability, $4\pi\times10^{-7}$ H/m

Abstract

The gasdynamic mirror (GDM) is a magnetic confinement device that has been proposed as a concept which could form the basis of a spacecraft propulsion system by accelerating its ionized propellant without the endurance limitations imposed by electrodes. The geometry of the GDM is that of a simple magnetic mirror, with a magnetic field configuration resembling that of a meridional nozzle where the fluid flow velocity is everywhere parallel to the magnetic field lines. The magnetic field strength is stronger at the ends, called mirrors, than at the center, producing a turning force that helps confine the plasma ions long enough for heating before being ejected through one of the mirrors that serves as a magnetic nozzle. Gasdynamic mirrors differ from most other mirror-type plasma confinement schemes in that they have a larger aspect ratio and higher plasma density in order to achieve better confinement and provide plasma stability without the complicated equipment required by low-aspect ratio, low-density mirror machines.

This work aims to study and characterize the plasma dynamics inside the GDM through both modeling and experiments. A physics-based model was developed that models the plasma dynamics inside an asymmetric GDM, where the two mirrors have different magnetic field strengths to bias the flow of ions to one end in order to produce thrust. The model allows the prediction of plasma characteristics such as the plasma

temperature, confinement time, particle energy and the magnitude of the ambipolar potential, as well as system attributes such as the system length and mass.

For the experimental study, a proof-of-concept model of the GDM was built that was driven by a 2.45 GHz microwave source. Ionization comes from electron cyclotron resonance heating (ECRH). Langmuir probe measurements provide 2D maps of the plasma density and temperature inside the GDM. A maximum ion density exceeding 10^{17} m^{-3} and an electron temperature between 4 and 5 eV were found in the central section of the GDM. The density profile suggested ion trapping near the exit mirror, and the plasma potential results hinted at the presence of an acceleration zone in the vicinity of the exit mirror.

Chapter 1

Introduction

1.1 Motivation

Spacecraft propulsion dictates mission feasibility. The chemical rocket is the most traditional form of spacecraft propulsion and still comprises the majority of the systems used today. In a chemical rocket, the energy source is the propellant enthalpy; i.e. the energy stored in the chemical bonds of the propellants [1]. Combustion between a fuel and an oxidizer releases this energy, which is then converted to directed kinetic energy via a convergent-divergent nozzle. However, the issue with chemical propulsion is the inherently limited energy that is available in the propellant chemical bonds, which limits the efficiency and performance of chemical rockets. This limitation is reflected in the system's relatively low specific impulse (I_{sp}), or equivalently its exhaust velocity.

Specific impulse is defined as the thrust generated per unit weight of propellant consumed over time and is a measure of the propellant use efficiency [2]. Low I_{sp} translates to large propellant requirements that can significantly limit the payload mass, and in the worst case result in missions that are not practical or possible for chemical rockets no matter how large or how many stages the vehicle has. Generally, it is not practical to perform a space mission where the mission ΔV is several (e.g. two to three) times the propulsion system's exhaust velocity [3].

Electric propulsion (EP) has the advantage of not being limited by propellant chemistry. Energy is supplied by an external power source, and the propellant is accelerated via electrical heating, electrostatic forces, or electromagnetic forces to produce thrust [4]. Systems such as ion and Hall thrusters have enabled missions that would otherwise be impractical or undesirable with traditional chemical rocket systems. Since an EP system can operate continuously at high I_{sp}, it can propel a spacecraft to very high velocity over a period of time.

Although currently the most common applications for EP are low-thrust operations such as station-keeping, orbit-raising and attitude control for satellites, its capability has been demonstrated in various space missions [5,6]. High-ΔV missions that EP is well suited for include comet encounter, sample return, outer solar system and deep-space robotic missions, due to its much higher specific impulse, which significantly reduces the amount of propellant needed. However, due to its inherently low thrust, current EP systems cannot adequately enable highly energetic or high-mass, deep-space missions, such as fast sample returns from the outer planets and the Kuiper belt. EP systems are also inadequate for future cargo or piloted missions to Mars, where a fast transit time is desirable. Such missions require a high-thrust, high-I_{sp} system.

The magnetoplamadynamic (MPD) thruster has been suggested as a candidate for those sorts of missions, due to its potential for high thrust and high I_{sp}. However, electrode erosion (as high as 0.2 μg/C [7]) has been one of the major obstacles in the development of MPD thrusters. Designs with no electrodes therefore have the potential to offer longer life and increased reliability, as well as enabling a higher power density.

The VASIMR®, proposed by Dr. Franklin Chang Diaz, is one such design [8,9]. It has the ability to vary both thrust and specific impulse. VASIMR uses a helicon source to create a plasma, which is heated via ion cyclotron heating (ICH) and subsequently ejected through a magnetic nozzle.

The gasdynamic mirror (GDM) propulsion system, the topic of this dissertation, is another concept with the potential to address these highly energetic missions, while circumventing the issue of electrode erosion. The GDM, like VASIMR, is also an electrodeless design. In addition, the GDM can form the basis of an electric plasma thruster as well as a nuclear propulsion system and thereby has the potential to carry out missions in both the near and very far future.

1.2 Rocket Performance

The above can be put into more quantitative terms by considering Tsiolkovsky's rocket equation [10]:

$$\frac{m_f}{m_0} = \frac{m_0 - m_{prop}}{m_0} = e^{-\Delta V / u_e} \tag{1.1}$$

The mass fraction on the left is the ratio of the initial rocket wet mass m_0 includes the final dry mass m_f (which includes the payload) and the propellant mass m_{prop}. ΔV is mission-dependent and denotes the necessary rocket velocity change to perform the mission, while u_e represents the effective exhaust velocity of the propellant. Equation (1.1) therefore says that in order to accelerate an appreciable amount of rocket dry mass, the propellant exhaust velocity needs to be on the same order as the mission ΔV requirement.

The specific impulse (I_{sp}), introduced in the previous section, is an important measure of rocket performance, along with the rocket thrust. The specific impulse is defined as the amount of thrust produced per weight of propellant consumed per unit time, or the impulse $\int Tdt$ per unit of propellant weight. Assuming neglible pressure thrust, the thrust is given by

$$T = \dot{m}u_e \tag{1.2}$$

The specific impulse is then given by

$$I_{sp} = \frac{T}{\dot{W}} = \frac{T}{\dot{m}g} = \frac{u_e}{g} \tag{1.3}$$

where T is the thrust, $\dot{m}$ is the propellant mass flow rate, and g is gravitational acceleration at the Earth's surface; i.e. 9.81 m/s^2. Inserting Eq. (1.3) into Eq. (1.1) and rearranging gives the following expression for the propellant mass fraction:

$$\frac{m_{prop}}{m_0} = 1 - \exp\left(-\frac{\Delta V}{gI_{sp}}\right) \tag{1.4}$$

Equation (1.4) implies that for a given mission ΔV, a higher specific impulse requires less propellant mass, resulting in more available mass for the rocket payload. Alternatively, for a given payload mass and a given amount of propellant, a higher specific impulse translates into a higher ΔV that can be achieved, meaning more demanding missions can be performed.

While the best chemical rockets such as the Space Shuttle main engine can produce about 450 seconds of specific impulse [10], a high-power xenon Hall thruster can have an I_{sp} above 3000 seconds. A high-power ion thruster (such as the HiPEP) can produce even higher I_{sp}, as much as 9000 seconds [11].

The benefits and necessity of a high specific impulse system for future exploration missions become apparent when one considers a one-way trip to Mars without the use of gravity assist or aerobraking. A propulsion system I_{sp} of 300 s would require almost 86% of its initial mass as propellant for this mission, versus 18% for 3000 s I_{sp} [12].

Electric propulsion systems require input power to operate. Unlike a chemical rocket, their performance is not limited by the working fluid, but rather by the amount of power available. The thrust efficiency of an EP system is given by the following:

$$\eta_T = \frac{P_T}{P_{in}} = \frac{\dot{m}u_e^2}{2P_{in}} \tag{1.5}$$

Using Eqs. (1.2) and (1.3), we can rewrite the thrust efficiency to obtain the thrust-to-power ratio of an EP system:

$$\frac{T}{P_{in}} = \frac{2\eta_T}{u_e} = \frac{2\eta_T}{gI_{sp}} \tag{1.6}$$

Equation (1.6) shows that $T \propto I_{sp}^{-1}$ for constant input power, leading to the inherent tradeoff between thrust and specific impulse. The operating conditions are then set by the mission requirements.

As noted at the start of this section, since high specific impulse is often necessary for many future exploration missions with demanding ΔV requirements, Eq. (1.6) implies that the system thrust will be small for a given amount of power. The intrinsically low thrust of EP systems, such as ion and Hall thrusters, sometimes leads to longer spacecraft trip times, which may or may not be acceptable depending on the mission. When human planetary exploration missions finally become feasible, trip times must especially be kept as short as possible to limit the physical health risks of space travel due to extended exposure to space level radiation and weightlessness, as well as psychological effects from long-term confinement [13]. These highly-energetic missions therefore require not only high specific impulse for propellant efficiency, but also high thrust to shorten mission times.

Equation (1.6) shows that higher thrust can be achieved by increasing the input power, for a given specific impulse. Since higher power densities are generally achievable in plasmas through magnetic rather than electrostatic interactions; i.e. $B^2/(2\mu_0) >> (\varepsilon_0/2)E^2$ for realizable fields [14], the magnetoplasmadynamic (MPD) thruster has been regarded as a leading candidate for future missions such as heavy-lift Mars transfer due to its high power capabilities. However, in practice, MPD thruster efficiencies have not exceeded 35% using noble gases even at megawatt power levels [14]. These inefficiencies, along with electrode erosion problems, have significantly slowed MPD thruster development.

1.3 Magnetic Mirror

The improved lifetime and reliability of an electrodeless plasma thruster can be highly desirable for long duration missions. In addition, for relatively fast solar system exploration, a vehicle with specific power of at least 10 kW/kg and specific impulses in the range of 10,000 to 100,000 seconds [15] would also be desirable. Other high ΔV or high-mass missions include human transit between planets and cargo missions with large payload mass fraction. Fusion-based propulsion systems would be quite suitable for these sorts of missions if they could be built in reasonable sizes.

One of the oldest thermonuclear plasma confinement concepts is the magnetic mirror. Mirror-type fusion devices use an open magnetic field line configuration called a magnetic well to confine the plasma. Confinement in these devices is achieved due to constraints on particle motion imposed by the conservation of magnetic moment and energy.

In an effort to develop mirror machines for terrestrial fusion power, extensive physics research and engineering development have been carried out for the past several decades. The earliest mirror machines were built at the Lawrence Livermore Laboratories in the late 1950’s and early 1960’s to demonstrate stable plasma confinement [16]. Results of these experiments were less than satisfactory; a magnetohydrodynamic (MHD) instability known as the flute instability proved to be a major problem. This instability arises as a result of the unfavorable (concave toward the plasma) curvature of the magnetic field lines near the magnetic mirrors. It is the pressure-driven version of the Rayleigh-Taylor instability and is so called because the perturbation of a quasi-cylindrical plasma surface resembles a fluted Greek column. The plasma “flutes” extend radially outward from the central plasma column, quickly striking the containment wall. Contact with the wall causes the plasma to cool, as well as leading to the loss of confinement. One way to suppress the MHD flute instability involves the installation of current-carrying Ioffe bars [17] to create a “minimum B” configuration, where only “favorable” (i.e., convex toward the plasma) B-field curvature exists within the mirror.

Another type of instability found in a magnetic mirror is called the loss cone microinstability. This instability is caused by asymmetry in the plasma ion velocity space due to the loss of particles with velocity space components falling within the mirror loss cone. Though not as dangerous as the MHD modes, these microinstabilities can lead to local turbulence and enhanced diffusion across the magnetic field lines, resulting in short confinement times and excessive plasma loss.

Although these microinstabilities are difficult to control, theoretical analyses suggest that they would not pose any major problem in a larger machine. As a result, larger mirror machines have been built and tested, culminating in the construction of what would have been the largest mirror experiment in the U.S., the Mirror Fusion Test Facility mod B (MFTF-B). MFTF-B was completed in the early 1980's, but the project was canceled in favor of the Tokamak Fusion Test Reactor (TFTR) and was unfortunately never operated [16]. The linear mirror concept has been largely abandoned as a potential terrestrial power reactor because the Q value (ratio of energy out to energy in) only slightly exceeded unity, as opposed to >15-20 that is generally desired for power generation. As a result, the traditional mirror configurations were never able to produce an attractive power gain factor.

Although unacceptable as a terrestrial reactor, this Q value is quite adequate from a propulsion standpoint; as long as Q is greater than one, the fusion reaction will be self-sustaining. Another quality that lends the magnetic mirror naturally to propulsion applications is that the open magnetic field line configuration allows for easy ejection of the plasma to produce thrust. Indeed, the open-ended geometry, which inevitably allows plasma ions to escape and carry with them sufficient energy to render the simple mirror unacceptable as a terrestrial reactor, is exactly what is desired in a propulsion system.

1.4 Aim of Project

A type of mirror machine, called the gasdynamic mirror or GDM, was proposed by Kammash [18] as a propulsion device. My research aims at understanding and modeling the plasma dynamics inside the GDM and validating the concept as a propulsion system. Theoretical and experimental efforts are carried out to characterize the plasma inside the GDM, which include the following:

- A physics-based model was formulated to describe the plasma dynamics inside an asymmetric gasdynamic mirror. Magnetic field asymmetry, where the mirror ratios for the two ends of the mirror are different, is necessary to bias the flow of plasma through one end of the machine to produce thrust. The model provides a set of governing equations that can be solved to obtain the plasma parameters inside the GDM.
- A computer code was written based on the above physics-based model. Since the set of equations are interdependent, pure analytic solutions are not possible. For a given set of input parameters, the code solves for a set of self-consistent values for the various quantities. The outputs from the code allow us to predict the plasma parameters inside the GDM, such as the particle energies, confinement times, and magnitude of the ambipolar potential, as well as physical parameters such as the plasma length and mass of the system.
- Experiments were carried out to study the plasma dynamics inside the GDM. The main goal here is to characterize the plasma and compare with computational results where applicable. To achieve that goal, a microwave plasma source was built for our proof-of-concept model of the GDM. In this source, energy is coupled to the plasma electrons via electron cyclotron resonance heating (ECRH). Although the GDM was initially proposed as a fusion propulsion system, this demonstrated that the GDM can also function as a plasma thruster driven by an external power source, using

technologies that have largely been developed. Thus, the GDM is a versatile concept with the ability to satisfy both near term and future missions depending on available technologies.

1.5 Dissertation Overview

Chapter 2 describes the gasdynamic mirror propulsion concept and investigates its use as a fusion and a fission propulsion scheme. Numerical performance results will be presented. Chapter 3 presents the derivation of the physics model governing the plasma dynamics inside the GDM, followed by a description of the GDM code. Chapter 4 describes our ECR-GDM experiments, the design of our GDM and the microwave plasma source, and the experimental setup and diagnostics. Chapter 5 presents the experimental results. Chapter 6 concludes the research and recommends future work.

Chapter 2

The Gasdynamic Mirror Concept

The gasdynamic mirror [19] is a type of magnetic mirror confinement system with a large aspect ratio (length >> radius) operating at a high plasma density to overcome the major instability modes found in classical mirror machines. In contrast to a classical mirror for which the ion mean free path is much greater than the system length, the ion confinement time in a gasdynamic mirror is a much stronger function of the mirror ratio. Thus, increasing the mirror ratio in a gasdynamic mirror produces a much greater effect on plasma confinement, and as such gasdynamic mirrors are usually operated at high mirror ratios.

2.1 Linear (Mirror) Confinement Scheme

There are two main types of magnetic confinement schemes: linear and toroidal. The tokamak is an example of a toroidal device. As the name suggests, these devices form a torus or donut shape, and therefore are also called closed-ended devices. Due to the shape, end losses are eliminated, and good confinement can be achieved. However, due to difficulty in extracting the plasma efficiently into a directed exhaust because of the closed field lines, toroidal devices do not lend themselves readily to propulsion applications.

Linear devices or mirrors are also called open-ended devices. In their simplest form, they consist of an open cylinder around which current-carrying conductors are wrapped. This produces an axial magnetic field in the enclosed space similar to that found inside a solenoid. Unlike a simple solenoid, the magnetic field is designed to be stronger at the ends of the machine than at the center. This enhanced field strength can be achieved by increasing the current through the end coils or by having more coils per unit length. The result is a field geometry that confines particles between the ends. These ends are referred to as mirrors since they reflect charged particles in much the same way as optical mirrors reflect light, preventing them from escaping too quickly. Figure 2.1 illustrates the geometry of a simple mirror.

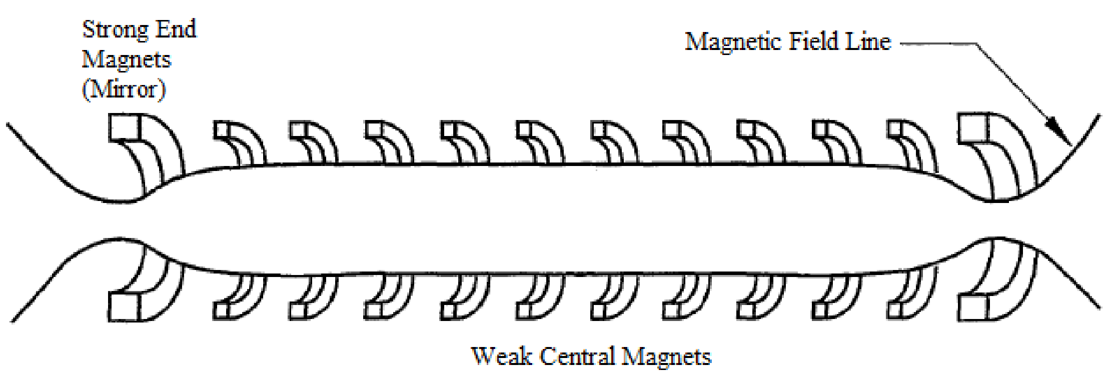

Figure 2.1. A simple mirror geometry.

The basis for magnetic mirror confinement is the adiabatic invariance of the magnetic moment μ; i.e. the magnetic moment of a gyrating particle is a constant of motion. This can be expressed as follows as the particle travels along the magnetic field,

$$\mu = \frac{W_\perp}{B} = \frac{\frac{1}{2} m v_{m\perp}^2}{B_m} = \frac{\frac{1}{2} m v_{c\perp}^2}{B_c} \tag{2.1}$$

where $W_\perp$ is the kinetic energy of the particle perpendicular to the field line, and the subscripts *m* and *c* denote the corresponding values at the mirror and center, respectively. Furthermore, conservation of energy states that, in the absence (or until) interactions with other particles, the total particle energy is also constant; i.e.,

$$W = \frac{1}{2}mv^2 = W_\perp + W_{//} = \frac{1}{2}mv_\perp^2 + \frac{1}{2}mv_{//}^2 = \text{constant} \tag{2.2}$$

and its energy is simply exchanged between the parallel and perpendicular components as it gyrates along the magnetic field.

Rearranging Eq. (2.1), we obtain an equation relating the magnetic field and the perpendicular particle velocity at the mirror and the center,

$$R \equiv \frac{B_m}{B_c} = \frac{v_{m\perp}^2}{v_{c\perp}^2} \tag{2.3}$$

where we have also defined the ratio of the mirror to center magnetic field strengths as the mirror ratio *R*.

Going back to Eq. (2.2), since μ is constant, it follows that

$$W_{//} = W - \mu B \tag{2.4}$$

Equation (2.4) therefore states that as the magnetic field becomes stronger (i.e. as the particle moves towards the mirror) the parallel component of its kinetic energy decreases until μB becomes large enough to equal the particle's total kinetic energy *W* leaving zero parallel energy, at which point all of its kinetic energy is in the cyclotron motion and the particle gets reflected. This happens at both mirrors, and the particle becomes confined. However, for high-energy particles and those particles whose orbits are along the field lines at or near the centerline of the device (such that their magnetic moments are small), μB never increases enough to cancel *W* even at the mirrors. As a result, these particles escape confinement unless the mirror field is made so large that it is effectively infinite. Prevent leakage this way would not be technologically possible. Thus, a magnetic mirror is inherently lossy, although there are ways to reduce the energy loss, such as direct conversion of the energy of the escaping particles into electricity [20]. While the leakiness of the magnetic mirror is not desirable for a fusion reactor, it is precisely what is needed for a propulsion system.

In order to put the above observation more quantitatively, consider a particle with a magnetic moment such that the maximum B field at the mirror B_m is just enough to deflect it. Since the total kinetic energy is conserved, we can write the following at the deflection point, where $v_{m//} = 0$:

$$\begin{aligned} & W = W_c = W_m = W_{m\perp} \\ & \Rightarrow v_c^2 = v_{c\perp}^2 + v_{c//}^2 = v_m^2 = v_{m\perp}^2 \end{aligned} \tag{2.5}$$

Combining Eqs. (2.3) and Eq. (2.5), we have

$$R = \frac{v_{m\perp}^2}{v_{c\perp}^2} = \frac{v_c^2}{v_{c\perp}^2} = \frac{1}{\sin^2 \alpha} \tag{2.6}$$

where

$$\sin \alpha = \frac{v_{c\perp}}{v_c} \tag{2.7}$$

defines α to be the angle the particle velocity vector makes with the local magnetic field line, as depicted in Figure 2.2. Hence, the minimum $v_{c\perp}/v_c$ a particle must possess for confinement is related to the magnetic fields as follows:

$$\sin \alpha = \frac{1}{\sqrt{R}} = \sqrt{\frac{B_c}{B_m}} \tag{2.8}$$

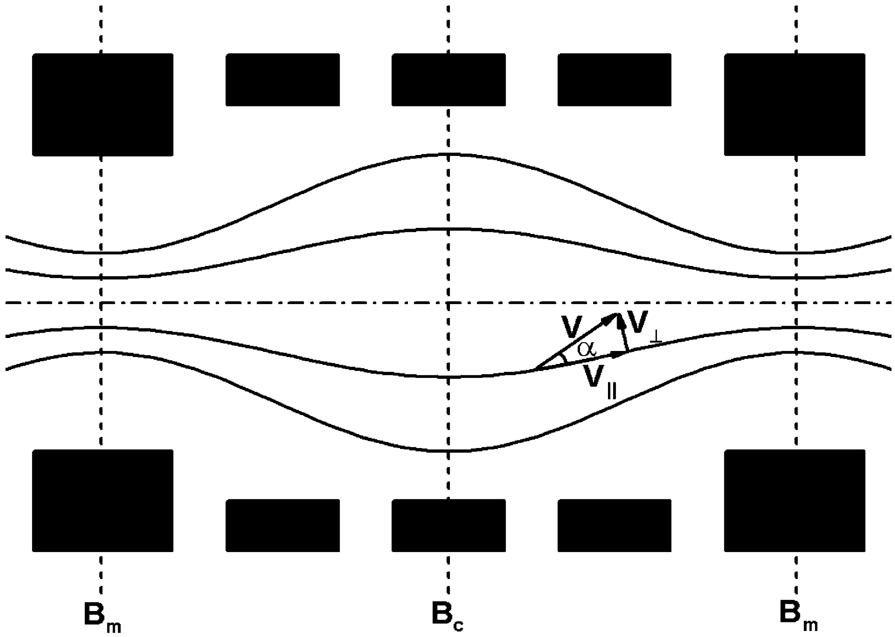

Figure 2.2. Particle motion in a magnetic mirror showing the loss cone angle α [16]. The curves are the magnetic field lines.

The angle α is known as the loss cone angle. Any plasma particle whose phase space velocity yields an angle greater than α will be trapped by the magnetic mirror, while those yielding an angle smaller than α will escape.

Equation (2.8) also shows that increasing the mirror ratio has the effect of decreasing the loss cone angle, thus allowing more particles to be trapped and leading to good confinement. Good confinement is desirable not only when using a magnetic mirror as a fusion reactor, but also when using a magnetic mirror as a propulsion system. In both cases, good confinement allows the plasma to be retained long enough for sufficient heating. Of course, good confinement needs to be balanced against the function of a propulsion system, which is to eject the plasma and produce thrust. Another benefit of high mirror ratios, as will be shown, is that the length (and hence the mass) necessary to achieve self-sustained fusion is inversely proportionally to the mirror ratio.

2.2 The GDM Propulsion Concept

2.2.1 Confinement Principle

Simply put, the GDM propulsion concept is a magnetic mirror confinement system in which the propellant (in the form of a dense plasma) is confined for a period of time while being heated, and then accelerated through the magnetic nozzle to produce thrust. Unlike a classical collisionless mirror fusion reactor, where a plasma ion will traverse the device several times before undergoing a scattering collision [20], the underlying confinement principle of the GDM is based on a different premise. In a GDM reactor, the plasma density and temperature will have such values as to make the ion-ion collision mean free path much shorter than the characteristic dimension of the system; e.g. the plasma length. Under these conditions the plasma behaves like a fluid, and its escape from the system would be analogous to the flow of a gas into vacuum from a vessel with a hole. Therefore, its confinement properties can be described by gasdynamic laws (hence, its name).

A first order expression for the confinement time in the GDM can be obtained by considering the plasma flux leaving the system and the total number of particles in the system. Figure 2.3 illustrates this geometry.

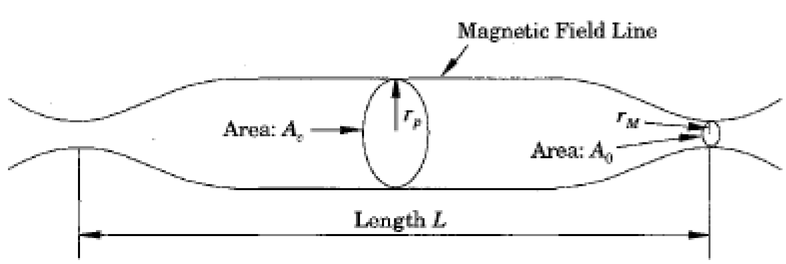

Figure 2.3. Schematic of the gasdynamic mirror propulsion system [18].

The plasma flux across each mirror is given by $A_0 n v_{th}$, where A_0 is the mirror throat area, n is the plasma density and v_{th} is the particle thermal velocity. The total number of particles in the system with a central region area A_c and plasma length L is approximately $A_c L n$.

Consider an equal mirror ratio for both mirrors; in this case, the plasma flux across each mirror is on average the same. The time it takes all the particles to escape, namely the confinement time, can be expressed by the following,

$$\tau = \frac{A_c n L}{2A_0 n v_{th}} = \frac{A_c L}{2A_0 v_{th}} = \frac{r_p^2 L}{2r_m^2 v_{th}} \tag{2.9}$$

where r_p and r_m are the plasma radius and mirror throat radius, respectively. Now if we assume these radii are on the same order as the ion gyroradius in the corresponding region, then we have the following,

$$\frac{r_p^2}{r_m^2} \sim \left(\frac{m v_{c\perp}}{q B_{pc}}\right)^2 \left(\frac{q B_{pm}}{m v_{m\perp}}\right)^2 = \frac{v_{c\perp}^2}{v_{m\perp}^2}\frac{B_{pm}^2}{B_{pc}^2} = \frac{1}{R_p}\left(R_p\right)^2 = R_p \tag{2.10}$$

where B_p denotes the magnetic field in the plasma and R_p is the mirror ratio seen by the plasma; i.e. the plasma mirror ratio. These are different from the vacuum quantities since the presence of plasma reduces the apparent magnetic field and are related to their vacuum counterparts by

$$R_p = \frac{R_0}{\sqrt{1-\beta}} \tag{2.11}$$

$$B_p = B_0\sqrt{1-\beta} \tag{2.12}$$

where the subscript *0* denotes vacuum quantities, and β is defined as the ratio of plasma pressure to confining magnetic field pressure.

$$\beta = \frac{\sum nT}{B_0^2 / 2\mu_0} \tag{2.13}$$

Note that in deriving Eq. (2.10), we invoked Eq. (2.3) to relate the perpendicular particle velocity and the magnetic field, namely $v_{c\perp}^2 / v_{m\perp}^2 = B_{pc} / B_{pm}$. Therefore, the confinement time in Eq. (2.9) becomes

$$\tau = \frac{R_p L}{2v_{th}} \tag{2.14}$$

Unlike the classical mirror for which the confinement time is only a logarithmic function of the mirror ratio, the GDM has a stronger (linear) dependence. Thus, increasing the mirror ratio in the GDM provides a much greater increase in the confinement time than in a classical mirror.

Recall that Eq. (2.14) is derived based on the condition that the plasma is collisional, and confinement requires that the ion collision mean free path λ be much shorter than the plasma length; i.e. $\lambda << L$. However, as it turns out, when $R_p >> 1$, it is sufficient that $\lambda / R_p << L$ in order to satisfy confinement. The term λ / R_p can be thought of as an effective mean free path against scattering through an angle on the order of the loss cone angle.

2.2.2 Basic Principle of Operation

The magnetic configuration of the GDM is that of a simple magnetic mirror in which the magnetic field strength at the ends (mirrors) is stronger than that in the central section. For a system with a large aspect ratio (ratio of plasma length to radius), the system is azimuthally symmetric and the fluid flow velocity is everywhere parallel to the magnetic field lines. The GDM will be magnetically asymmetric (i.e. with asymmetric mirror ratios) in order to bias the flow of plasma toward the thrusting end of the device. The stronger field at the mirrors allows the plasma to be confined well enough to be heated by injected power before escaping through the weaker mirror, which acts as a magnetic nozzle to produce thrust.

Once propellant gas is injected into the GDM and a plasma is formed, electrons will escape rapidly through the mirrors due to their small mass, leaving behind an excess of positive charge that manifests itself in a positive electrostatic potential. The electric field generated by this ambipolar potential accelerates the ions while slowing down the electrons, causing both species to leave the mirror at equal rates and producing a charge-neutral propellant beam. Because hotter electrons produce a larger electrostatic potentials (and hence a larger accelerating electric fields), the proposed system can be viewed as a variable specific impulse device if the input power can be adjusted to match the mission requirements. Moreover, asymmetry in the mirror ratios controls the propellant mass flow through the magnetic nozzle, and thus the GDM has the potential to function as a variable thrust system as well.

2.2.3 Plasma Stability Concerns

As alluded to in Section 1.3, there are two main plasma instability modes that can arise in a magnetic mirror device. The first is a MHD mode called the flute instability. In an effort to suppress this, the GDM thruster will have a large aspect ratio (length-to-diameter ratio) in order to minimize the unfavorable (concave toward the plasma) curvature of the magnetic field lines along the length of the device that drives this instability. In addition, early experiments with the Gasdynamic Trap at the Budker Institute Novosibirsk in Russia had suggested that the flute instability can be stabilized by a sufficient amount of plasma in and beyond the mirror region [21]. Other studies by Nagornyj *et al.* [22] have also shown that large mirror ratios in a high aspect ratio gasdynamic trap can have a stabilizing effect. Since the GDM satisfies these conditions and is designed to operate at high plasma density, with density just beyond the mirror being comparable to that in the central section, it is therefore possible to stabilize the plasma against flute instability in the GDM.

Furthermore, the high collisionality manifested by the small ion collision mean free path tends to repopulate the "loss cone" in ion velocity space. This prevents the loss cone microinstability, which is a result of velocity space asymmetry, from occurring. Experimental results have not indicated the presence of these microinstabilities [16]; however, even if they are present, the confinement time in a gasdynamic confinement system is not very sensitive to loss cone instabilities (unlike a classical mirror system, which is sensitive to these microinstabilities) [23]. In theory, microinstabilities appear only to be a problem in a high-temperature, low-density plasma.

Other experiments have also demonstrated that the gasdynamic confinement scheme is capable of supporting a high-β plasma [23]. Since β is a measure of how effective the magnetic field is in confining the plasma and is very sensitive to the aforementioned instabilities, high-β operation indicates that the system is operating with a high degree of plasma stability. In short, with careful design, we could circumvent major plasma stability problems that can prevent the proposed thruster from functioning effectively as described. Although sizable magnetic fields would be required for plasma confinement in high-power operation, propulsion device mass can be reduced with the use of high-temperature superconducting magnets. These magnets are currently being investigated and will hopefully be developed in the time frame of interest. Other techniques such as magnetic field reversal near the mirror region [24,25] may also yield mass reductions. Also, as mentioned in Section 1.1, the GDM is simply a plasma confinement and acceleration device. Thus, it can form the basis of an electric plasma thruster as well as a fission/fusion propulsion system. With the impressive progress being made in the development of high-power microwave sources (gigaWatts of power at giga-Hertz frequencies), the evolution of the GDM thruster into a MW-level system for use in cargo and human interplanetary missions appears to be very promising.

2.3 Fusion Concept Studies

2.3.1 Concept Description

The gasdynamic mirror was originally proposed by Kammash [18] as a means to utilize fusion reactions as a source of power for a space propulsion system. The system has a cross-sectional view illustrated in Figure 2.4. The halo thickness and magnet-shield

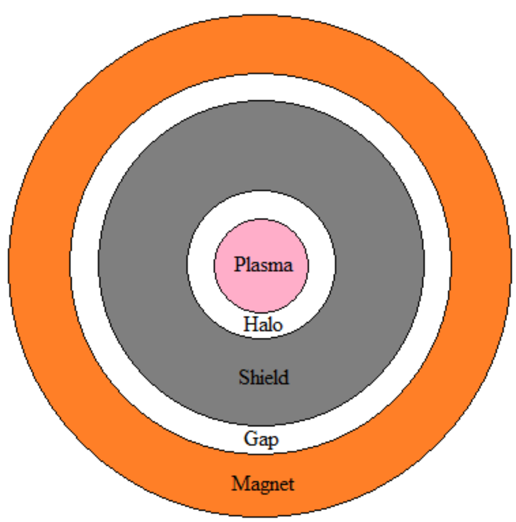

Figure 2.4. Cross-sectional view of the GDM fusion propulsion system.

gap were chosen to be 10 cm and the shield thickness was chosen to be 42 cm for our studies of the system [26].

The system is maintained at a steady-state by injecting fusion fuel in the region of a homogeneous magnetic field at a rate that replaces the amount lost from the mirrors. The fuel is confined long enough to allow fusion reactions to take place. Charged particles escaping through one end of the system contribute to the thrust. Charged particles escaping through the opposite end enter a direct converter that recovers the energy carried away by the particles at an efficiency η_D. Radiative losses (Bremsstrahlung and synchrotron radiation) are recovered by a thermal converter with an efficiency η_t. The recovered power is then recirculated back to the GDM fusion reactor to keep the plasma hot and sustain the reaction.

2.3.1.1 Lawson Criterion

To be practical, the fusion engine needs to exceed the "breakeven" condition, such that the energy from the fusion reaction is greater than that required to initiate fusion. The system is self-sustaining when it is at breakeven, which is a function of temperature, density and confinement time of the system. The minimum condition that must be met for a self-sustaining fusion reactor can be stated by the Lawson criterion [27]. In its simplest form, the Lawson criterion states that the energy release in fusion per unit volume is equal to the ion kinetic energy in that volume; i.e.,

$$n_1 n_2 \langle \sigma v \rangle E_{ch} \tau = \frac{3}{2}(n_1 + n_2)kT \qquad (2.15)$$

where n_1 and n_2 are the number densities of the two reacting ion species, E_{ch} is the energy released in the fusion reaction in the form of charged particles (since neutrons cannot directly help to keep the plasma hot), σ is the fusion cross section, and $n_1 n_2 \langle \sigma v \rangle$ is the reaction rate (number of reactions per volume per unit time) obtained by averaging over the Maxwellian velocity distribution of the interacting ions. The term $\langle \sigma v \rangle$ is obviously a function of temperature, and for deuterium-tritium (D-T) reaction becomes sizable at 10 keV, which is the typical temperature assumed. If we consider a 50-50 D-T mixture ($n_1 = n_2 = n/2$) at 10 keV, then the Lawson criterion yields

$$n\tau \approx 10^{14} \text{ sec/cm}^3 \tag{2.16}$$

which simply says that the product of the ion density and confinement time must exceed this order of magnitude for a self-sustaining D-T fusion reaction at 10 keV.

2.3.1.2 Power Balance

The energy balance of the system can be illustrated by a power flow diagram, Figure 2.5. As the diagram shows, the thermal converter recovers a portion of the neutron (P_n) and radiative (P_r) power loss, while the direct converter recovers some of the energy carried away by the fraction F of the charged particles escaping through the

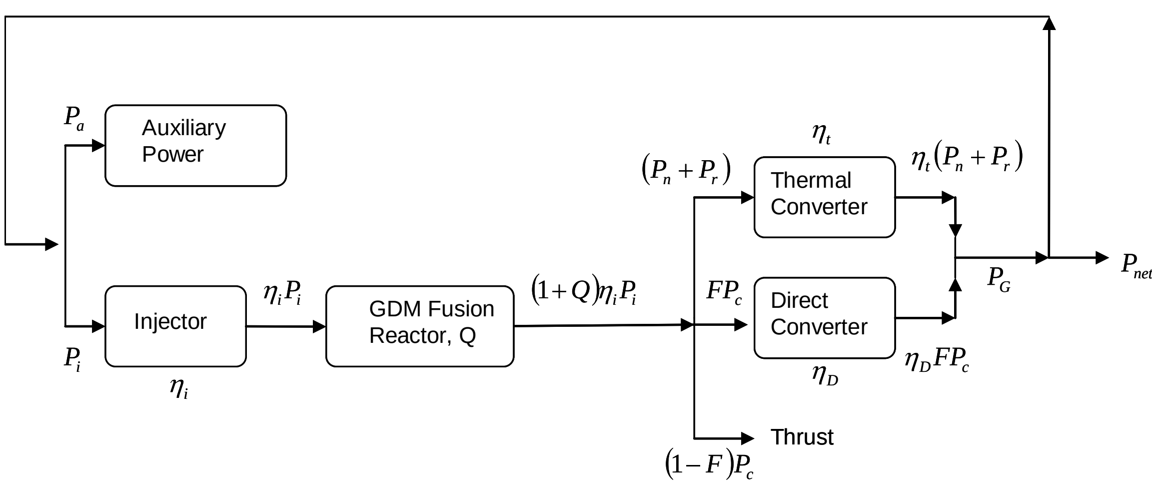

Figure 2.5. Power flow diagram for the GDM fusion propulsion system.

non-thrusting end of the device. In practice, the fraction F is controlled by having an asymmetric mirror ratio. This not only allows us to bias the flow of propellant toward the thrusting end of the device, but also allows us to vary the mass flow through each end to control thrust level as well as the amount of electric power the system produces. Together the direct and thermal converters produce the gross electric power P_G of the system. Reasonable values assume $\eta_D \approx 0.8$ and $\eta_t \approx 0.3$ [20]. The system depicted by Figure 2.5 also includes a certain amount of net electric power P_{net} extracted from the fusion reactor to power other systems on the spacecraft, as well as a portion of the recirculated power P_a that is used to power other reactor-related components, such as the pumps and the magnets. The rest of the recirculated power P_i is then injected back into the GDM reactor to sustain the fusion reaction. Injector efficiency is typically very high, and our studies assume $\eta_i \approx 1$. The fusion power is related to the injected power via the gain factor Q, namely $P_f = Q\eta_i P_i$. The minimum power the GDM fusion reactor needs to produce to sustain the fusion reaction is then given by when P_{net} and P_a are zero.

Using the power flow diagram, it is straightforward to derive an expression for the gain factor Q in terms of the system component powers and efficiencies.

$$Q = \frac{(1-\eta_i\eta_D F)P_f}{\eta_i\left[\eta_D F P_f + (\eta_t - \eta_D F)(P_n + P_r) - P_{net} - P_a\right]} \tag{2.17}$$

For a D-T fuel cycle, $(P_n + P_r) \approx 0.8P_f$. Assuming the aforementioned efficiency values and that P_a / P_f is negligible, then we can plot the gain factor as a function of the fraction of charged particles contributing to the thrust, $1-F$, for various P_{net}/P_f where $P_{net} = 0$

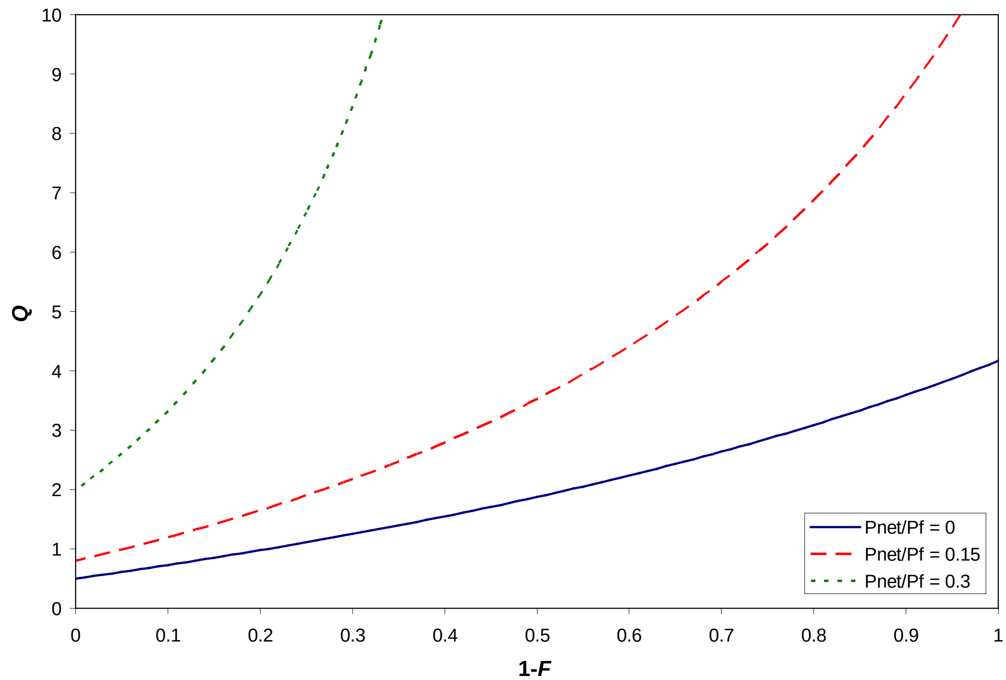

Figure 2.6. Gain factor Q as a function of the fraction of charged particles $(1-F)$ contributing to thrust for the deuterium-tritium fuel cycle. Assumptions: $\eta_D = 0.8$, $\eta_t = 0.3$, $\eta_i = 1.0$, $P_a / P_f << 1$.

means that the GDM fusion reactor is used strictly for propulsion. Clearly, the greater number of charged particles that are being used for thrust, the larger the fusion power the GDM reactor needs to generate to be self-sustained. This translates into higher density and higher temperature (that is, until the temperature for which peak $\langle \sigma v \rangle$ is reached), as Eq. (2.18) shows.

$$P_f = n_1 n_2 \langle \sigma v \rangle E_f \tag{2.18}$$

Furthermore, it should be noted that Eq. (2.17) has a singularity at $P_{net} + P_a = \eta_D F P_f + (\eta_t - \eta_D F)(P_n + P_r)$, which basically says that the power that can be extracted from the system is limited by the power recovered by the direct converter and thermal converter. In fact, the amount of extracted power cannot be anywhere close to that limit since realistically the remaining power would not be sufficient to keep the reactor self-sustained, as manifested by the huge Q value required near the limit.

2.3.1.3 Fusion Fuel Cycles

At this juncture, we will briefly look at various candidates for fusion fuel. The main interests are those involving deuterium, which is a stable, naturally occurring isotope of hydrogen.

$$\begin{aligned} {}_1\mathrm{D}^2 + {}_1\mathrm{D}^2 &\longrightarrow {}_1\mathrm{T}^3\left(1.01\,\mathrm{MeV}\right) + \mathrm{p}\left(3.02\,\mathrm{MeV}\right) \\ &\longrightarrow {}_2\mathrm{He}^3\left(0.82\,\mathrm{MeV}\right) + \mathrm{n}\left(2.45\,\mathrm{MeV}\right) \end{aligned} \tag{2.19}$$

$${}_1\mathrm{D}^2 + {}_1\mathrm{T}^3 \longrightarrow {}_2\mathrm{He}^4\left(3.5\,\mathrm{MeV}\right) + \mathrm{n}\left(14.1\,\mathrm{MeV}\right) \tag{2.20}$$

$${}_1\mathrm{D}^2 + {}_2\mathrm{He}^3 \longrightarrow {}_2\mathrm{He}^4\left(3.6\,\mathrm{MeV}\right) + \mathrm{p}\left(14.7\,\mathrm{MeV}\right) \tag{2.21}$$

The easiest reaction according to the Lawson criterion is the deuterium-tritium reaction, Eq. (2.20), meaning the confinement requirement is the least demanding. It also has the highest fusion cross section (except between around 450-1000 keV where D-He^3 is slightly higher [28], although D-T still has the highest $\langle \sigma v \rangle$ overall as shown in Figure 2.7). At temperatures below 100 keV, the D-T cross section is at least two orders of magnitude higher than the total for both branches of D-D, and as a result D-D reaction is negligible in the D-T cycle. On the other hand, D-T reaction cannot be ignored in the D-D cycle since its proton branch produces tritium. Thus, while the D-D cycle itself has the advantage of producing much lower energy neutrons, that advantage becomes somewhat inconsequential in practice. Figure 2.7 shows a plot of the reaction rates $\langle \sigma v \rangle$ for the above fuel cycles using data in Ref. [28].

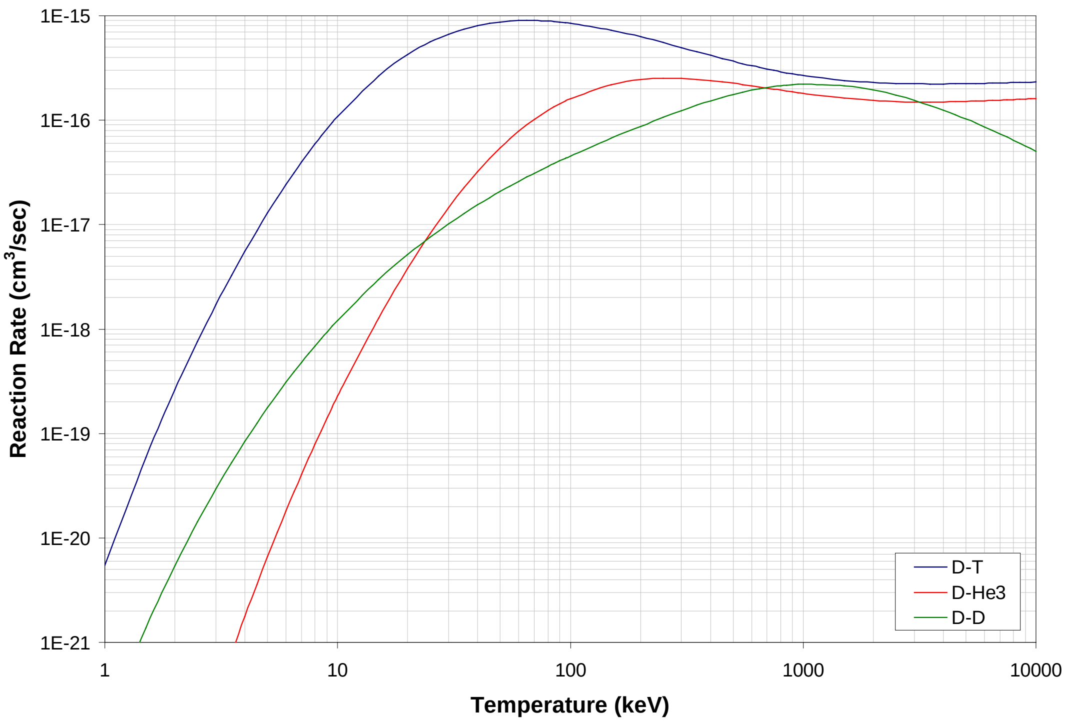

Figure 2.7. Fusion reaction rates $\langle \sigma v \rangle$ averaged over Maxwellian distributions. Note that the individual reactivity for both branches of the D-D cycle are added to produce the D-D curve in the figure [29].

Since tritium is radioactive, it occurs naturally only in negligible amounts. Tritium breeding is done by the interaction of neutrons with lithium via the following two reactions. Note that the second reaction is endothermic; i.e. energy needs to be supplied for the reaction to take place.

$$\begin{aligned} {}_3\mathrm{Li}^6 + \text{"slow" n} &\longrightarrow {}_1\mathrm{T}^3 + {}_2\mathrm{T}^4 + 4.8\,\mathrm{MeV} \\ {}_3\mathrm{Li}^7 + \text{"fast" n} &\longrightarrow {}_1\mathrm{T}^3 + {}_2\mathrm{T}^4 - 2.5\,\mathrm{MeV} + \mathrm{n}'(\mathrm{slow}) \end{aligned} \tag{2.22}$$

Since the fast neutrons in the D-T cycle are the main cause of radiation damage and induced radioactivity in the reactor, the "clean" D-He^3 fuel cycle becomes attractive because it does not produce neutrons. Unfortunately, it alleviates but does not completely eliminate the problem; as long as deuterium is present, the D-D reaction will take place, although to a lesser degree, and the D-T reaction will automatically follow. The more important advantage of D-He^3, however, is that the primary fusion products are all charged particles, and energy can be extracted readily in a direct conversion scheme. Also, from a propulsion standpoint, most of that fusion energy is “usable” and can be converted to directed thrust since it is carried by charged particles, whose motions are influenced by magnetic and electric fields.

Finally, Eqs. (2.23) to (2.25) give the power densities for the three fuel cycles released in the form of charged particles [29]. Note that the expression for D-D, Eq. (2.23), already takes into account the subsequent D-T reaction. From the equations and Figure 2.7, we can see that D-T has a higher power density than D-D for all temperatures and in fact yields the highest power density of all three fuel cycles at temperatures below 100 keV. This together with the least demanding Lawson criterion and the relative ease of ignition (10 keV vs. 75-100 keV for D-He^3) makes D-T the primary candidate for the first generation of GDM fusion propulsion system.

$$P_{DD} = 3.3\times 10^{-13} n_D^2 \langle \sigma v \rangle_{DD} \ \mathrm{watt/cm^3} \tag{2.23}$$

$$P_{DT} = 5.6\times 10^{-13} n_D n_T \langle \sigma v \rangle_{DT} \ \mathrm{watt/cm^3} \tag{2.24}$$

$$P_{DHe^3} = 2.9\times 10^{-12} n_D n_{He^3} \langle \sigma v \rangle_{DHe^3} \ \mathrm{watt/cm^3} \tag{2.25}$$

2.3.2 Magnetic Field Asymmetry and System Performance

In order to study the GDM propulsion concept, a physics-based model was developed to model the plasma dynamics inside the gasdynamic mirror, and a computer code was written based on the model to solve for the set of consistent plasma parameters given a particular set of inputs. Both the model and the code will be explained in details in Chapter 3. The goal in this section is to present results when applying the model to a GDM fusion propulsion system.

One of the observations from the analytical model is that magnetic field asymmetry and the mirror ratios have a direct and significant effect on the performance of the GDM. This is because the thrust and specific impulse of the system directly depend on the particle escape energy, confinement time, and the ambipolar potential, all of which are interdependent and are ultimately dependant on the mirror ratios of the system. The goal here is to quantify this dependence. Consider a 50-50% D-T system operating at steady state at a density of 5×10^{17} cm^{-3} and a temperature of 10 keV. The exact density chosen here, as will be shown later, is inconsequential since it is the trend that is of interested. Typical expected efficiencies for the injector, direct converter and thermal converter efficiencies are used, namely $\eta_i \approx 1$, $\eta_D \approx 0.8$, and $\eta_t \approx 0.3$. The plasma beta value β is assumed to be 0.95.

2.3.2.1 Mirror Ratios Effects at Fixed Temperature and Density

Figure 2.8 shows how the ambipolar potential varies with the mirror ratio R_T at the thrusting end for various mirror ratio R_D at the direct converter end. For a given R_D, the potential increases approximately logarithmically with R_T, and at a given R_T, it increases with increasing R_D. Each curve in the plot ends when $R_T = R_D$, where half of the charged particle power appears as thrust power and the other half goes to the direct converter. Since the GDM is strictly operating as a propulsion system; i.e. $P_{net} = 0$, there is no merit for $R_T > R_D$ because the thrust power would be less than 50% in that case,

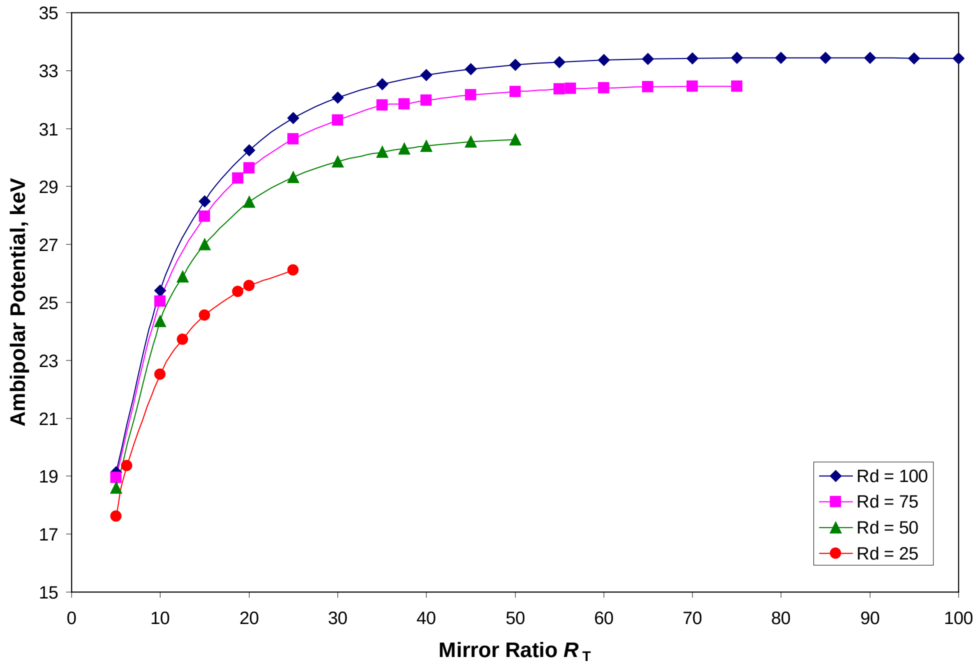

Figure 2.8. Ambipolar potential as a function of the two mirror ratios R_T and R_D at 10 keV temperature and a density of 5×10^{17} cm^{-3}.

and most of the power would then go through the direct converter leading to greater loss. Finally, Figure 2.8 shows that the ambipolar potential is quite significant; in fact for the settings used, the potential is about the same or greater than the ion escape energy, as seen in Figure 2.9. This significantly enhances the energy (and, thus, the velocity) of the ions, which provide the bulk of the thrust as they leave the GDM chamber.

Figure 2.9 shows the behavior of the average electron escape energy E_{Le} and the average ion escape energy E_{LiT} at the thrusting end. The electron energy has the same general dependence on R_T as the ambipolar potential. This is due to the fact that because of their small mass and high energy, the electrons do not *see* the mirror and are not directly affected by it, but are only influenced via the ambipolar potential. On the other hand, the ions are directly affected by the mirror, as well as the potential, which is

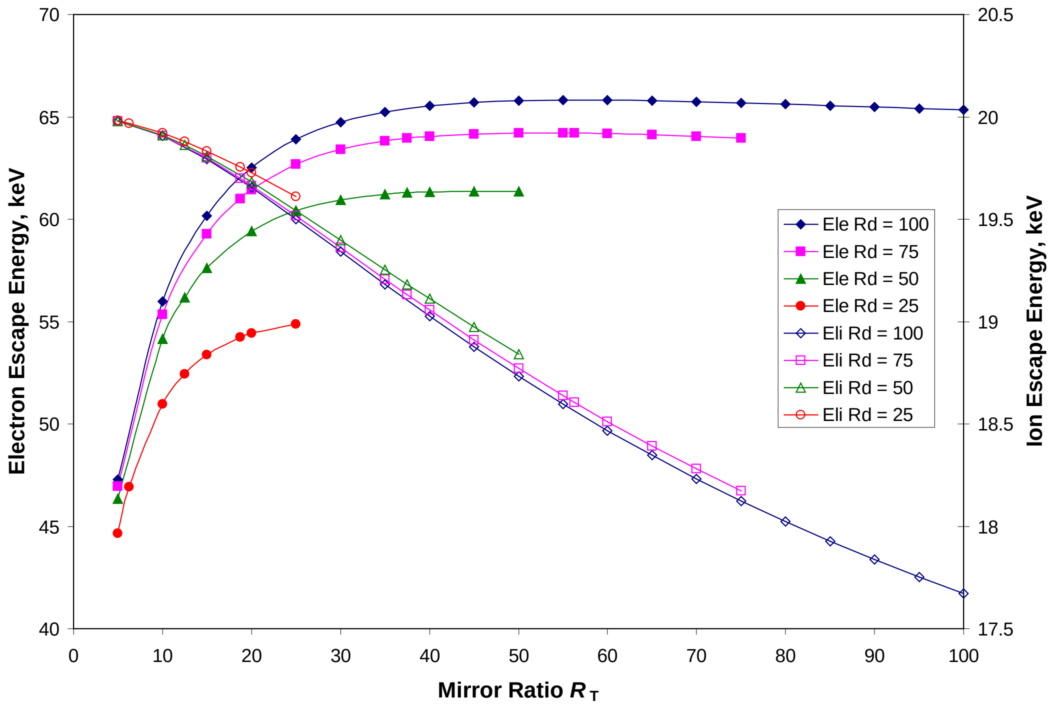

Figure 2.9. Average electron (E_{Le}) and ion (E_{LiT}) escape energies as a function of the mirror ratios, under the same simulation conditions as Figure 2.8.

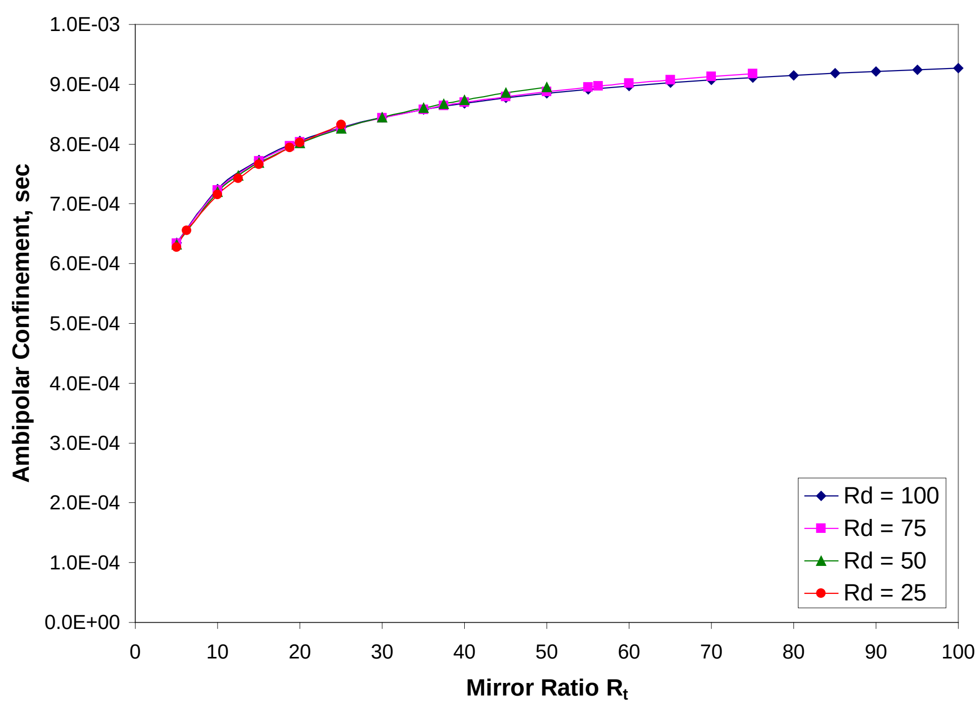

Figure 2.10. Ambipolar confinement time at the thrusting end as a function of the mirror ratios, under the same conditions as Figure 2.8.

evidenced in Figure 2.9.

Figure 2.10 shows the dependence of the ambipolar confinement time τ_T at the thrusting end. The derivation of the confinement time will be addressed in Chapter 3. The results show that it increases in an approximately logarithmic fashion with R_T for a given R_D, although the overall increase is not very drastic. Furthermore, the dependence on R_D is very weak, as can be expected since the figure shows the confinement time for the exit mirror.

Figure 2.11 depicts how the thrust of the GDM varies with R_T and R_D. The thrust decreases approximately exponentially with R_T for a given R_D; this behavior is due to its dependence on the ambipolar confinement time that enters into the mass flow rate calculation as Chapter 3 will show. The dependence of thrust on R_D, however, is not significant, even though closer inspection suggests that for a given R_T, the thrust decreases slightly with decreasing R_D.

Figure 2.12 depicts how the I_{sp} of the GDM varies with R_T and R_D. The average escape velocities of the ions and electrons are proportional to $\sqrt{E_{LiT} + e\phi}$ and $\sqrt{E_{Le} - e\phi}$, respectively. Figure 2.8 and Figure 2.9 show that both of these quantities increase with increasing R_D, which is consistent with the I_{sp} results. In addition, for a given R_D, the particle velocity increases, reaches a maximum, and then gently decreases with increasing R_T.

Finally, Figure 2.13 relates the values of the two mirror ratios R_T and R_D to the fraction *F* of charged particle power that goes to the direct converter. For a given R_T, the

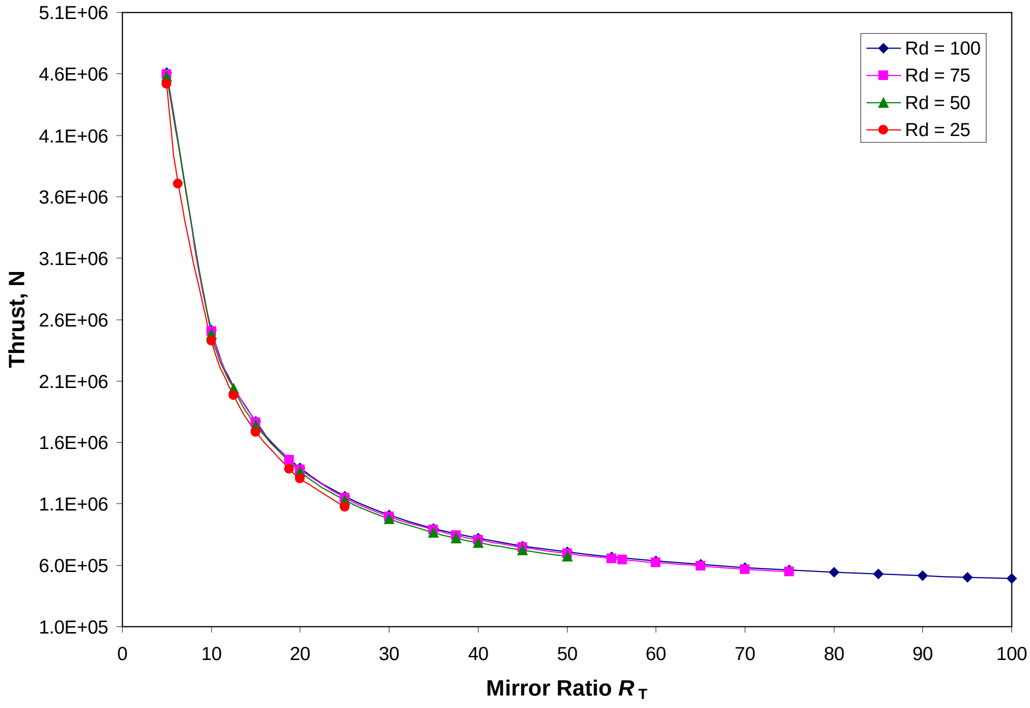

Figure 2.11. Thrust as a function of the mirror ratios at 10 keV temperature and a density of 5×10^{17} cm^{-3}.

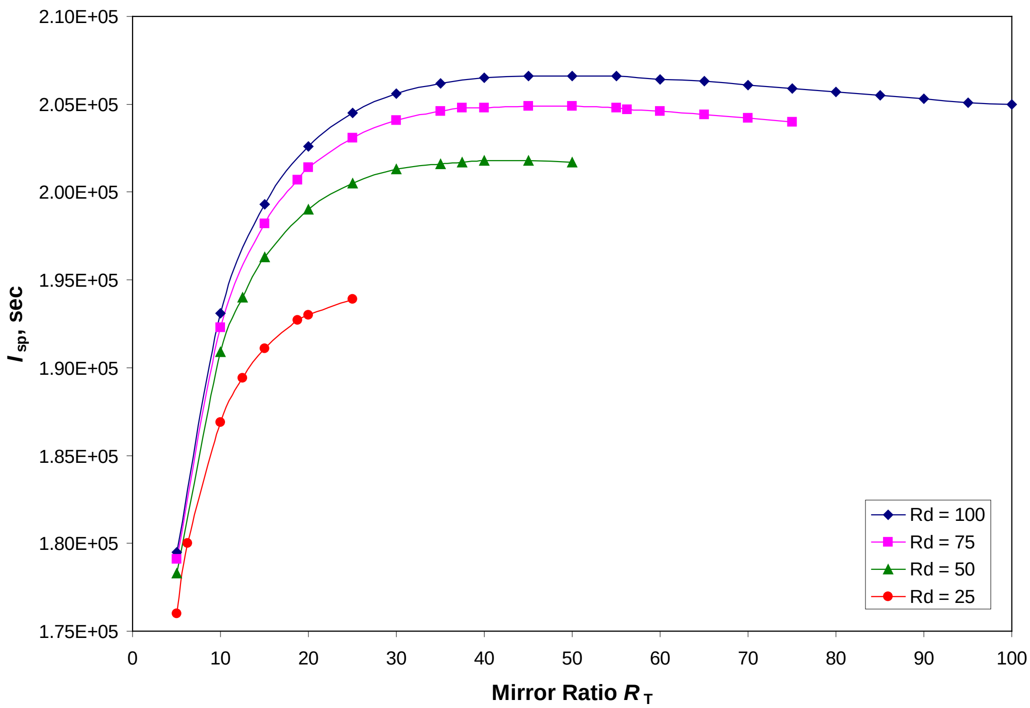

Figure 2.12. Specific impulse as a function of the mirror ratios at 10 keV temperature and a density of 5×10^{17} cm^{-3}.

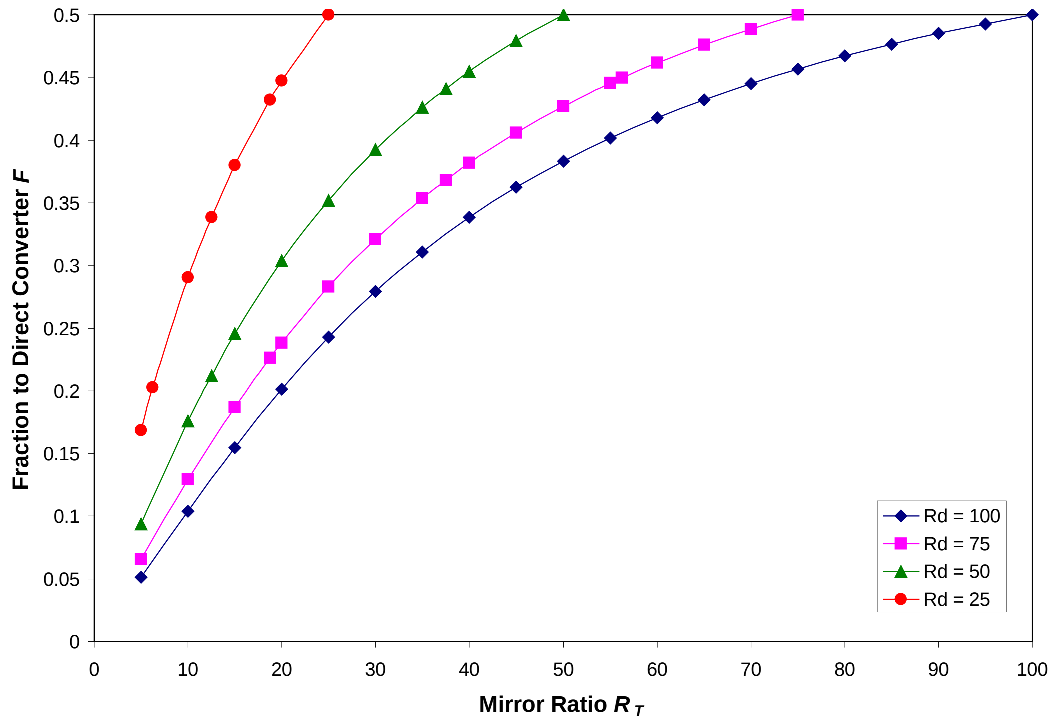

Figure 2.13. Fraction of charged particle power going to the direct converter, under the same conditions as Figure 2.8.

fraction F increases with decreasing R_D as expected . Similarly, the higher R_D is, the higher R_T needs to be to keep the fraction F the same.

2.3.2.2 Effects of R_T and R_D for Fixed R_T/R_D Ratio

Finally, Table 2.1 shows how the performance of the GDM varies for a given R_T/R_D ratio. As before, the simulations assume a 10 keV temperature and a density of $n = 5\times10^{17}\,\mathrm{cm}^{-3}$, with the GDM running in steady-state 50-50% D-T fusion mode. Table 2.1 shows that for a given ratio, the thrust increases as the mirror ratios are reduced. This is due to the increased mass flow through the mirrors because more ions are able to escape. On the other hand, the decreasing potential due to the decreasing mirror ratios

R_T/R_D	R_D	R_T	F	T (N)	I_{sp} (sec)
0.25	100	25	0.24	1.16×10^6	2.05×10^5
	75	18.75	0.23	1.46×10^6	2.01×10^5
	50	12.5	0.21	2.04×10^6	1.94×10^5
	25	6.25	0.20	3.70×10^6	1.80×10^5
0.5	100	50	0.38	7.08×10^5	2.07×10^5
	75	37.5	0.37	8.45×10^5	2.05×10^5
	50	25	0.35	1.13×10^6	2.01×10^5
	25	12.5	0.34	1.99×10^6	1.89×10^5
0.75	100	75	0.46	5.62×10^5	2.06×10^5
	75	56.25	0.45	6.45×10^5	2.05×10^5
	50	37.5	0.44	8.22×10^5	2.02×10^5
	25	18.75	0.43	1.38×10^6	1.93×10^5
1	100	100	0.5	4.91×10^5	2.05×10^5
	75	75	0.5	5.48×10^5	2.04×10^5
	50	50	0.5	6.71×10^5	2.02×10^5
	25	25	0.5	1.08×10^6	1.94×10^5

Table 2.1. Results on varying the R_T/R_D ratio.

leads to a reduction in the specific impulse. Another observation made explicit by Table 1 is that the fraction $(1-F)$ of charged particle power that is converted to thrust power increases slightly as the mirror ratios decrease, even though the R_T/R_D ratio remains constant, as long as R_T/R_D is less than unity.

In conclusion, this section presented the results of a numerical study of how magnetic field asymmetry affects the propulsive capabilities of the GDM through its effects on ambipolar potential, confinement time and particle escape energies. The dependency is a direct consequence of the physics-based model that was developed. The magnitudes of the various quantities such as thrust and specific impulse obtained above are inconsequential in the current study; what is of interest is the overall trend on how these quantities are affected by the changing mirror ratios. The results suggest the possibility that the thrust and specific impulse can be controlled by varying the mirror ratios since the various quantities depend on the mirror ratios and not necessarily on the individual field strength at various sections of the GDM.

2.3.3 Plasma Parameters and System Design

In addition to propulsive capabilities, the mass of the system is another important metric for a propulsion system, since it partially controls the thrust to weight ratio. Naturally, one would like to maximize this ratio. The system mass is of course quite dependent on the length of the system, which is dictated by the plasma length required for self-sustained fusion. The length of the plasma varies depending on the plasma parameters and system attributes such as the chosen mirror ratios.

Figure 2.14 shows how the plasma length varies with these quantities. Surprisingly, for these cases, R_D has a negligible effect on plasma length. Of course R_D still has an effect on other system attributes such as thrust and power balance, since varying R_D varies the fraction of charged particles going to the direct converter.

For a given density and pair of mirror ratios, there is an optimal temperature at which the plasma length is minimized. This is a direct consequence of the dependence of the fusion reaction rates on temperature. Furthermore, at a given temperature, the higher the density and the higher R_T is, the lower the plasma length, which improves system mass. However, that is not the whole story, since increasing the mirror ratio increases the magnet mass, which might negate any benefits resulting from a smaller plasma length. The full optimization problem is beyond the scope of this work.

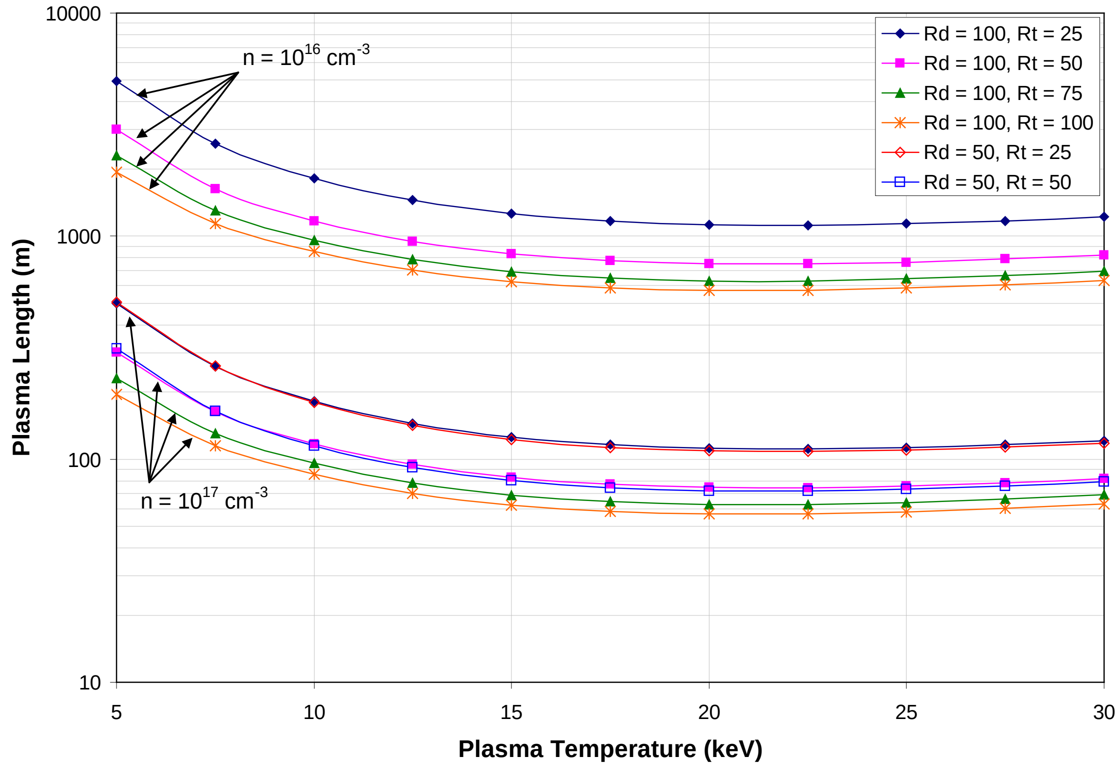

Figure 2.14. Dependence of plasma length on temperature, density and GDM mirror ratios.

2.4 Hybrid GDM Concept

In the previous section, a fusion GDM propulsion concept using 50-50% D-T fuel was described. Deuterium-tritium is chosen because it has the least demanding confinement requirements, and because it produces the highest power density at a comparatively low temperature of 10 keV among the various fusion fuels. To ignite the fuel and achieve self-sustained fusion, of course, the fuel needs to be heated to 10 keV, and in this section a scheme is proposed that could achieve that.

2.4.1 Concept Description

The proposed system, a fission-fusion hybrid system, is illustrated in Figure 2.15.

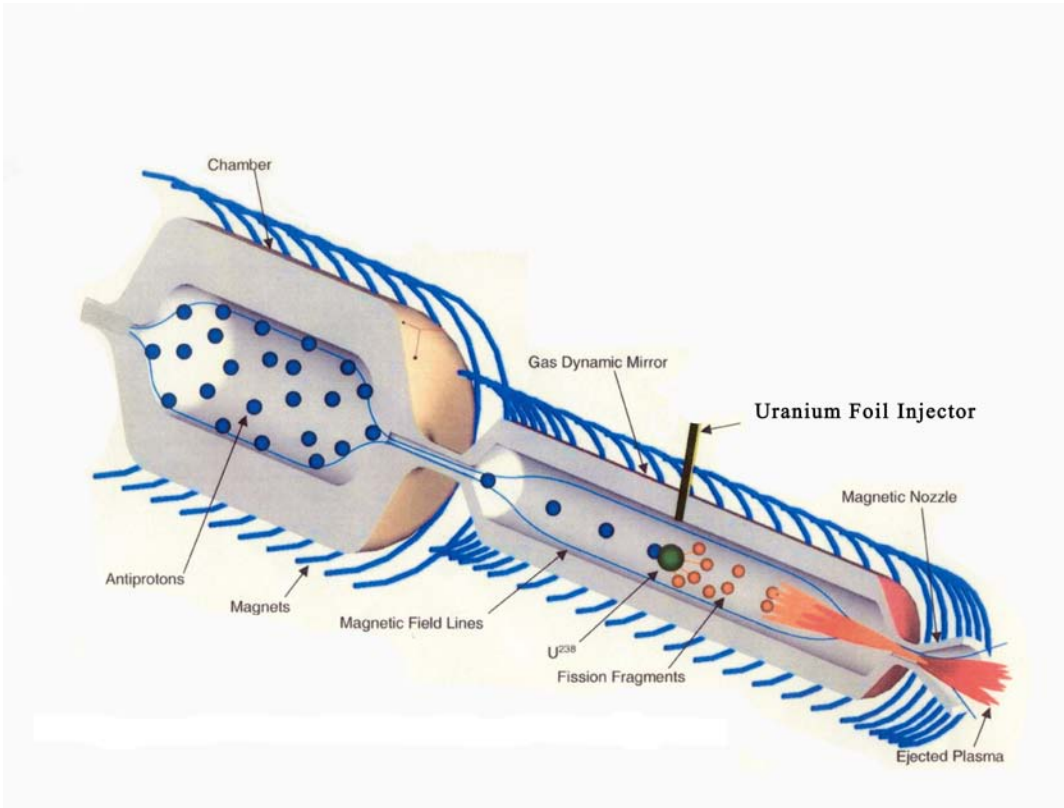

Figure 2.15. Antiproton-driven fusion GDM propulsion concept.

It consists of an antiproton trap attached to the GDM. The heating process is based on theoretical and experimental physics research which revealed that "at-rest" annihilation of antiprotons in uranium-238 targets causes fission at nearly 100% efficiency [30,31]. Thus, heating in the proposed system can be achieved by inserting U^{238} targets (in the form of foils or atomic beams) in the proper position and then striking them with antiprotons from an axially injected pulsed antiproton beam released from the trap. The antiprotons will slow down on the plasma electrons until they encounter the U^{238} targets and eventually annihilate with a neutron or proton inside the nuclei. This causes the U^{238} nuclei to undergo fission. The resulting fission fragments and annihilation products (pions and muons) are highly ionizing and energetic, and can readily heat the background D-T plasma to very high temperatures leading to its ignition.

2.4.2 At-Rest Antiproton Annihilation

Several studies [30,31] in the last couple decades have shown that "at-rest" annihilation of antiprotons in the uranium isotope U^{238} leads to fission at nearly 100% efficiency. Figure 2.16 shows the fission probabilities for various heavy nuclei. The resulting highly charged, fast fission fragments are highly ionizing, and can heat a suitable medium to very high temperatures.

When an antiproton or a proton with multiple MeV kinetic energy slams into a target material, it undergoes collisions with the electrons of the target and slows down by giving up energy to these particles. A proton striking a solid target will either come to rest in the material and form a chemical bond with other atoms, or it diffuses around as atomic hydrogen. An antiproton striking the target will displace an orbital electron around the nucleus and then begin immediately to cascade down in energy towards the ground state emitting x-rays as it makes these transitions. Eventually, it enters the nucleus, and an annihilation with either a neutron or a proton takes place. At this point the kinetic energy of the antiproton is measured in eV, not in MeV; hence the label "at-rest" annihilation.

Nuclear fission following the annihilation at-rest of antiprotons in heavy nuclei has been demonstrated in uranium and bismuth [32]. Measurements have been made of the mass distribution of the fission fragments, as well as the multiplicity of the light charged particles that were emitted in the process [32]. It was shown that,when antiprotons are annihilated in uranium, the average mass and kinetic energy of each of the two fission fragments is approximately 106 amu and 80 MeV. Figure 2.17 shows the detailed mass and kinetic energy distributions. It was also shown that, on the average, the

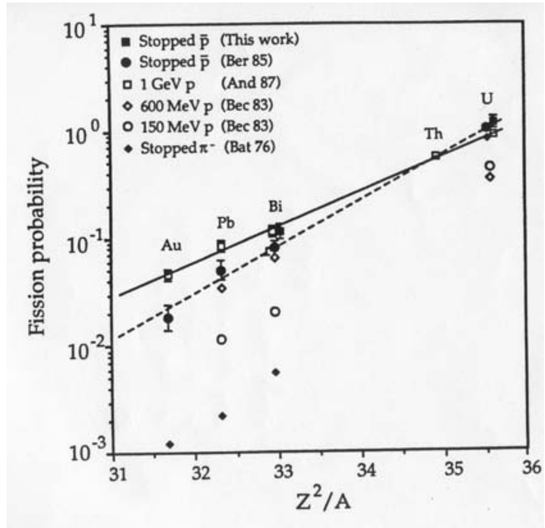

Figure 2.16. Fission probabilities for various heavy nuclei [32].

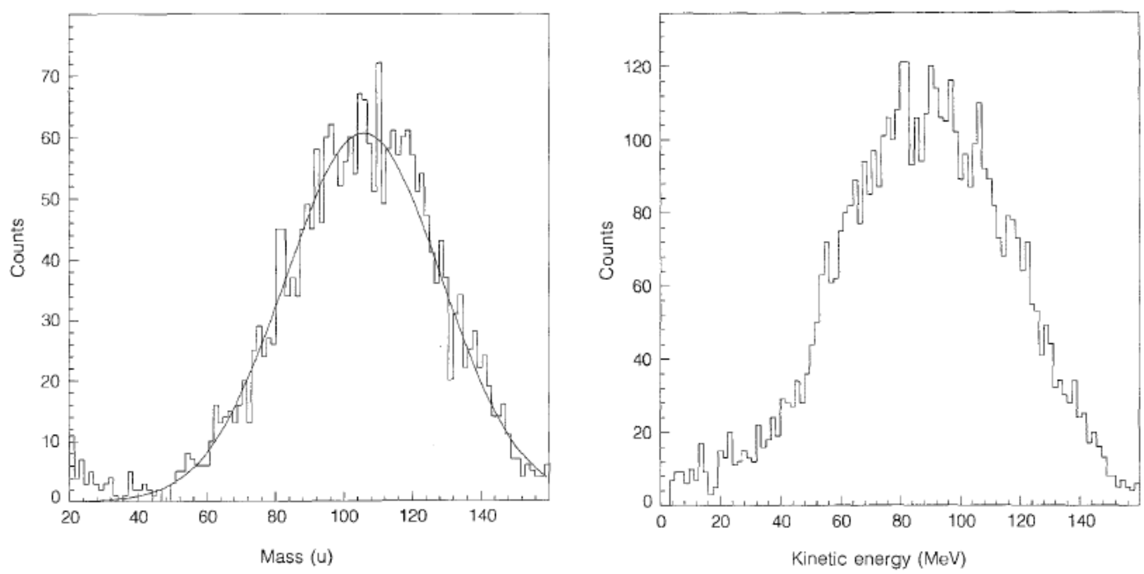

Figure 2.17. Fission fragment mass and kinetic energy distribution for a uranium target [32]. Note that the energy spectrum was not corrected for slight energy losses in the target.

fission fragments left the target nearly isotropically, making this reaction especially desirable for heating a propellant.

In a low temperature plasma of, for instance, 13.6 eV (corresponding to the ionization energy of hydrogen), an energetic antiproton can slow down on the electrons of the plasma or undergo annihilation reactions with the ions of the medium. The rate of annihilation (i.e., number of annihilation per unit length) is given by the following equation [33].

$$\frac{dp}{dx} = 0.19 n \pi r_0^2 \left(\frac{\gamma}{1 - e^{-\gamma}} \right) \frac{c}{v} \tag{2.26}$$

where n is the plasma density, c the speed of light, v the velocity of the antiproton, r_0 the classical electron radius (2.82x10^{-13} cm) and the dimensionless constant

$$\gamma = 2\pi\alpha \frac{c}{v} \tag{2.27}$$

with α being the fine structure constant (1/137).

The energy loss per unit time for the interaction with the electrons can be expressed by the following [20].

$$\frac{dE}{dt} = v\frac{dE}{dx} = -c_1 E \tag{2.28}$$

where E is the energy of the antiproton and c_1 is a constant given by

$$c_1 = 2 \times 10^{-12} \frac{n}{m_{\bar{p}} T_e^{3/2} (\mathrm{keV})} \tag{2.29}$$

Here $m_{\bar{p}}$ represents the mass of the antiproton in atomic mass units (amu) and T_e the electron temperature in the plasma. The distance x in the plasma which the antiproton must traverse from the injection point in order to reach a particular value of energy, E, is obtained by integrating Eq. (2.28) over x with the result

$$E(x)^{1/2} = E_0^{1/2} - c_1 \sqrt{\frac{m_{\bar{p}}}{8}} x \tag{2.30}$$

where E_0 is the initial energy, namely that at $x = 0$.

The desired position for the annihilation is one that corresponds to a final energy that is near zero, so as to invoke the "at-rest" condition alluded to earlier. The quantity of interest is *f*, which represents the fraction of antiprotons that have annihilated after penetrating a given distance into the GDM. It can be expressed in terms of *p* as follows:

$$f = 1 - e^{-p[E(x)]} \tag{2.31}$$

where $p(E)$ represents the annihilation as a function of energy. This annihilation rate can be obtained from combining the annihilation per unit length dp/dx, Eq. (2.26), and energy loss per unit path dE/dx, Eq. (2.28); i.e.,

$$\frac{dp}{dE} = \frac{dp}{dx}\left(\frac{dE}{dx}\right)^{-1} \tag{2.32}$$

The above equation is integrated to yield

$$p(E) = \frac{2\beta}{k}\ln\left[\frac{e^{kE^{-1/2}} - 1}{e^{kE_0^{-1/2}} - 1}\right] \tag{2.33}$$

where

$$\begin{aligned} \beta &= \frac{0.19\pi^2 r_0^2 n\alpha c^2}{c_1}\sqrt{2m_{\bar{p}}} \\ k &= 2\pi\alpha c\sqrt{\frac{1}{2}m_{\bar{p}}} \end{aligned} \tag{2.34}$$

Note that when $E = E_0$, $p = 0$ and $f = 0$ as expected. Also, the dependence of *f* on *x* is through $p[E(x)]$, as can be seen from Eqs. (2.30) and (2.33).

For a D-T plasma density of $n = 5\times10^{16}\ \text{cm}^{-3}$ in the GDM with an initial temperature of $T_e = 13.6\,\text{eV}$, and assuming that the antiprotons are injected at an energy of 20 keV, the antiprotons will have a final energy of $E \approx 0$ at $x = 17\,\text{cm}$. Figure 2.18 shows that most of the antiprotons do not get annihilated until their energies are sufficiently close to zero. This is the distance from the point of injection at which the U^{238} targets must be radially inserted in order to affect an “at rest” annihilation in the target.

Figure 2.19 shows that this “at rest” distance decreases exponentially with the plasma (electron) density. The assumption of 20 keV antiproton energy is based on existing portable Penning trap technology, such as the HiPAT built by J. Martin at NASA Marshall Space Flight Center that can hold 10^{12} antiprotons at 20 keV [34]. Upon initiating the fission in the U^{238} ions, two fission fragments are produced per annihilation that will then heat the electrons of the D-T plasma.

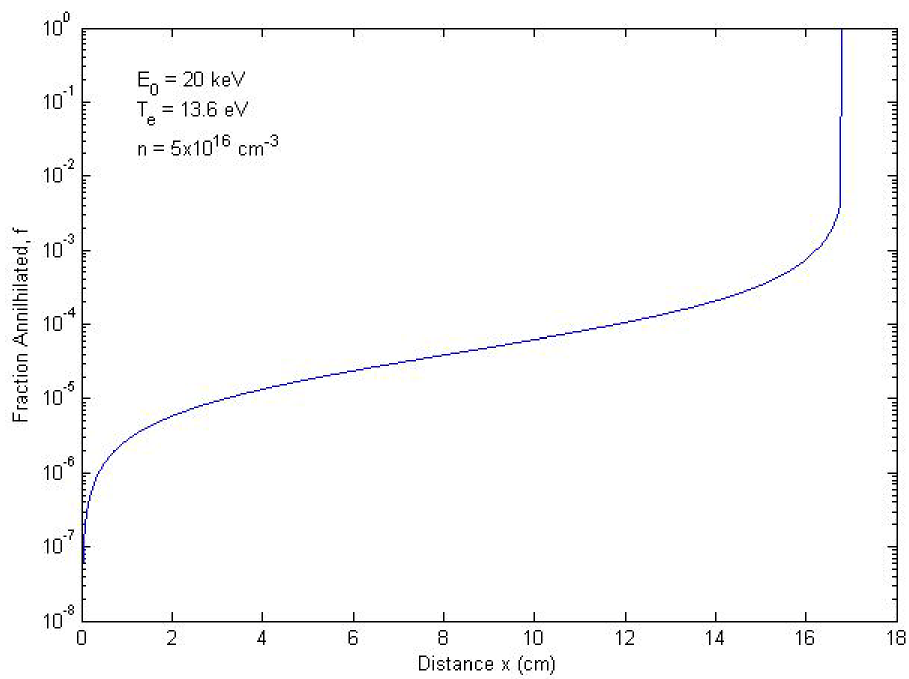

Figure 2.18. Fraction of antiprotons annihilated vs. distance traveled at specified conditions.

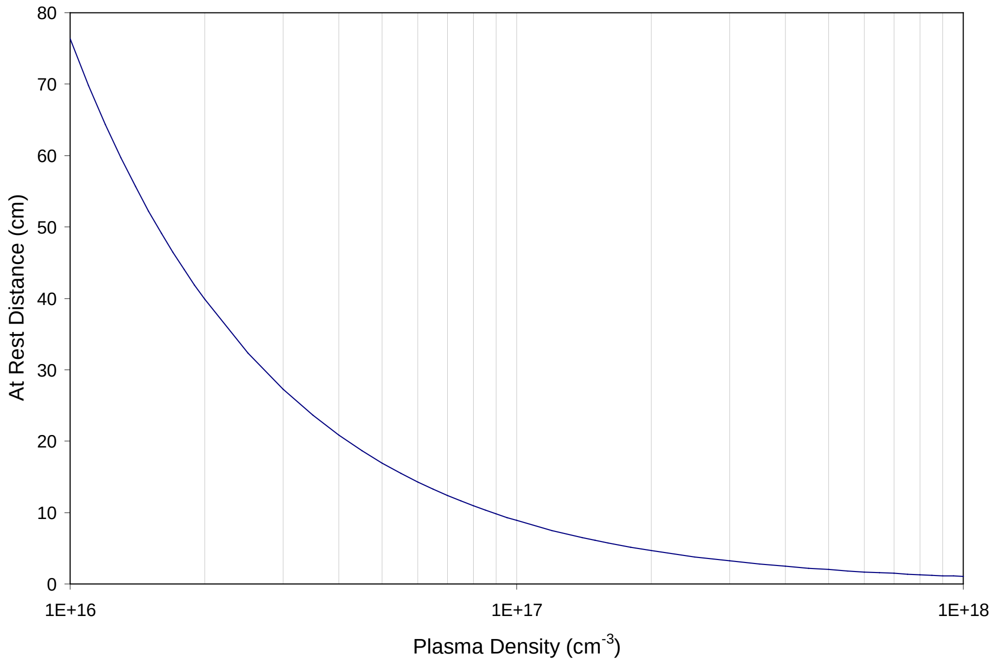

Figure 2.19. Distance at which the antiprotons are "stopped" as a function of plasma (electron) density.

2.4.3 Heating of Plasma Electrons

As described above, the process begins with antiproton annihilation. Statistically speaking, an average (over a large number of reactions) of three charged pions and two neutral pions are created per proton-antiproton annihilation. However, to be conservative in the analysis below, two charged pions (one positive and one negative) are assumed to be created from every annihilation reaction.

$$
\begin{aligned}
& p + \overline{p} \longrightarrow a\pi^0 + b\pi^+ + b\pi^-, a \approx 2, b \approx 1.5 \\
& \pi^+ \xrightarrow{72ns} \mu^+ + \nu_\mu \\
& \pi^- \xrightarrow{72ns} \mu^- + \overline{\nu}_\mu \\
& \mu^+ \xrightarrow{6.2\mu s} e^+ + \nu_\mu + \overline{\nu}_e \\
& \mu^- \xrightarrow{6.2\mu s} e^- + \overline{\nu}_\mu + \nu_e
\end{aligned}
\tag{2.35}
$$

The neutral pions, since they are uncharged and decay into gamma photons almost instantly (8.4×10^{-18} sec), do not directly participate in the heating process. However, the charged pions (each with kinetic energy of 250 MeV at birth) and their decay products (the charged muons with kinetic energy of 192.3 MeV) have the potential to transfer some of their energy to the plasma electrons during their lifetime.

2.4.3.1 Energy Transfer by Coulomb Collisions

The primary method of kinetic energy transfer from the charged annihilation products and fission fragments to the plasma is by Coulomb collisions with the plasma electrons. The rate of this energy coupling is given by

$$\frac{dE}{dt} = -\left[\frac{8}{3}\sqrt{2\pi}Z^2 Z_e^2 e^4 \sqrt{m_e}\ln\Lambda \frac{n_e}{m} C\right]\frac{E}{T_e^{3/2}} = -A\frac{E}{T_e^{3/2}} \tag{2.36}$$

$$C = \left(1.6022\times10^{-9}\right)^{-3/2}\left(\frac{\text{keV}}{\text{erg}}\right)^{3/2} \tag{2.37}$$

where A has been defined as

$$A \equiv \frac{8}{3}\sqrt{2\pi}Z^2 Z_e^2 e^4 \sqrt{m_e}\ln\Lambda \frac{n_e}{m} C \tag{2.38}$$

Equation (2.36) is written in the CGS system, so m_e and m are respectively the electron and incident particle mass in *grams*, e is the elementary charge in *stat-Coulombs*, Z and Z_e are respectively the charge states of the incident (e.g. annihilation products, fission fragments) and target (i.e. electrons in the current analysis) particles, n_e is the electron density in cm^{-3}, T_e is the electron temperature in *keV* (and C is a conversion factor that allows us to use *keV* as a convenient unit for temperature). The Coulomb Logarithm $\ln\Lambda$ is given by the following for a deuterium-tritium (D-T) plasma,

$$\ln \Lambda = 24 - \log \frac{\sqrt{n_e}}{T_e \times 1000} \tag{2.39}$$

where n_e is again the electron density in cm^{-3}, and T_e is the electron temperature in *keV*.

For an initial plasma electron temperature of T_{e0}, the kinetic energy lost by the incident particle $E_0 - E$ becomes the plasma electron thermal energy. The energy balance equation is therefore as follows,

$$\frac{3}{2} n_e \left(T_e - T_{e0} \right) = n_{inc} \left(E_0 - E \right) \tag{2.40}$$

where n_{inc} is the density of incident particles and E_0 is the initial incident particle energy. For the current analysis, where the incident particles include both the annihilation products (charged pions and muons) and the fission fragments resulting from antiproton-induced fission, Eq. (2.40) can be rewritten as follows,

$$\frac{3}{2} \left(T_e - T_{e0} \right) = \frac{n_{inc}}{n_e} \left(E_0 - E \right) = \frac{2 n_{\bar{p}}}{n_e} \left(E_0 - E \right) = 2R \left(E_0 - E \right) \tag{2.41}$$

Equation (2.41) uses the assumption that the charged pion/muon/fission fragment density is twice the antiproton density. This assumption stipulates that for every antiproton annihilated, two charged pions are created, which subsequently decay into two muons. Also, the induced fission creates two fission fragments. Moreover, a quantity R (not to be confused with the mirror ratio) was defined as the ratio of antiproton density to electron density.

Differentiating Eq. (2.41) with respect to time, substituting Eq. (2.36) for dE/dt in the resulting expression, and then substituting for E by rearranging Eq. (2.41), the following result is obtained,

$$
\begin{aligned}
\frac{dT_e}{dt} &= -\frac{4}{3}R\frac{dE}{dt} = -\frac{4}{3}R\left(-A\frac{E}{T_e^{3/2}}\right) \\
&= \frac{4R}{3}\frac{A}{T_e^{3/2}}\left(E_0 - \frac{3T_e}{4R} + \frac{3T_{e0}}{4R}\right) \\
&= A\frac{\frac{4}{3}RE_0' - T_e}{T_e^{3/2}} \\
&= A\frac{\frac{2}{3}R'E_0' - T_e}{T_e^{3/2}}
\end{aligned}
\tag{2.42}
$$

where the following definitions were used:

$$
\begin{aligned}
R' &\equiv 2R \\
E_0' &\equiv E_0 + \frac{3T_{e0}}{4R} \equiv E_0 + \frac{3T_{e0}}{2R'}
\end{aligned}
\tag{2.43}
$$

The ratio R' can be interpreted as the number of incident particles per electron of the D-T plasma (i.e. ratio of the annihilation products density or fission fragments density to electron density) and is defined here only for convenience. Rearranging Eq. (2.42) and integrating gives

$$
\int_{T_{e0}}^{T_e} \frac{T_e^{3/2}}{\frac{2}{3}R'E_0' - T_e} dT_e = A\int_0^{\tau} dt \tag{2.44}
$$

The solution of this integral (with τ being the heating time) is

$$
\left. -\frac{2}{3}T_e^{3/2} - 2\left(\frac{2}{3}R'E_0'\right)T_e^{1/2} + \left(\frac{2}{3}R'E_0'\right)^{3/2} \ln\left(\frac{\sqrt{\frac{2}{3}R'E_0'} + T_e^{1/2}}{\sqrt{\frac{2}{3}R'E_0'} - T_e^{1/2}}\right)\right|_{T_{e0}}^{T_e} = A\tau \tag{2.45}
$$

After substituting the limits of integration and rearranging, the solution is

$$
\begin{aligned}
A\tau &= \left(\frac{2}{3}R'E_0'\right)^{3/2} \times \\
&\left\{\ln\left(\frac{\sqrt{\frac{2}{3}R'E_0'} + T_e^{1/2}}{\sqrt{\frac{2}{3}R'E_0'} - T_e^{1/2}}\frac{\sqrt{\frac{2}{3}R'E_0'} - T_{e0}^{1/2}}{\sqrt{\frac{2}{3}R'E_0'} + T_{e0}^{1/2}}\right) - \frac{2\left(T_e^{1/2} - T_{e0}^{1/2}\right)}{\left(\frac{2}{3}R'E_0'\right)^{1/2}} - \frac{2}{3}\frac{\left(T_e^{3/2} - T_{e0}^{3/2}\right)}{\left(\frac{2}{3}R'E_0'\right)^{3/2}}\right\}
\end{aligned}
\tag{2.46}
$$

Assuming further that the incident particles reach an equilibrium with the plasma electrons; i.e. $E = \frac{3}{2}T_e$, the following equilibrium expression can be obtained from Eq. (2.41),

$$T_e = \frac{\frac{2}{3}R'E_0'}{1+R'} \tag{2.47}$$

Replacing T_e in Eq. (2.46) with Eq. (2.47) gives the following *equilibrium* relationship between the heating time and the ratio R' .

$$A\tau = \left(\frac{2}{3}R'E_0'\right)^{3/2} \times$$
$$\left\{\ln\left(\frac{\sqrt{1+R'}+1}{\sqrt{1+R'}-1}\frac{\sqrt{\frac{2}{3}R'E_0'}-T_{e0}^{1/2}}{\sqrt{\frac{2}{3}R'E_0'}+T_{e0}^{1/2}}\right) - \frac{2}{(1+R')^{1/2}} - \frac{2}{3}\frac{1}{(1+R')^{3/2}} + \frac{2T_{e0}^{1/2}}{\left(\frac{2}{3}R'E_0'\right)^{1/2}}\left[1+\frac{T_{e0}}{2R'E_0'}\right]\right\} \tag{2.48}$$

2.4.3.2 The Heating Process

The D-T plasma electrons are assumed to have an initial temperature of 13.6 eV, corresponding to the ionization potential of deuterium/tritium. An antiproton beam is introduced, and "at-rest" annihilation takes place on a uranium-238 target, releasing charged pions as part of the annihilation products. In addition, the energy released from the annihilation causes uranium fission, giving rise to fission fragments.

The charged pions are assumed to be responsible for the first stage of heating of the plasma electrons. Energy transfer from the charged pions to plasma electrons is governed by Eq. (2.46), with the constraint that the heating time must equal the mean (laboratory) life time of charged pions, namely 2.6×10^{-8} seconds. Equilibrium; i.e. Eq.(2.47), between the charged pions and plasma electrons is **not** assumed.

The charged pions then decay into muons, which are assumed to be responsible for the second stage of heating. Energy transfer is again governed by Eq. (2.46), and the constraint here is that the heating time must equal the mean (laboratory) life time of muons, namely 2.2×10^{-6} seconds. As in the case with pions, equilibrium between muons and plasma electrons is **not** assumed.

The fission fragments are then assumed to be responsible for the remainder of the heating required to raise the electrons to the desired temperature. Equilibrium between fission fragments and plasma electrons **is** assumed since the fission fragments do not decay, and Eq. (2.48) is taken as the governing equation for energy transfer from the fission fragments to the plasma electrons, with the heating time being one of the unknown quantities.

The ratio of antiproton density to electron density (i.e. *R*) is another unknown quantity. The three heating equations governing heating by charged pions, muons, and fission fragments must therefore be solved simultaneously for the same value of *R*. An iteration algorithm in Matlab was implemented towards this end. The total heating time is then given by sum of the charged pion lifetime, the muon lifetime, and the fission fragment heating time that is determined from Eq. (2.48).

Once the plasma electrons are heated to the desired temperature, energy transfer from the electrons to DT ions is then assumed to occur in a characteristic thermalization time, given by the following:

$$\begin{aligned} \tau_{ei} &= 1/\nu_{ei} \\ \nu_{ei} &= \frac{3.2\times10^{-9} Z_i^2 n \ln\Lambda}{\left(m_i/m_p\right)T_e^{3/2}} \end{aligned} \tag{2.49}$$

where n is the electron density in cm^{-3}, T_e is the electron temperature in eV, Z_i is the charge state of the ions, m_i is the ion mass, m_p is the proton mass, and the Coulomb logarithm $\ln \Lambda$ is given by Eq. (2.39).

2.4.3.3 Sample Calculations

For an electron density of 5×10^{16} cm^{-3} and a final temperature of 10 keV, the fission fragment heating time comes out to be approximately 1.95×10^{-4} seconds, giving a total heating time of approximately 2.01×10^{-4} seconds. The electron-ion thermalization time, on the other hand, is approximately 1.11×10^{-3} seconds. The number of incident particles (pions, muons, and fission fragments) per electron (i.e. R') is approximately 8.3×10^{-5}, giving a ratio R of antiproton density to electron density of 4.15×10^{-5}, or an antiproton density of 2.07×10^{12} cm^{-3} for an electron density of 5×10^{16} cm^{-3}. Table 2.2 summarizes the main results for other densities and temperatures.

$n =$ $T_e =$	5×10^{17} cm^{-3} 10 keV	10^{17} cm^{-3} 10 keV	5×10^{16} cm^{-3} 10 keV	10^{16} cm^{-3} 10 keV	10^{16} cm^{-3} 5 keV
τ_H (sec)	2.82×10^{-5}	1.07×10^{-4}	2.01×10^{-4}	9.00×10^{-4}	3.74×10^{-4}
τ_{ei} (sec)	1.21×10^{-4}	5.69×10^{-4}	1.11×10^{-3}	5.24×10^{-3}	1.95×10^{-3}
$n_{\bar{p}}$ (cm^{-3})	1.18×10^{13}	3.45×10^{12}	2.07×10^{12}	5.88×10^{11}	2.39×10^{11}

Table 2.2. Comparison of the heating time and electron-ion thermalization time, and the amount of antiprotons needed to achieve the indicated electron temperatures for various densities. Note that τ_H is the total heating time, including pion, muon and fission fragment heating.

2.4.4 Alpha Particle Dynamics

The previous section outlines a scheme whereby a fusion GDM can reach ignition temperature. Subsequently, the fusion energy released in the form of charged particles (alpha particles for D-T cycle) keep the system self-sustained. Due to the presence of negative muons created as a result of the antiproton annihilation, there is a possible additional contribution to the initial heating of the system. Frank [35] in 1947 noted that negative muons might be able to catalyze proton-deuterium fusion, which was experimentally observed by Alvarez *et al.* [36] in 1956. D-T fusion catalyzed by muons was discussed by Zel'dovich and Sakharov [37], and later Jackson [38] concluded that the D-T interaction has the highest possibility of catalyzed fusion. Analyses and measurements [39,40] showed that on average one negative muon can catalyze about 100 D-T fusion reactions in its lifetime in a dense D-T mixture. Due to muon catalysis, fusion reactions can take place in a cold plasma, resulting in the production of 3.5 MeV alpha particles that can potentially contribute to initial heating of the plasma before ignition. The catalysis mechanism was summarized in Ref. [41]. On the basis of energetics alone, muon-catalyzed fusion has the potential to reduce the amount of antiprotons required to achieve a thermonuclear burn by about 60%.

Of course, energetics alone does not address the issue of alpha particle confinement in the GDM. For alpha particle heating to be useful, a sufficient number of these alpha particles would need to deposit their energy into the plasma through collisions before escaping from the system. In this section, this will be analyzed quantitatively by allowing for escape while the alpha particles slow down on the plasma particles. Assuming that alpha particle confinement follows that of the lighter deuterium and tritium ions, the appropriate expressions will be deduced for their velocity distribution, mean energy, and confinement time in the GDM.

2.4.4.1 Energy Distribution

The number of alpha particles in an interval of energy ΔE is $n_\alpha(E)\Delta E$, where $n_\alpha(E)$ is the energy distribution function representing the number density per unit energy. If a loss mechanism has a time constant $\tau(E)$, then the steady-state loss rate equation is

$$\frac{d}{dt}\left[n_\alpha(E)\Delta E\right] = n_\alpha(E)\left(\frac{dE}{dt}\right)_E - n_\alpha(E+\Delta E)\left(\frac{dE}{dt}\right)_{E+\Delta E} - \frac{n_\alpha(E)\Delta E}{\tau(E)} = 0 \qquad (2.50)$$

Figure 2.20 illustrates the meaning of each term. Since dE/dt represents energy loss and is implicitly a negative quantity, this explains the negative signs in the figure. The first term in Eq. (2.50) represents alpha particle loss due to them slowing down to below the energy range *E* and *E* + *ΔE*. The second term represents gain due to alpha particles slowing down to the range *E* and *E* + *ΔE*. Finally, the last term represents alpha particles that escape from the system. Rearranging the equation and using the definition of a derivative, the following governing differential equation is obtained for the energy distribution of alpha particles.

$$\frac{\partial}{\partial E}\left(n_\alpha \frac{dE}{dt}\right) + \frac{n_\alpha(E)}{\tau(E)} = \frac{\partial n_\alpha}{\partial E}\left(\frac{dE}{dt}\right) + n_\alpha(E)\frac{\partial}{\partial E}\left(\frac{dE}{dt}\right) + \frac{n_\alpha(E)}{\tau(E)} = 0 \qquad (2.51)$$

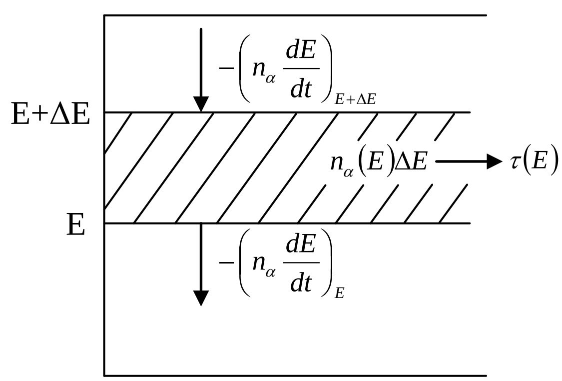

Figure 2.20. Alpha particle flux balance.

Integrating Eq. (2.51) over the range of energies *E* to E_0, where E_0 is the initial energy (i.e. birth energy) of the alpha particles, yields the following:

$$n_\alpha(E) = n_\alpha(E_0)\exp\left\{\int_E^{E_0}\left[\frac{\frac{\partial}{\partial E}\left(\frac{dE}{dt}\right)}{dE/dt} + \frac{1}{\tau(E)\frac{dE}{dt}}\right]dE\right\} \tag{2.52}$$

The first term of the integrand can be rewritten as follows

$$\frac{\frac{\partial}{\partial E}\left(\frac{dE}{dt}\right)}{dE/dt} = \frac{d}{dE}\left[\ln\left(\frac{dE}{dt}\right)\right] \tag{2.53}$$

and can be readily integrated yielding the following expression for the alpha particle energy distribution.

$$n_\alpha(E) = n_\alpha(E_0)\frac{\left(dE/dt\right)_{E_0}}{dE/dt}\exp\left\{\int_E^{E_0}\frac{1}{\tau(E)\,dE/dt}dE\right\} \tag{2.54}$$

Now consider alpha particles produced via muon-catalyzed fusion. The initial energy distribution would be given by the following:

$$n_\alpha(E_0) = \frac{\left(c_\mu n_\mu\right)/\tau_\mu}{-\left(dE/dt\right)_{E_0}} \tag{2.55}$$

where n_μ is the negative muon number density, τ_μ is the muon lifetime, and c_μ is the number of catalyzed fusions (i.e. number of alpha particles born) per negative muon. The rate of decrease of alpha particle energy dE/dt can be expressed by Eq. (2.56), with the first term denoting energy loss to the plasma electrons and the second term denoting energy loss to the ions due to Coulomb collisions.

$$\frac{dE}{dt} = -\left(c_1 E + \frac{c_2}{\sqrt{E}}\right) \tag{2.56}$$

The coeffieients c_1 and c_2 depend on the type of incident and target particles, as well as plasma density and temperature.

$$c_1 = \frac{8}{3}\sqrt{2\pi}Z^2 Z_e^2 e^4 (\ln\Lambda)\frac{\sqrt{m_e}}{T_e^{3/2}}\frac{n_e}{m}C_a \qquad [\mathrm{s}^{-1}]$$
$$C_a = \left(1.6022\times10^{-9}\right)^{-3/2}\left(\frac{\mathrm{keV}}{\mathrm{erg}}\right)^{3/2} \tag{2.57}$$

where m and m_e are respectively the mass of the incident particle (i.e. alpha particle) and the electron. Similarly, Z and Z_e are the charge state of the incident particle (i.e. alpha particle) and the electron, respectively. The electron density is n_e, and T_e is the electron temperature. Equation (2.57) is written in the CGS system, and all the quantities are in standard CGS units, with the exception of the electron temperature T_e. For convenience, T_e in Eq. (2.57) has units of *keV*. The conversion factor C_a makes explicit the conversion to the CGS system. Finally, ln Λ is the same Coulomb Logarithm given by Eq. (2.39).

Similarly for c_2, Eq. (2.58) is written in the CGS system, and all quantities have their standard CGS units. The conversion factor C_b ensures that c_2 has the correct energy unit of keV in order to be consistent with the other equations.

$$c_2 = \frac{4\pi Z^2 Z_i^2 e^4 (\ln\Lambda) n_i}{m_i}\sqrt{\frac{m}{2}}C_b \qquad \left[\frac{\mathrm{keV}^{3/2}}{\mathrm{s}}\right]$$
$$C_b = \left(1.6022\times10^{-9}\right)^{-3/2}\left(\frac{\mathrm{keV}}{\mathrm{erg}}\right)^{3/2} \tag{2.58}$$

Substituting Eqs. (2.55) and (2.56) into Eq. (2.54) yields the following energy distribution for alpha particles produced via muon-catalyzed fusion, where E has unit *keV*.

$$n_\alpha(E) = \frac{(c_\mu n_\mu)/\tau_\mu}{c_1 E + \frac{c_2}{\sqrt{E}}} \exp\left\{ -\int_E^{E_0} \frac{\sqrt{E}}{\left(c_1 E^{3/2} + c_2\right)\tau(E)} dE \right\} \tag{2.59}$$

To evaluate Eq. (2.59), we need the time constant (i.e. confinement time) $\tau(E)$. The confinement time for the GDM, ignoring the ambipolar potential, is given by,

$$\tau(E) = \frac{R_p L}{v} \tag{2.60}$$

Here R_p is the plasma mirror ratio, which is the ratio of the magnetic field seen by the plasma at the mirror to that at the center. The monoenergetic particle velocity is given by Eq. (2.61).

$$v = \sqrt{\frac{2EC_c}{m_\alpha}} \qquad C_c = 1.6022 \times 10^{-9} \text{ erg/keV} \tag{2.61}$$

where m_α is the mass of the alpha particle, and C_c is a unit conversion factor allowing E in Eq. (2.61) to be expressed in *keV* in order to be consistent with Eq. (2.59). All the other quantities in Eqs. (2.60) and (2.61) have the standard CGS units to be consistent with Eqs. (2.57) and (2.58). Substituting these equations into Eq. (2.59) yields the final expression for the energy distribution for alpha particles produced via muon-catalyzed fusion inside the GDM,

$$n_\alpha(E) = \frac{(c_\mu n_\mu)/\tau_\mu}{c_1 E + \frac{c_2}{\sqrt{E}}} \exp\left\{ -\sqrt{\frac{2C_c}{m_\alpha}} \frac{1}{R_p L} \int_E^{E_0} \frac{E}{c_1 E^{3/2} + c_2} dE \right\} \quad \left[\mathrm{cm}^{-3} \cdot \mathrm{keV}^{-1}\right] \tag{2.62}$$

2.4.4.2 Electron Heating Only

The analytical solution to the full integral in Eq. (2.62) is very complicated. For a relatively cold plasma, e.g. at the ionization temperature, c_1 can be several orders of magnitude larger than c_2. Therefore, electron heating dominates, which is what is expected for a cold plasma. If we envision a GDM system wherein these alpha particles produced via muon-catalyzed D-T fusion reactions contribute to the initial phase of the plasma heating, it is reasonable to assume that the bulk of their energy is deposited into the plasma electrons. The integral in Eq. (2.62) can therefore be simplified by assuming $c_2 = 0$, so that

$$n_\alpha(E) = \frac{(c_\mu n_\mu)/\tau_\mu}{c_1 E} \exp\left\{ -\sqrt{\frac{2C_c}{m_\alpha}} \frac{1}{R_p L} \int_E^{E_0} \frac{dE}{c_1 E^{1/2}} \right\} \tag{2.63}$$

The resulting integral can be easily evaluated, yielding the following distribution function:

$$\begin{aligned} n_\alpha(E) &= \frac{c_\mu n_\mu}{c_1 E \tau_\mu} \exp\left\{ -\sqrt{\frac{2C_c}{m_\alpha}} \frac{2}{R_p L c_1} \left(\sqrt{E_0} - \sqrt{E}\right) \right\} \\ &= \frac{c_\mu n_\mu}{c_1 E \tau_\mu} \exp\left\{ -A\left(\sqrt{E_0} - \sqrt{E}\right) \right\} \end{aligned} \tag{2.64}$$

Here, the quantity A (not to be confused with A in Eq. (2.38)) was defined as

$$A \equiv \sqrt{\frac{2C_c}{m_\alpha}} \frac{2}{R_p L c_1} > 0 \quad \left[\mathrm{keV}^{-1/2}\right] \tag{2.65}$$

Inspecting Eq. (2.64) shows that the distribution behaves as follows.

$$n_\alpha(E) \sim \frac{e^{A\sqrt{E}}}{E} \tag{2.66}$$

For relatively small energy E, $1/E$ dominates, whereas for large E, the exponential dominates. The minimum of the distribution occurs at an energy $E_{\min}$, given by

$$E_{\min} = \frac{4}{A^2} \tag{2.67}$$

Since the energy of the alpha particles will be bounded by E_{th} (thermal energy) and E_0 (initial energy at birth; i.e. 3.5 MeV), only this portion of $n_\alpha(E)$ is meaningful. Using typical orders of magnitude for the defined quantity A; i.e. 10^{-3} to 10^{-5} for a dense cold plasma, it can be seen that the distribution lies significantly to the left of the minimum, where $1/E$ dominates. Figure 2.21 shows a representative plot of the distribution function for this range of energies.

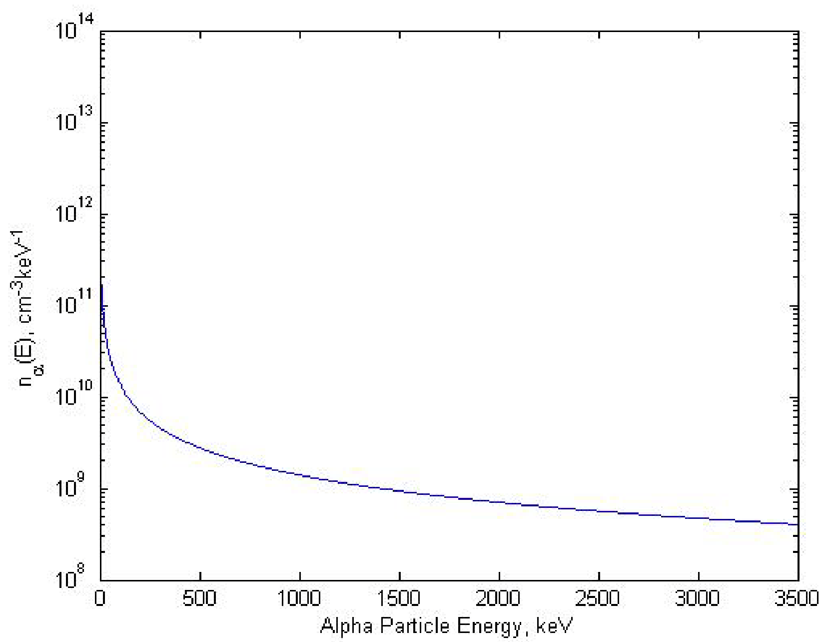

Figure 2.21. Typical profile for the alpha particle energy distribution function.

2.4.4.3 Confined Alpha Particle Density

To obtain the total number density, the distribution, Eq. (2.64), was integrated over all energies between the lower and upper bounds, giving

$$N_\alpha = \int_{E_{th}}^{E_0} n_\alpha(E)dE = \frac{c_\mu n_\mu}{c_1 \tau_\mu} e^{-A\sqrt{E_0}} \int_{E_{th}}^{E_0} \frac{e^{A\sqrt{E}}}{E} dE \tag{2.68}$$

A change of variable transforms the integral in Eq. (2.68) into

$$\begin{aligned} N_\alpha &= \frac{2c_\mu n_\mu}{c_1 \tau_\mu} e^{-A\sqrt{E_0}} \int_{-A\sqrt{E_{th}}}^{-A\sqrt{E_0}} \frac{e^{-z}}{z} dz \\ &= \frac{2c_\mu n_\mu}{c_1 \tau_\mu} e^{-A\sqrt{E_0}} \left[-\int_{-A\sqrt{E_0}}^{\infty} \frac{e^{-z}}{z} dz + \int_{-A\sqrt{E_{th}}}^{\infty} \frac{e^{-z}}{z} dz \right] \end{aligned} \tag{2.69}$$

Each of the integrals in Eq. (2.69) is defined as the “exponential integral function” and is denoted by Ei. Therefore, the total density assuming electron heating only is given by the following.

$$N_\alpha = \frac{2c_\mu n_\mu}{c_1 \tau_\mu} e^{-A\sqrt{E_0}} \left[Ei\left(A\sqrt{E_0}\right) - Ei\left(A\sqrt{E_{th}}\right) \right] \quad \left[\mathrm{cm}^{-3}\right] \tag{2.70}$$

2.4.4.4 Mean Kinetic Energy

The mean alpha energy can be calculated as follows.

$$\overline{E}_\alpha = \frac{\int_{E_{th}}^{E_0} E n_\alpha(E)dE}{N_\alpha} = \frac{\frac{c_\mu n_\mu}{c_1 \tau_\mu} e^{-A\sqrt{E_0}} \int_{E_{th}}^{E_0} e^{A\sqrt{E}} dE}{N_\alpha} \equiv \frac{I}{N_\alpha} \tag{2.71}$$

The integral I can be readily evaluated by first making a variable substitution $x \equiv A\sqrt{E}$ and then using integration by parts, so that

$$I = \frac{2c_\mu n_\mu}{A^2 c_1 \tau_\mu} e^{-A\sqrt{E_0}} \left[e^{A\sqrt{E_0}} \left(A\sqrt{E_0} - 1 \right) - e^{A\sqrt{E_{th}}} \left(A\sqrt{E_{th}} - 1 \right) \right] \tag{2.72}$$

The final expression for the mean alpha particle energy is thus

$$\overline{E}_\alpha = \frac{e^{A\sqrt{E_0}} \left(A\sqrt{E_0} - 1 \right) - e^{A\sqrt{E_{th}}} \left(A\sqrt{E_{th}} - 1 \right)}{A^2 \left[Ei\left(A\sqrt{E_0} \right) - Ei\left(A\sqrt{E_{th}} \right) \right]} \quad [\mathrm{keV}] \tag{2.73}$$

2.4.4.5 Sample Calculations

As before, the calculation here assumed a D-T plasma with density 5×10^{16} cm^{-3} at an initial temperature of 13.6 eV, which corresponds to the ionization potential of the propellant. Each negative muon created as a result of “at-rest” antiproton annihilation on average has the potential to catalyze approximately 100 D-T fusion reactions, each releasing an alpha particle of 3.5 MeV of kinetic energy that further contributes to the initial phase of plasma heating.

For a GDM with an antiproton density of 2.07×10^{12} cm^{-3} (based upon heating requirements described in Section 2.4.3) yielding an initial alpha particle density of 2.07×10^{14} cm^{-3}, the number of alpha particles being confined is about 1.68×10^{13} cm^{-3}. The mean energy of these confined alpha particles is roughly 294 keV.

To determine the change in plasma temperature, consider the simple energy balance

$$\frac{3}{2} n_e \left(T_e - T_{e0} \right) = n_{inc} \left(E_0 - E \right) \tag{2.74}$$

where n_{inc} is the incident particle density (i.e. alpha particles in the current analysis), and the subscript *0* denotes initial values.

If the confined alpha particles are assumed to deposit almost all of their energy into the plasma electrons (i.e., they slow down from their birth energy of 3.5 MeV to a final average kinetic energy $E = (3/2)T = 20.4\,\mathrm{eV}$, corresponding to a temperature of 13.6 eV, on the electrons), then the change in the electron temperature is $\Delta T_e = 784\,\mathrm{eV}$. This represents the maximum heating produced by these alpha particles.

Alternately, as a more conservative estimate, if the confined alpha particles are assumed to slow down on the electrons until they reach their mean kinetic energy of 294 keV, then the corresponding change in the electron temperature is $\Delta T_e = 718\,\mathrm{eV}$. From Eq. (2.74), it can be seen that

$$\Delta T_e \sim \frac{n_{inc}}{n_e} \Delta E \tag{2.75}$$

Since ΔE is more-or-less fixed, the important factor is the density ratio. Increasing this ratio, either by increasing antiproton density or by decreasing electron density, can result in a ΔT_e of multiple keVs. Of course, due to the heating requirements, these two densities are not necessarily independent. For example, changing the electron density will change the minimum antiproton density required; as a result, the negative muon density (and hence the confined alpha particle density) will change as well. However, one can increase the antiproton density beyond the minimum required value dictated by the heating requirements to produce a larger ΔT_e, if this is desired – and if the associated increase in cost of obtaining and confining the antiprotons is not prohibitive.

In summary, it was found that although there are particle losses, the number of alpha particles remaining in the GDM (and the resulting heating they contribute) is nevertheless significant. For a given plasma density, one can increase the antiproton density, causing the amount of heating to increase as a result of increased density of confined alpha particles. For instance, in the above calculations, doubling the amount of antiprotons will result in an approximately 1.5 keV increase in the electron temperature. The mean energy, however, will remain the same for a given plasma density, as will the percentage of alpha particles confined

Another way to increase the contributed heating is to increase the percentage of confined alpha particles. Brief calculations have shown that this percentage increases as the plasma density decreases. For instance, when $n_e = 1 \times 10^{16}$ cm^{-3}, the percentage of alpha particles confined long enough to heat the plasma increases 4-fold compared to the calculations above (with $n_e = 5 \times 10^{16}$ cm^{-3}). The associated heating increases significantly with decreasing plasma density as well. The tradeoff, however, is that the plasma dynamics inside the GDM dictate a rapid increase in the plasma length with decreasing plasma density, and the system soon becomes prohibitively massive.

Chapter 3

Plasma Dynamics inside the GDM

3.1 Physics-Based Model

In this chapter, the physics-based model that describes the plasma dynamics inside the GDM will be presented. The initial rapid loss of the electrons out of the system establishes an electrostatic potential, and the particle dynamics is heavily influenced by the electric field associated with this potential. Therefore, in order to identify the forces that contribute to the flow of particles through the mirrors, one must incorporate not only the diffusion due to collisions, but also the contribution of the electric field. Another aspect to consider is that the GDM needs to have an asymmetric mirror ratio in order to bias the direction of particle escape toward the thrusting end of the device. This is achieved by properly controlling the mirror ratio at both ends.

3.1.1 Ambipolar Potential and Loss Rate

The derivation begins with the monoenergetic diffusion equations for the electrons and ions in the device [42].

$$\left(1/R_j\right)\gamma_{ej} = -D_e \nabla n_e - \mu_e \vec{E} n_e \tag{3.1}$$

$$\left(1/R_j\right)\gamma_{ij} = -D_{ij} \nabla n_i - \mu_i Z \vec{E} n_i \tag{3.2}$$

where the mirror ratio reflects the fact that the monoenergetic flux γ is measured at the throat of the mirror with area A_0. The subscript *j* denotes the corresponding quantity at the two mirrors. If the plasma area at the center of the device is A_c, then $A_0 = A_c / R$. It is assumed that the ion and electron densities vary as

$$n = n_c \exp[-(2k/L)z] \tag{3.3}$$

where *L* is the axial length of the system, and *k* is an integer density length scale. It is clear that one can write for the total monoenergetic flux through the mirror the result

$$A_0 \gamma = -A_0 D \nabla n = (2k/L) A_0 D n \tag{3.4}$$

For the ions, the following diffusion coefficient is employed,

$$D_{ij} = \frac{L^2}{4k\tau_j} \tag{3.5}$$

where τ_j is the loss time constant for mirror ratio R_j. The approximate loss time constant for ions τ_{ij} is given by the Eq. (3.6). Note that this is based on flux balance and expresses the loss rate assuming all of the ions escape through *one* end of the GDM with mirror ratio R_j in the absence of any electric field.

$$\tau_{ij} = \frac{R_j L}{v_{th}} \tag{3.6}$$

For the electrons, the following diffusion coefficient is used,

$$D_e = \frac{v_e^2}{3\nu_{ei}} \tag{3.7}$$

where ν_{ei} is an electron-ion collision frequency given by

$$\nu_{ei} = \frac{n_e \ln \Lambda}{C_0 E_e^{3/2}} \tag{3.8}$$

with the constant $C_0 = 8.176 \times 10^9 \text{ s cm}^{-3} \text{ keV}^{-3/2}$. In addition, the following definitions are used for the mobilities appearing in Eqs. (3.1) and (3.2).

$$\mu_e = \frac{e}{m_e \nu_{ei}} \tag{3.9}$$

$$\mu_i = \frac{Ze}{m_i \nu_{ei}} \tag{3.10}$$

If one assumes that the electrostatic potential varies in space in the same manner as the electron and ion densities, the electric field becomes

$$\vec{E} = -\nabla \phi = (2k/L)\phi \tag{3.11}$$

With this assumption, the monoenergetic fluxes given by Eqs. (3.1) and (3.2) can be rewritten as

$$\gamma_{ej} = \frac{2kn_e R_j}{m_e L \nu_{ei}} \left(\frac{1}{3} m_e v_e^2 - e\phi \right) \tag{3.12}$$

$$\gamma_{ij} = \frac{1}{2} n_i \left(v_i + \frac{4kR_j}{m_e L \nu_{ei}} \frac{m_e}{m_i} Z^2 e\phi \right) \tag{3.13}$$

Note that for small electron speed v_e, the electron flux becomes negative, which is physically unrealistic (since there is no source external to the system to produce this return flow). As a result, the following condition is set as the lower limit on Eq. (3.12):

$$\gamma_{ej} = 0 \text{ for } v_e < \sqrt{\frac{3e\phi}{m_e}} \tag{3.14}$$

Since the ion flux is always positive, the lower limit on Eq. (3.13) is zero.

Because the plasma in GDM is highly collisional, it is reasonable to assume that the species are Maxwellian. The total electron and ion fluxes Γ_{ej} and Γ_{ij} can therefore be found by multiplying Eqs. (3.12) and (3.13) by the respective Maxwell-Boltzmann velocity distribution and then integrating over all velocities, giving

$$\Gamma_{ej} = \frac{2R_j k n_e T_e}{m_e L \nu_{ei}} \left\{ \left(1 - \frac{e\phi}{T_e}\right)\left[1 - erf\left(\sqrt{\frac{3e\phi}{2T_e}}\right)\right] + \frac{2}{\sqrt{\pi}}\sqrt{\frac{3e\phi}{2T_e}} \exp\left(-\frac{3e\phi}{2T_e}\right)\right\} \tag{3.15}$$

$$\Gamma_{ij} = \frac{2R_j k n_i T_i}{m_e L \nu_{ei}} \left[\frac{m_e L \nu_{ei}}{4R_j k T_i}\left(\frac{8T_i}{\pi m_i}\right)^{1/2} + \frac{m_e}{m_i} Z^2 \frac{e\phi}{T_i}\right] \tag{3.16}$$

The condition of charge neutrality requires that the charged flux losses be equal and the net charge be zero; i.e.,

$$\begin{aligned} \Gamma_j &\equiv \Gamma_{ej} = Z\Gamma_{ij} \\ n &\equiv n_e = Z n_i \end{aligned} \tag{3.17}$$

Upon satisfying these conditions and defining the following quantities,

$$\begin{aligned} \delta_j &\equiv \frac{L}{4R_j k} m_e \nu_{ei} \left(\frac{8T_i}{\pi m_i}\right)^{1/2} \\ x &\equiv \sqrt{\frac{3e\phi}{2T_e}} \end{aligned} \tag{3.18}$$

the following balance equation is obtained for the electrostatic potential ϕ,

$$\left(1 - \frac{2}{3}x^2\right)\left[1 - erf(x)\right] + \frac{2}{\sqrt{\pi}} x e^{-x^2} = \frac{\delta_j}{T_e} + \frac{2}{3}\frac{m_e}{m_i} Z^2 x^2 \tag{3.19}$$

where T_e and T_i are the electron and ion temperatures and $erf(x) = \left(2/\sqrt{\pi}\right)\int_0^x e^{-t^2}\,dt$ is the error function.

Recall that Eq. (3.19) corresponds to two equations for the two “mirrors”, one for j = 1 and one for j = 2. In general, the potentials that satisfy the two are different. However, unlike fluxes, there is only one potential present inside the GDM. As a result, the two equations resulting from Eq. (3.19) are combined to obtain Eq. (3.20), which is then used to determine the ambipolar potential inside the GDM.

$$\left(1-\frac{2}{3}x^2\right)\left[1-erf(x)\right]+\frac{2}{\sqrt{\pi}}xe^{-x^2} = \frac{\delta_1+\delta_2}{2T_e}+\frac{2}{3}\frac{m_e}{m_i}Z^2x^2 \tag{3.20}$$

Rearranging Eq. (3.5) yields an expression for the loss time constant as

$$\tau_j = \frac{L^2}{4kD_{ij}} \tag{3.21}$$

where the diffusion coefficient D_{ij} given by Eq. (3.22) is obtained from the condition $(1/R_j)\Gamma_j = -D_{ij}\nabla n = (2k/L)D_{ij}n$, together with the expressions for total ion flux Eq. (3.16) and number density Eq. (3.17):

$$D_{ij} = \frac{1}{m_e \nu_{ei}}\left[\delta_j + \frac{m_e}{m_i}Z^2 e\phi\right] \tag{3.22}$$

Writing the following for the ion thermal velocity,

$$v_{th} = \sqrt{\frac{8T_i}{\pi m_i}} \tag{3.23}$$

and using this to rewrite δ_j in terms of τ_{ij} in Eq. (3.22), the resulting expression for the ion diffusion coefficient can be equated to Eq. (3.5); i.e.,

$$D_j = \frac{L^2}{4k\tau_{ij}}\left[1+\frac{m_e}{m_i}Z^2\frac{e\phi}{\delta_j}\right] = \frac{L^2}{4k\tau_j} \tag{3.24}$$

From this one obtains the loss time constant (or equivalently the confinement time)

$$\tau_j = \frac{\tau_{ij}}{1+(m_e/m_i)Z^2(e\phi/\delta_j)} \tag{3.25}$$

Note that when the potential ϕ is neglected, the characteristic confinement time reduces to that given by Eq. (3.6), which was used in previous studies of the GDM [18]. Again as before, Eq. (3.25) expresses the loss rate assuming that *all* the ions escape through one end of the GDM with mirror ratio R_j. The total loss rate can be written as follows.

$$\frac{1}{\tau} = \frac{1}{\tau_1} + \frac{1}{\tau_2} \tag{3.26}$$

For the potential-less case, when the two mirror ratios are the same, Eq. (3.26) reduces (as it should) to the expression given in Eq. (2.14).

3.1.2 Average Particle Escape Energy

It should be noted that in Eq. (3.20), the mirror ratio *R* appears only in the ion dynamics term. This is because only the ions respond to mirror confinement, as noted earlier. Moreover, $T_e \neq T_i$ in a GDM, because electrons with energies above that of the potential escape, causing the electron distribution to become (in effect) a "truncated" Maxwellian. The potential is obtained by iterative solution of Eq. (3.20), and it can be used to evaluate the electron and ion escape energies, given by

$$E_{Le} = \frac{(5-2x^2)[1-erf(x)] + \frac{2}{\sqrt{\pi}}\left(5+\frac{4}{3}x^2\right)xe^{-x^2}}{2\left(1-\frac{2}{3}x^2\right)[1-erf(x)] + \frac{4}{\sqrt{\pi}}xe^{-x^2}} T_e \tag{3.27}$$

$$E_{Lij} = \frac{2 + \frac{m_e}{m_i} Z^2 \frac{T_e}{\delta_j} x^2}{1 + \frac{2}{3} \frac{m_e}{m_i} Z^2 \frac{T_e}{\delta_j} x^2} T_i \tag{3.28}$$

The above expressions are obtained by multiplying Eqs. (3.12) and (3.13) by the respective kinetic energy and then integrating over the Maxwell-Boltzmann velocity distribution.

It should be noted that the average electron escape energy for asymmetric mirrors, given by Eq. (3.27), is the same as in the case for symmetric mirrors. Again, this is expected since the electrons have such small mass and high velocity that they essentially do not *see* the mirrors. On the other hand, the average ion escape energy has the same expression as that for symmetric mirrors, but due to its dependence on the mirror ratio, the escape energy will be different at both ends of an asymmetric GDM. Also note that if the potential is ignored, the electron and ion escape energies reduce to

$$E_{Le} = \frac{5}{2} T_e \text{ and } E_{Lij} = 2T_i \tag{3.29}$$

which agree with previous results [18]. Furthermore, since E_{Le} and E_{Lij} are the average energies of escaping electrons and ions as they leave the plasma chamber, the ambipolar potential must be added (subtracted) to the ion (electron) energy to obtain their energies outside the chamber. Therefore, the average energy of an escaped electron outside the plasma chamber is $(E_{Le} - e\phi)$ and that of an escaped ion is $(E_{Lij} + e\phi)$.

3.1.3 Conservation Equations

Recall that the total loss time constant for an asymmetric GDM is given by Eq. (3.26). The loss rates τ_1 and τ_2 associated with mirror ratios R_1 and R_2 are given by

Eq. (3.25). Knowing this, one can now write the ion and electron power balance equations in steady state for an asymmetric GDM as

Electron: $$SE_{in} f_{ie} + n^2 W_{ie} + P_\alpha f_{\alpha e} = \left(\frac{n}{\tau_1} + \frac{n}{\tau_2} \right) E_{Le} + P_r \tag{3.30}$$

Ion: $$SE_{in} f_{ii} + P_\alpha f_{\alpha i} = \frac{n}{\tau_1} E_{Li1} + \frac{n}{\tau_2} E_{Li2} + n^2 W_{ie} \tag{3.31}$$

In these equations, S is the rate of injection of fuel ions per unit volume, E_{in} is the energy of the injected particles, W_{ie} is the energy exchange rate from the ions to the electrons, P_r is the radiative (Bremsstrahlung and synchrotron) power, and P_α is the alpha power given by

$$P_\alpha = \frac{1}{4} n^2 \langle \sigma v \rangle E_\alpha \tag{3.32}$$

with $E_\alpha = 3.5\,\text{MeV}$.

As a fusion alpha particle slows down, it gives a fraction $f_{\alpha i}$ of its energy to the plasma ions and a fraction $f_{\alpha e} = 1 - f_{\alpha i}$ to the electrons. Similarly, the injection energy E_{in} of the source ions is divided with a fraction f_{ii} going to the ions and $f_{ie} = 1 - f_{ii}$ to the electrons. Adding Eq. (3.30) to Eq. (3.31) gives the total (electron + ion) power balance.

$$SE_{in} + P_\alpha = \frac{n}{\tau_1} \left(E_{Li1} + E_{Le} \right) + \frac{n}{\tau_2} \left(E_{Li2} + E_{Le} \right) + P_r \tag{3.33}$$

Finally, the steady state mass (particle) balance equation is simply

$$S = n \left(\frac{1}{\tau_1} + \frac{1}{\tau_2} \right) + \frac{n^2}{2} \langle \sigma v \rangle \tag{3.34}$$

where the left hand side term S represents the particle source and the right hand side represents losses due to particles escaping from the system and particles consumed by fusion.

3.1.4 Calculation of Plasma Length

In this section, the expression governing the length of the system will be derived. Defining the power

$$P \equiv SE_{in} + P_\alpha - P_r = \eta_i P_i + P_\alpha - P_r \tag{3.35}$$

where P_i is the specific injector power and η_i the injector efficiency, one can rewrite the total energy balance equation, Eq. (3.33), as

$$\frac{P}{n} = \frac{1}{\tau_1}\left(E_{Li1} + E_{Le}\right) + \frac{1}{\tau_2}\left(E_{Li2} + E_{Le}\right) \tag{3.36}$$

Defining the parameter Y_j

$$Y_j = \frac{T_e}{\delta_j} L \, , \; j = 1,2 \tag{3.37}$$

and the ion thermal speed,

$$v_{th} = \sqrt{\frac{8T_i}{\pi m_i}} \tag{3.38}$$

one can rewrite the confinement time and ion escape energy (i.e. Eqs. (3.25) and (3.28)) as

$$\tau_j = \frac{R_j L}{v_{th}\left(1 + \frac{2}{3}\frac{m_e}{m_i} Z^2 \frac{Y_j x^2}{L}\right)} \tag{3.39}$$

$$E_{Lij} = \frac{2 + \frac{m_e}{m_i} Z^2 \frac{Y_j x^2}{L}}{1 + \frac{2}{3}\frac{m_e}{m_i} Z^2 \frac{Y_j x^2}{L}} T_i \tag{3.40}$$

Inserting these two equations, along with the electron escape energy Eq. (3.27), into Eq. (3.36), one can obtain (after some algebra) the quadratic equation, Eq. (3.41), that the reactor length L satisfies for an asymmetric GDM to achieve self-sustained fusion.

$$\frac{P}{n}\frac{1}{v_{th}} L^2 - \left(\frac{1}{R_1} + \frac{1}{R_2}\right)(2T_i + E_{Le})L - \frac{2}{3}\frac{m_e}{m_i} Z^2 x^2 \left(\frac{Y_1}{R_1} + \frac{Y_2}{R_2}\right)\left(\frac{3}{2}T_i + E_{Le}\right) = 0 \tag{3.41}$$

Note from the definitions of δ_j in Eq. (3.18), Y_j and v_{th} in Eq. (3.37), one can show that

$$\frac{Y_1}{R_1} = \frac{Y_2}{R_2} = \frac{4kT_e}{m_e \nu_{ei} v_{th}} \tag{3.42}$$

Hence the third term in Eq. (3.41) can be rewritten in a slightly different form, giving for asymmetric mirrors.

$$\frac{P}{n}\frac{1}{v_{th}} L^2 - \left(\frac{1}{R_1} + \frac{1}{R_2}\right)(2T_i + E_{Le})L - \frac{4}{3}\frac{m_e}{m_i} Z^2 x^2 \frac{Y_1}{R_1}\left(\frac{3}{2}T_i + E_{Le}\right) = 0 \tag{3.43}$$

For symmetric mirrors, $R_1 = R_2 \equiv R$ and $Y_1 = Y_2 \equiv Y$, and thus Eq. (3.41) reduces to the following equation, which agrees with previous results.

$$\frac{1}{2}\frac{P}{n}\frac{R}{v_{th}} L^2 - (2T_i + E_{Le})L - \frac{2}{3}\frac{m_e}{m_i} Z^2 x^2 Y\left(\frac{3}{2}T_i + E_{Le}\right) = 0 \tag{3.44}$$

3.1.5 Relationship between Mirror Ratios and Fraction to Direct Converter

Now, we will develop a relationship between the mirror ratios at both ends of the asymmetric GDM and the fraction F of the power carried by escaping charged particles that is processed by the direct converter (leaving the fraction of $1-F$ available for thrust power).

Denoting the average power density of escaping charged particles by P_c, the direct converter power density by P_D, and the thrust power density by P_T yields the following.

$$P_D = FP_c \tag{3.45}$$

$$P_T = (1-F)P_c \tag{3.46}$$

Alternately, the direct converter power and thrust power can be expressed as follows,

$$P_D = \frac{n}{\tau_D}(E_{LiD} + e\phi) + \frac{n}{\tau_D}(E_{Le} - e\phi) = \frac{n}{\tau_D}(E_{LiD} + E_{Le}) \tag{3.47}$$

$$P_T = \frac{n}{\tau_T}(E_{LiT} + e\phi) + \frac{n}{\tau_T}(E_{Le} - e\phi) = \frac{n}{\tau_T}(E_{LiT} + E_{Le}) \tag{3.48}$$

where n is the electron (ion) density, τ_D and τ_T are ambipolar confinement time given by Eq. (3.25), E_{Le} is the electron escape energy from Eq. (3.27), and E_{LiD} and E_{LiT} are the ion escape energy from Eq. (3.28). Taking the corresponding ratio of P_D to P_T using Eqs. (3.45) – (3.48) and equating the two resulting expressions, an implicit relationship can be obtained that relates F and the mirror ratios at both ends of the GDM:

$$\frac{\tau_T}{\tau_D}\frac{E_{LiD} + E_{Le}}{E_{LiT} + E_{Le}} = \frac{F}{1-F} \tag{3.49}$$

Note that the mirror ratios are implicit in the ambipolar confinement times and the ion escape energies, the calculation of which requires the fraction F to be known. Also note that although the electron escape energy does not directly depend on the mirror ratios, it is nevertheless indirectly influenced by them through the ambipolar potential, upon which the electron escape energy is directly depended. Therefore, given a set of mirror ratios, calculation starts with an initial guess of F (e.g. 0.5). Once the various quantities in Eq. (3.49) are determined, a check is done to determine if the assumed F is consistent with the chosen mirror ratios. If not, a different F is chosen, and the process is iterated.

3.2 Description of the GDM Code

The physics-based model described in the previous section provides the full set of equations governing the plasma and system parameters of the GDM. The most important results are the ambipolar potential, confinement time, and the electron and ion escape energies. The governing equations need to be solved together with mass and energy conservation equations in order to obtain a self-consistent set of values for the quantities. Because the complicated functional forms of the equations couple with the interdependency of the variables, it is impossible to analytically assess the full functional dependency and solve the equations. As a result, a computer program based on the above model has been written to solve them numerically.

The inputs to the GDM program specify the operating conditions of the GDM and other physical characteristics. They include: ratio of plasma to magnetic pressures (β), the ion mass, the plasma mirror ratios, the wall reflectivity for synchrotron radiation, the shield-magnet gap, the halo thickness, the shield thickness, the component efficiencies (injector, direct converter, and thermal converter), the plasma density, the ion temperature, the plasma radius, and the input power. The code attempts to solve for two main unknowns: the electron temperature, and the plasma length. In the process of calculating these two quantities, other plasma parameters are determined, such as the ambipolar confinement time, the ambipolar potential, the electron and ion escape energies, the core and mirror magnetic fields, the radiation power, the specific impulse, the thrust, and the system masses. Appendix A shows a sample output from the program.

Fundamentally, the code solves the electron and ion power balance equations – namely Eqs. (3.30) and (3.31) – in order to determine the combination of electron temperature and plasma length that is consistent with the set of inputs. In the code implementation, however, the ion power balance equation is not used directly; rather the total (ion + electron) power balance, Eq. (3.33), is used. However, this is equivalent to using the ion power balance equation since the program ensures the electron power balance equation is satisfied.

Thus, the program iteratively solves for the electron temperature using the electron power balance and the plasma length determined by the total power balance and the electron and ion fluxes as shown in Eq. (3.41). Since the ambipolar potential enters into the length calculation, Eq. (3.20) is solved at the same time. The algorithm therefore starts with an initial guess for the electron temperature T_e (initially taken to be the same as the ion temperature). It then uses T_e to determine the radiation power P_r and the gain factor Q, which in turn are used to find a consistent set of values for the plasma length L and the ambipolar potential in the form of x, as described in the previous section. At this point, the total power is balanced for the chosen electron temperature. The program then checks for electron power balance. If electron power is not balanced, a new value of T_e is chosen and a new iteration begins.

Chapter 4

ECR-GDM Experiments

Previous chapters have examined the GDM concept as a fusion propulsion system; however, since the GDM is simply a plasma confinement and acceleration device, it also has the potential to function as an electrodeless plasma thruster if energy can be supplied by an external power source. One such power source particularly suited for the GDM configuration is a microwave source that generates plasma via electron

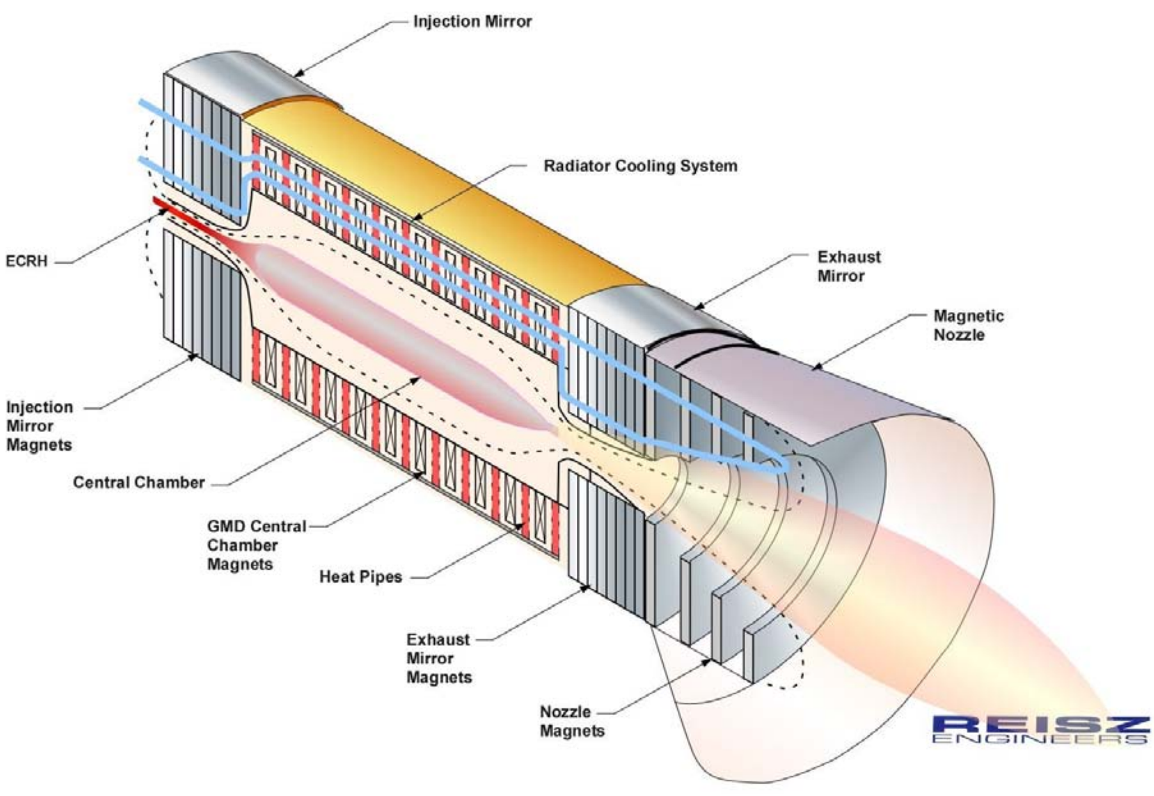

Figure 4.1. Conceptual drawing of an ECR-GDM thruster. Courtesy of Reisz Engineers.

cyclotron resonance (ECR). Figure 4.1 illustrates the proposed concept.

Microwave ECR devices are more desirable than RF-powered devices for high power applications. One reason for this improved desirability is that higher frequency can lead to a higher density plasma. Another reason is that microwave circuits are simpler than those for low-frequency RF. In this chapter, an ECR-GDM experiment will be presented. The goal is to characterize an ECR plasma, as well as studying the GDM concept.

4.1 Electron Cyclotron Resonance Theory

In this section, the plasma waves responsible for ECR and the physical mechanisms behind it will be described. First, the section begins with a discussion on waves in a magnetized plasma.

4.1.1 Wave Propagation in a Magnetized Plasma

Plasma waves can propagate at an arbitrary angle to the applied magnetic field $\vec{B}_0$. This section will focus on the principal waves; i.e. electromagnetic waves that travel parallel to and perpendicular to $\vec{B}_0$. There are four principal waves in a magnetized plasma, depending on the direction of wave propagation and the electric field polarization of the wave [43]. These are the ordinary wave (O-wave), the extraordinary wave (X-wave), the right-hand circularly polarized wave (R-wave), and the left-hand circularly polarized wave (L-wave).

As illustrated in Figure 4.2, both the ordinary and the extraordinary waves propagate perpendicular to the external magnetic field. By contrast, the two circularly

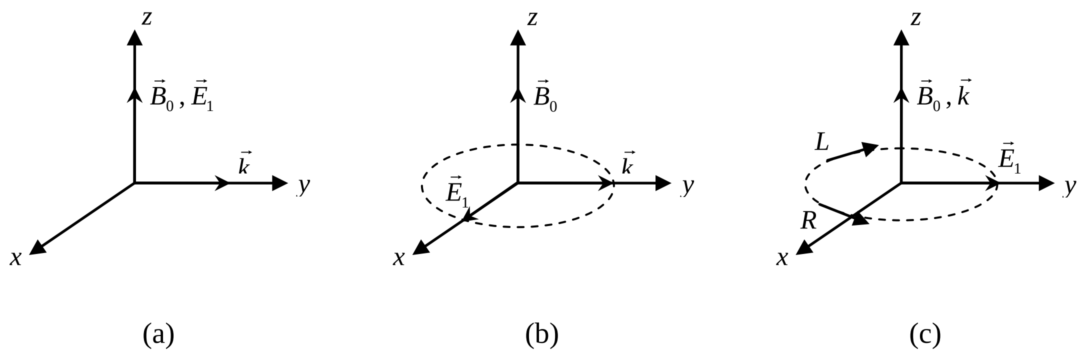

Figure 4.2. Directions of wave propagation $\vec{k}$, wave polarization $\vec{E}_1$, and applied magnetic field $\vec{B}_0$ for (a) ordinary wave, (b) extraordinary wave, and (c) right-hand (*R*) and left-hand (*L*) circularly polarized waves.

polarized waves propagate parallel to the external magnetic field. Furthermore, the ordinary wave and the circularly polarized waves are transverse waves, with $\vec{k} \perp \vec{E}_1$, whereas the extraordinary wave is partly transverse and partly longitudinal ($\vec{k}\, // \,\vec{E}_1$). The O-wave is linearly polarized with its electric field lying along $\vec{B}_0$; thus, its motion is unaffected by $\vec{B}_0$ and is the same as in an unmagnetized plasma. The X-wave is elliptically polarized such that the electric field vector traces out an ellipse in the plane perpendicular to $\vec{B}_0$. The R- and L-waves are circularly polarized such that the electric field vector traces out a circle in the plane perpendicular to $\vec{B}_0$. The polarization (i.e. electric field vector) of the R-wave rotates clockwise when viewed along the direction of $\vec{B}_0$, while the polarization of the L-wave rotates counter-clockwise.

The propagation of each wave type can be represented by its dispersion relationship. Since high frequency waves are considered here ($\omega >> \omega_{ci}$, where ω_{ci} is the ion cyclotron frequency), the ion dynamics can be ignored, and the ions are assumed to have infinite mass. This is valid for the frequency chosen for the experiments (2.45

GHz); if a much lower frequency is used, then ion dynamics must be considered. The resulting dispersion relationships for the four principal waves are given by Eqs. (4.1) – (4.4). Note that, in addition to the R- and L-waves, there is a third solution for the case of parallel propagation. This third solution is a longitudinal (i.e. electrostatic) wave ($\vec{k} \,//\, \vec{E}_1$) corresponding to plasma oscillation at the electron plasma frequency.

O-wave
$$\frac{k^2 c^2}{\omega^2} = 1 - \frac{\omega_{pe}^2}{\omega^2} \tag{4.1}$$

X-wave
$$\frac{k^2 c^2}{\omega^2} = 1 - \frac{\omega_{pe}^2}{\omega^2}\left(\frac{\omega^2 - \omega_{pe}^2}{\omega^2 - \omega_{UH}^2}\right) \tag{4.2}$$

R-wave
$$\frac{k^2 c^2}{\omega^2} = 1 - \frac{\omega_{pe}^2}{\omega(\omega - \omega_{ce})} \tag{4.3}$$

L-wave
$$\frac{k^2 c^2}{\omega^2} = 1 - \frac{\omega_{pe}^2}{\omega(\omega + \omega_{ce})} \tag{4.4}$$

In the above equations, the electron cyclotron frequency is $\omega_{ce} = \dfrac{eB_0}{m_e}$, the electron plasma frequency is $\omega_{pe} = \sqrt{\dfrac{n_0 e^2}{m_e \varepsilon_0}}$, and the upper hybrid frequency is $\omega_{UH} = \sqrt{\omega_{pe}^2 + \omega_{ce}^2}$. Note that ω_{ce} is explicitly positive. The quantity $N \equiv (kc)/\omega$ is the index of refraction of the wave. When $N \to 0$ (or equivalently when $k \to 0$), there is cutoff (or wave reflection). When $N \to \infty$ (or $k \to \infty$), resonance (or wave absorption) occurs. Table 4.1 summarizes the cutoff and resonance conditions for the principal waves.

	Cutoffs ($k = 0$)	Resonances ($k = \infty$)
O-wave	$\omega = \omega_{pe}$	None
X-wave	$\omega = \dfrac{\pm\,\omega_{ce} + \sqrt{\omega_{ce}^2 + 4\omega_{pe}^2}}{2}$	$\omega = \omega_{UH}$
R-wave	$\omega = \dfrac{\omega_{ce} + \sqrt{\omega_{ce}^2 + 4\omega_{pe}^2}}{2}$	$\omega = \omega_{ce}$
L-wave	$\omega = \dfrac{-\,\omega_{ce} + \sqrt{\omega_{ce}^2 + 4\omega_{pe}^2}}{2}$	None

Table 4.1. Summary of cutoffs and resonances for principal waves in a cold magnetized plasma; i.e. ignoring ion dynamics.

Note that the O-wave dispersion relationship, Eq. (4.1), can be written as $k^2c^2 = \omega^2 - \omega_{pe}^2$. It is apparent, therefore, that *k* is bounded for a given wave frequency. As a result, the O-wave has no resonance, and hence does not contribute to plasma heating. Furthermore, the O-wave is bounded by the critical or cutoff density; i.e. the plasma density for which ω_{pe} equals the wave frequency. Once the plasma density exceeds the cutoff density, the O-wave is reflected.

The L-wave in the high frequency limit also has no resonance, as Eq. (4.4) shows; however, if we include ion dynamics in the low-frequency regime, we would find that the L-wave has a resonance at $\omega = \omega_{ci}$. Thus, a left-hand circularly polarized wave with a frequency $\omega \sim \omega_{ci}$ can couple energy to the plasma ions and produce a significant amount of ion heating. Similarly, a right-hand circularly polarized wave provides a significant amount of electron heating via resonance at the electron cyclotron frequency.

Finally, in the high-frequency limit, the O-wave has one resonance at the upper hybrid frequency that can contribute to electron heating. If ion dynamics are included, the X- wave also has an additional resonance at a lower frequency (called the lower

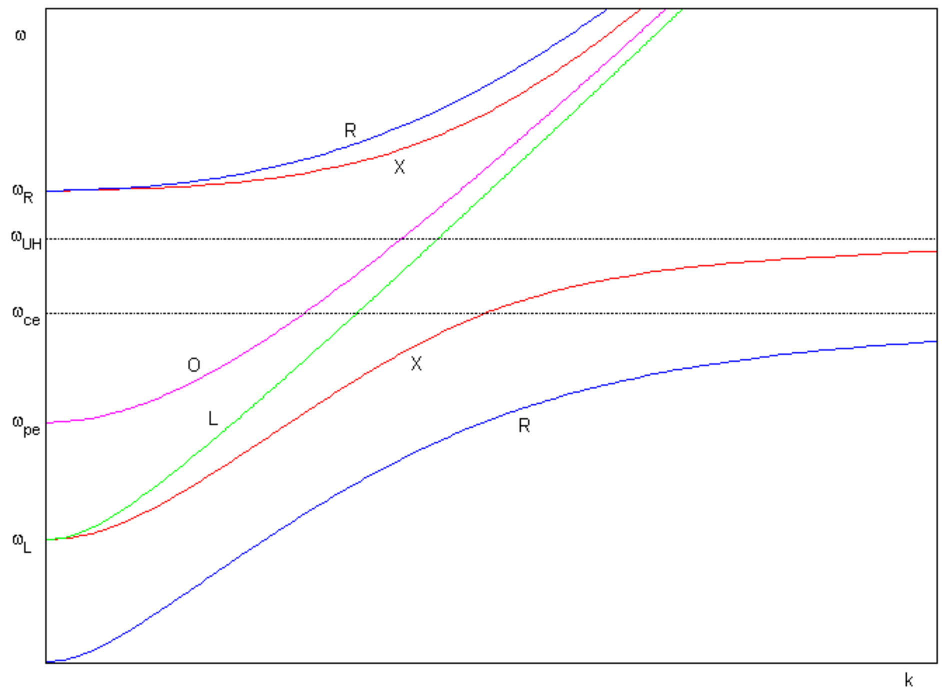

Figure 4.3. Dispersion relations for the principal waves in a magnetized plasma with immobile ions for $\omega_{ce} > \omega_{pe}$. ω_R and ω_L represent the cutoff frequencies for the R- and L-waves, respectively, as given in Table 4.1.

hybrid frequency) that can contribute to ion heating. The X-wave has two cutoff frequencies that are the same as the cutoff frequencies for the R- and L-waves. The dispersion relationships along with our observation above can be captured in a ω vs. k plot as shown in Figure 4.3. The frequencies ω_{UH} and ω_{ce} represent the upper hybrid resonance and electron cyclotron resonance for the X-wave and R-wave, respectively.

A convenient way to graphically represent wave propagation at an arbitrary angle to the applied magnetic field is the Clemmow-Mullaly-Allis (CMA) diagram [44]. The CMA diagram presents non-dimensional dispersion relations for the propagating waves,

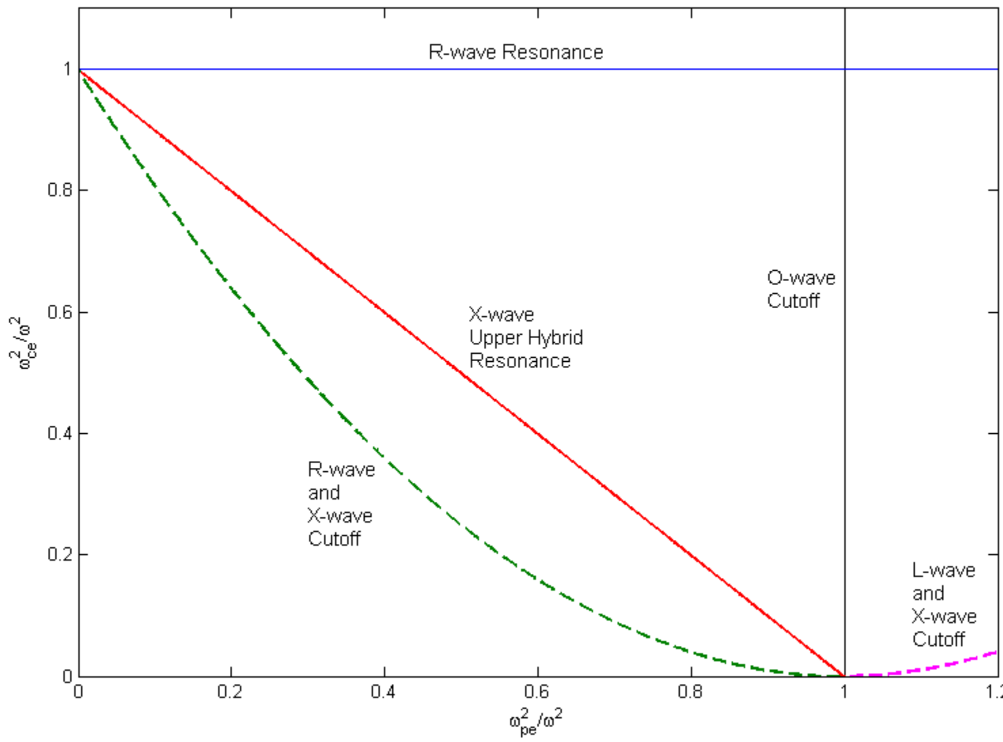

Figure 4.4. Simplified CMA diagram for principal waves in a magnetized plasma with immobile ions for $\omega > \omega_{pe}$ and $\omega > \omega_{ce}$.

as well as the cutoff and resonance conditions for the principal waves, for a wide range of magnetic fields ($\omega_{ce}\omega_{ci}/\omega^2$) and densities ($\omega_p^2/\omega^2$) (The term $\omega_p^2 = \omega_{pe}^2 + \omega_{pi}^2$ is the natural plasma frequency). Since this work only considers the high-frequency limit, the axes may be modified slightly by plotting ω_{ce}^2/ω^2 in the vertical axis and ω_{pe}^2/ω^2 in the horizontal axis. Figure 4.4 shows the cutoff and resonance conditions for the principal waves in the high-frequency region of the CMA diagram. Note that the cutoff for the L-wave and the low-frequency cutoff for the X-wave, namely ω_L, only contains a small area at the lower right-hand side of the plot. As the density increases, the high-frequency limit approximation starts to break down, and ion dynamics become important. Consequently, ion dynamics need to be included to obtain a more accurate result.

The CMA diagram can be used to follow the history of wave propagation/reflection/absorption in a plasma. Consider initial microwave propagation (before a plasma is formed) through a region of increasing magnetic field gradient, so that the wave moves toward the resonance zone. Since $B = 0$ and $n_e = 0$, the microwave starts at the origin of the CMA diagram ($\omega_{ce} = \omega_{pe} = 0$) as it travels down the waveguide system. The wave then moves upward along the ordinate of the diagram when it passes through regions of increasing magnetic field (and, thus, increasing ω_{ce}). It eventually reaches the first resonance zone for the X- and R-wave at the electron cyclotron resonance frequency. At this point, the microwave transfers its energy to the electrons through ECR and creates a plasma.

Once a plasma is formed, the microwave follows a different path on the CMA diagram. As it launches into the plasma chamber, since the density is non-zero, as it travels through regions of increasing magnetic field, it will encounter the cutoff zone for the R- and X-waves before reaching any resonance zone. Some of the microwave could still tunnel through the cutoff zone with attenuated power and reach the subsequent resonance zones. However, if the density is sufficiently high, all of the microwave energy will be reflected.

If the microwave launches into the plasma chamber from a decreasing magnetic field gradient towards the resonance zone – a configuration known as the "magnetic beach" – then the microwave would start out in regions where $\omega_{ce}^2 / \omega^2 > 1$ in the CMA diagram. As the microwave travels through regions of decreasing magnetic field, it will always encounter the ECR zone first before encountering the cutoff line. Thus, the R-wave will be absorbed without any reflection when it propagates in the direction opposite to the magnetic field strength gradient.

4.1.2 Basic Mechanism of ECR Heating

The basic principle of ECR heating is illustrated in Figure 4.5. A linearly polarized wave can be decomposed into the sum of two counterrotating circularly polarized waves. One rotates in the right-hand sense around the magnetic field at frequency ω (aptly called the right-hand circularly polarized wave, or R-wave or RHCP wave for short); the other rotates in the left-hand sense (called left-hand circularly polarized wave, or L-wave or LHCP wave for short). Since the electrons also rotate in the right-hand sense around the magnetic field at a frequency ω_{ce}, the RHCP wave can transfer energy to the electrons if $\omega = \omega_{ce}$. Figure 4.5a shows that for $\omega = \omega_{ce}$, electron rotation around the magnetic field will be in sync with the RHCP wave rotation; if the electrons are moving in the opposite direction to the electric field, then a force $F = -eE$ continuously acts on the electrons over one rotation, accelerating the electrons at all points along their circular orbit thereby increasing their energy. Of course, conservation of total energy dictates that the wave loses the same amount of energy. On the other hand, if the electrons are moving in the same direction as the electric field, the electrons will continuously lose energy to the wave over one rotation. The question then becomes whether energy gain exceeds energy loss on average. Since electrons that gain energy have a higher velocity and thus a larger gyroradius, they travel a larger distance over one wave rotation than those electrons with a reduced gyroradius due to energy loss. Since

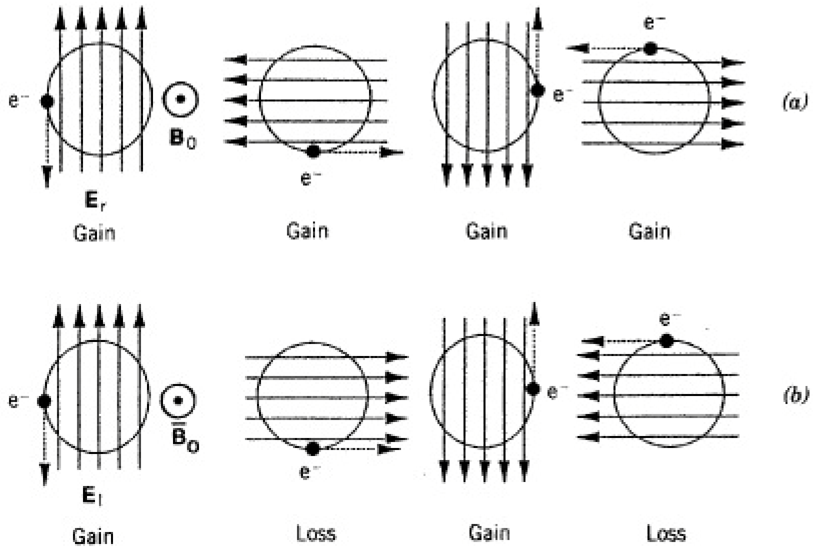

Figure 4.5. Basic mechanism of ECR heating [43]. Electrons resonate with the RHCP wave with continuous energy gain over one wave rotation in (a), whereas there is no electron resonance with the LHCP wave in (b) due to alternating energy gain and loss over one rotation.

energy change is given by the force times the distance over which the force acts, this means that on average, energy gain would exceed energy loss. This simple description explains how the RHCP wave transfers energy to the electrons via electron cyclotron resonance.

Now consider the LHCP wave in Figure 4.5b. Since it rotates in the opposite direction as the electron rotation around the magnetic field, it produces an oscillating force on the electrons over one rotation such that, on average, there is no energy gain or loss. The net effect of the LHCP wave on the electron energy is zero, hence there is no resonance between the LHCP wave and electrons. On the other hand, since the ions rotate in the same sense as the LHCP wave around the magnetic field, there is a net ion energy gain via ion cyclotron resonance. This process is similar to the mechanism described above for electrons, but applies only when a low-frequency wave is used. The high-frequency (2.45 GHz) microwave used in our experiments will not resonate with the ions unless the external magnetic field is sufficiently high such that $\omega_{ci}/2\pi = 2.45\,\mathrm{GHz}$. Since the magnetic fields attained in our experiments are far below this magnitude, ECR is our basic heating scheme whereby the RHCP wave is absorbed.

As mentioned previously, a linearly polarized wave is an equal admixture of RHCP and LHCP waves. The RHCP wave is absorbed, but what happens to the LHCP wave? It might be inefficiently converted to a RHCP wave due to multiple reflections from the waveguide feed or source surfaces, or more efficiently from a critical density layer in the source [43]. In any case, the exact fate of the LHCP wave is unclear.

4.2 Experimental Setup

4.2.1 Description of the ECR Plasma Source

As mentioned in Chapter 2, the GDM operates with a high-density plasma. A microwave source is chosen because of the high plasma density it can achieve compared to lower-frequency systems such as capacitively and inductively coupled plasma sources [43]. A helicon source can also provide similar density and electron temperature, but can be complicated to operate as both an RF electric field and a DC magnetic field need to be maintained. Furthermore, a microwave source is especially suited for the GDM since the GDM magnetic field configuration naturally provides the magnetic field (and the proper field gradient) required for ECR heating.

As described in Section 4.1, there are two ways a high-frequency wave such as microwave can couple energy to the plasma electrons. One method couples energy from a right circularly polarized wave via electron cyclotron resonance (ECR); the other method couples energy from an extraordinary wave via upper hybrid resonance. Although both energy-transfer methods require an external magnetic field, Figure 4.4

shows that the frequency at which ECR occurs is independent of the plasma density. This means that for a particular microwave frequency, the magnetic field strength required for ECR is fixed and known. This provides a well defined region in the system in which electron cyclotron resonance heating (ECRH) takes place, allowing the system designer to control the ECR zone location by design. Hence, the goal of this work is to build and utilize an ECR source for the experiments.

To accomplish this goal, it is, therefore, critical that the microwave be launched from the high *B* field side with a decreasing *B* field gradient; otherwise, density will be limited because upper hybrid absorption will occur in addition to wave reflection, as explained in Section 4.1. The *B* field configuration of the GDM upstream mirror naturally provides this "magnetic beach" configuration to ensure that ECR occurs.

Figure 4.6 shows the schematics and photograph of the ECR setup. The microwave source is a 2.45-GHz, 2-kW magnetron powered by a Model SM840E switching power generator from Alter Power Systems. The magnetron is enclosed in the water-cooled magnetron head assembly (Model TM020) with a WR284 waveguide launcher. The system can be controlled either remotely from a computer or by means of the panel controls, and the power output can be regulated from 10% to 100% of the nominal 2-kW power.

Launched microwaves are then transmitted through a series of waveguide components, all of which were purchased from Gerling Applied Engineering. The WR284 waveguide is chosen for the system. Although the established frequency range for the WR284 is 2.60-3.95 GHz, it is widely and successfully used at 2.45 GHz and is

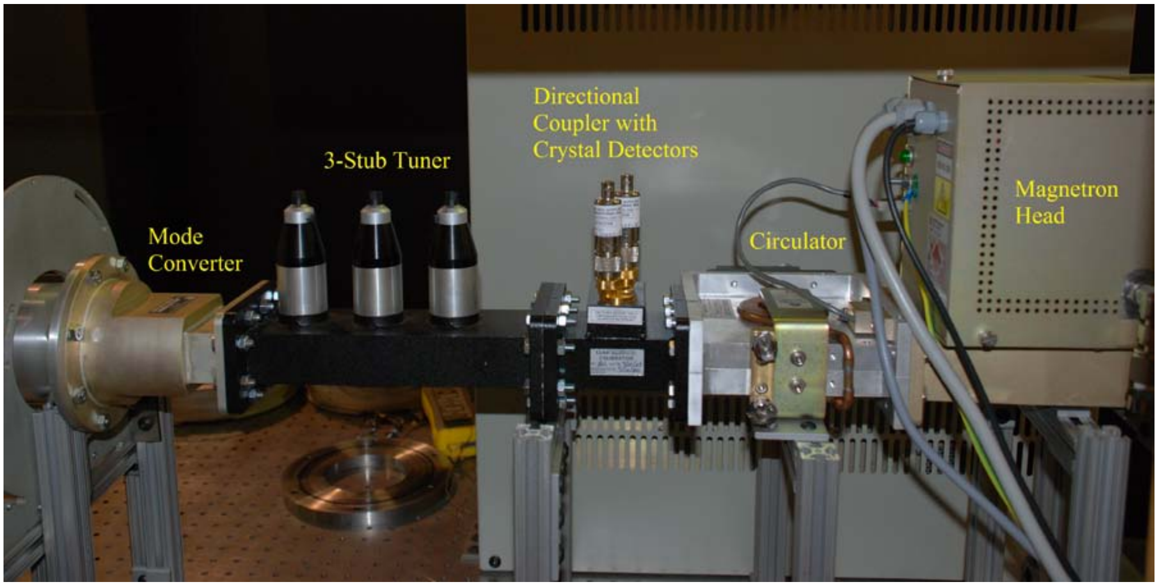

(a)

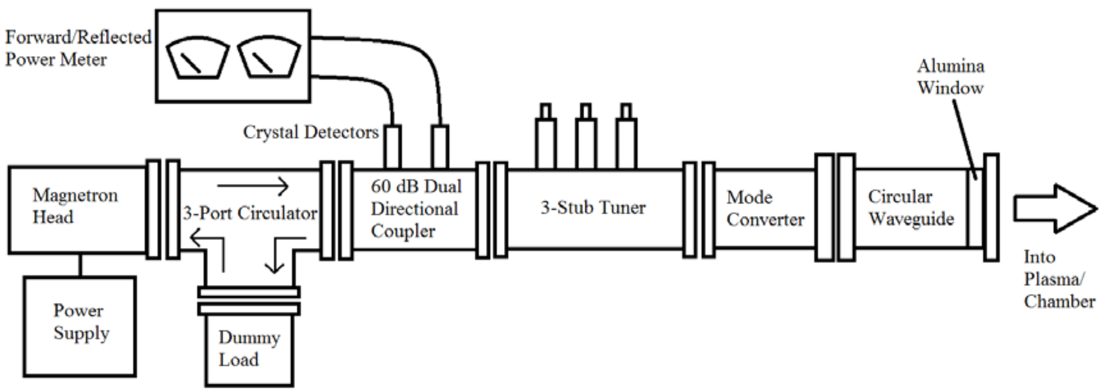

(b)

Figure 4.6. Photograph (a) and schematics (b) of the ECR source.

the preferred choice for 2.45-GHz operation at average power levels up to 6 kW [45]. It is more compact than the WR340 (which has an established frequency range of 2.20-3.30 GHz), and WR284 waveguide components are readily available from various vendors.

The microwaves are first transmitted through a 3-port circulator (Model GA1112) with a 3-kW forward and reverse continuous (CW) power capability, which diverts reflected waves from the microwave system beyond the circulator into a 3-kW (CW) water-cooled dummy load (Model GA1201) to prevent reflected power from damaging the magnetron. After the circulator, the microwaves are transmitted through a 60-dB dual directional coupler (Model GA3102) with a 6-kW (CW) rating and a minimum directivity of 25 dB. A directional coupler allows two microwave circuits to be combined into one integrated system in one direction while being completely isolated in the opposite direction [46]. A dual directional coupler is two basic couplers put back-to-back and allows both the forward and reflected power to be monitored simultaneously. The directivity indicates how accurately the system measurement can be made. High directivity indicates minimal interference between the forward and reverse powers in the coupler. The coupling factor (60 dB) indicates the amount of input power attenuation. The attenuated RF signals from the coupler are converted to DC voltages via a pair of crystal detectors and are delivered to a set of analog meters via RG-58/U coaxial cables for forward and reflected power measurements. The forward and reflected meters have a 3.5-kW and a 700-W scale, respectively, and are calibrated for low ripple waveform (e.g. CW, filtered output). The incident wave then passes through a 3-stub tuner (Model GA1001) with a 3-kW (CW) rating. Impedance matching is done via three stubs with ¼-wave chokes spaced at ¼ guide wavelength intervals; each ¼-wave choke is offset $^1/_{16}$ guide wavelength from the center. Finally, a rectangular-to-circular transition waveguide converts the dominant TE_{10} mode in the rectangular waveguide into TE_{11} mode in the circular waveguide. A ¼″ thick alumina disc at the end of the waveguide setup serves as a vacuum window as well as a microwave transmission window to transmit the microwaves into the GDM/vacuum chamber.

4.2.1.1 Mode Converter

As explained in the previous section, an ECR plasma source works by coupling the right-hand circularly polarized wave to the electron motion in a magnetic field. Standard rectangular waveguide was used, but in order to connect the waveguide system to the circular plasma tube of the GDM, a circular section of waveguide is needed. Thus, a mode converter is needed to convert from the rectangular waveguide to a circular one. The converter needs to be properly designed to ensure that it preserves mode purity and is higher-order mode free. Standard rectangular waveguides are designed to excite the linearly polarized TE_{10} mode, and the purpose of the mode converter is to convert this to the lowest-order linearly polarized TE_{11} mode in a circular waveguide. Figure 4.7 shows the two wave modes, and Figure 4.8 shows the mode converter made by Microwave Engineering Corporation. This converter uses a 2-section homogeneous stepped mode design [47] that converts from WR284 to a 3.392″ I.D. circular waveguide.

4.2.2 Design of the GDM

A small gasdynamic mirror was constructed for our study. The device consists of twelve electromagnetic coils with a spacing designed to produce the desired magnetic field topology (Figure 4.9). Together, these coils form two mirror segments and the central section. The design of the magnetic field profiles is discussed in the next section.

The twelve coils are housed in two individual magnet housings positioned back-to-back. Each housing holds six magnet coils. One housing is 14.5″ long and contains the upstream mirror and part of the central magnets. The second housing measures 15″ long and contains the remaining central magnets and the downstream mirror. The magnet

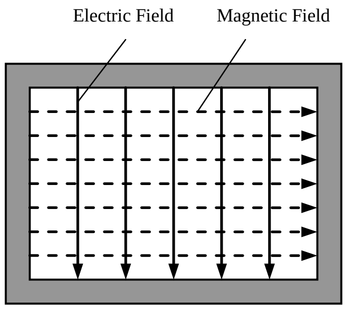

(a)

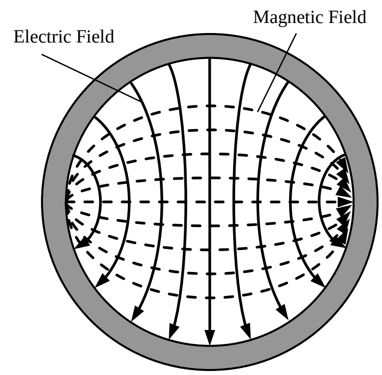

(b)

Figure 4.7. Cross-sectional view of the dominant (a) TE_{10} and (b) TE_{11} modes in rectangular and circular waveguides, respectively.

(a)

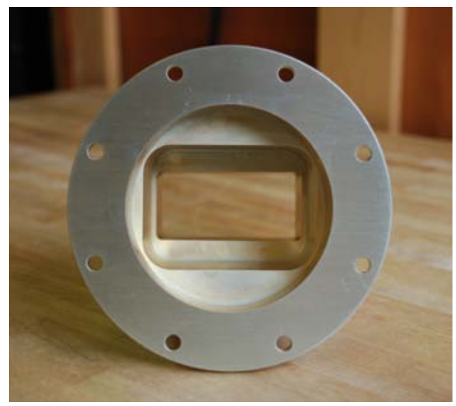

(b)

Figure 4.8. Photographs of the rectangular-to-circular waveguide mode converter using a 2-section homogeneous stepped mode design to convert from TE_{10} to TE_{11} wave mode.

spools are constructed out of aluminum, while the magnet housings and the endcaps at the two ends are constructed out of galvanized steel. Steel was chosen for these endcaps in order to enhance the magnetic field strength, while the 'endcaps' at the center are made out of aluminum so as not to disturb the magnetic field profile. The total length of the magnet assembly (and, thus, the GDM) is 29.75″. The magnets are wound with AWG 11 magnet wires, with a derated current rating of ~15 A when bundled in vacuum. Although the current rating is higher in air, overheating was a concern even with 15 A operation due to the absence of cooling and the enclosed nature of the magnet housing. Consequently, a 15 A limit sets the maximum applied current.

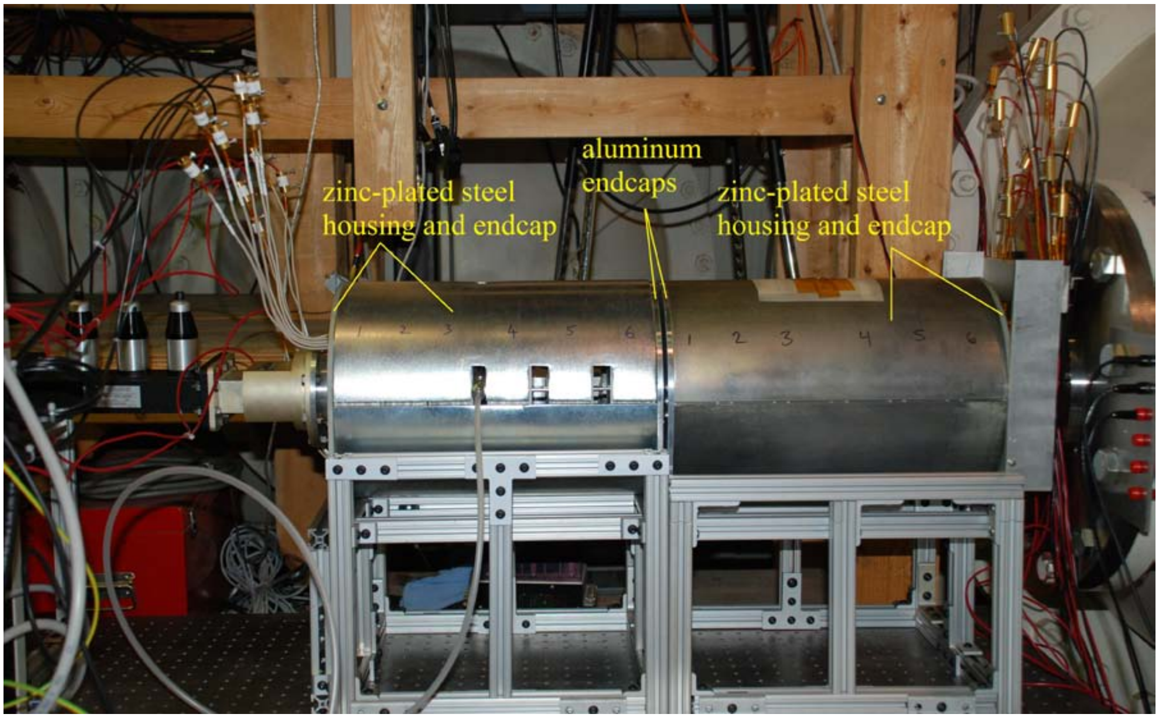

(a)

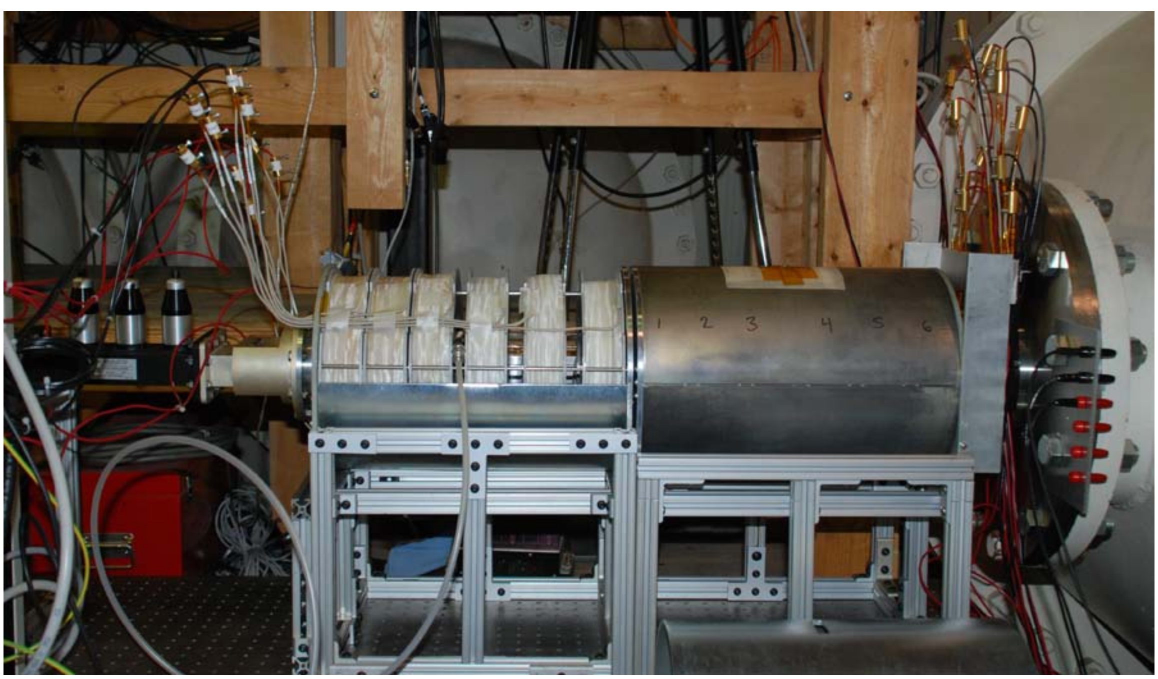

(b)

Figure 4.9. Photographs of the overall setup and the GDM magnets.

(a)

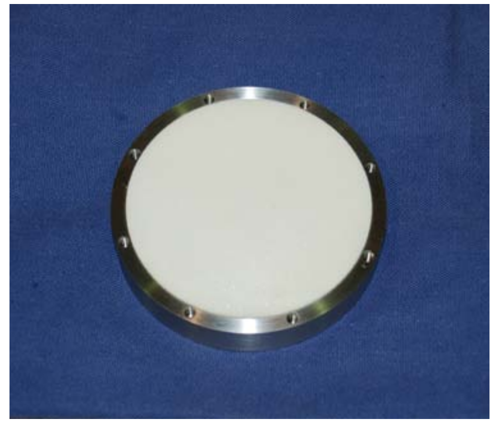

(b)

Figure 4.10. Microwave window flange made from 304 stainless steel, (a) without the window, and (b) with the ¼″ thick, 3-¾″ O.D. alumina disc positioned inside.

The plasma is contained inside an 85-mm I.D. Pyrex tube sealed at both ends to 304 stainless steel flanges. The tube with the flanges has a total length of 27″ and sits inside the magnets. One end of the tube is bolted to a vacuum chamber flange through a bellows assembly. The other end is bolted to a flange that holds the microwave window (Figure 4.10) and an aluminum waveguide extension that connects to the microwave waveguide setup described in the previous section.

The alumina microwave window is positioned around the region of maximum magnetic field in the upstream mirror. This configuration provides a decreasing magnetic field gradient in the plasma for the microwave to penetrate, as explained in Section 4.1.1. In addition, the strong magnetic field gradient induces a potential hill that helps to reduce plasma ion backstreaming and alumina disc heating as a result. Figure 4.11 shows how all the components are connected.

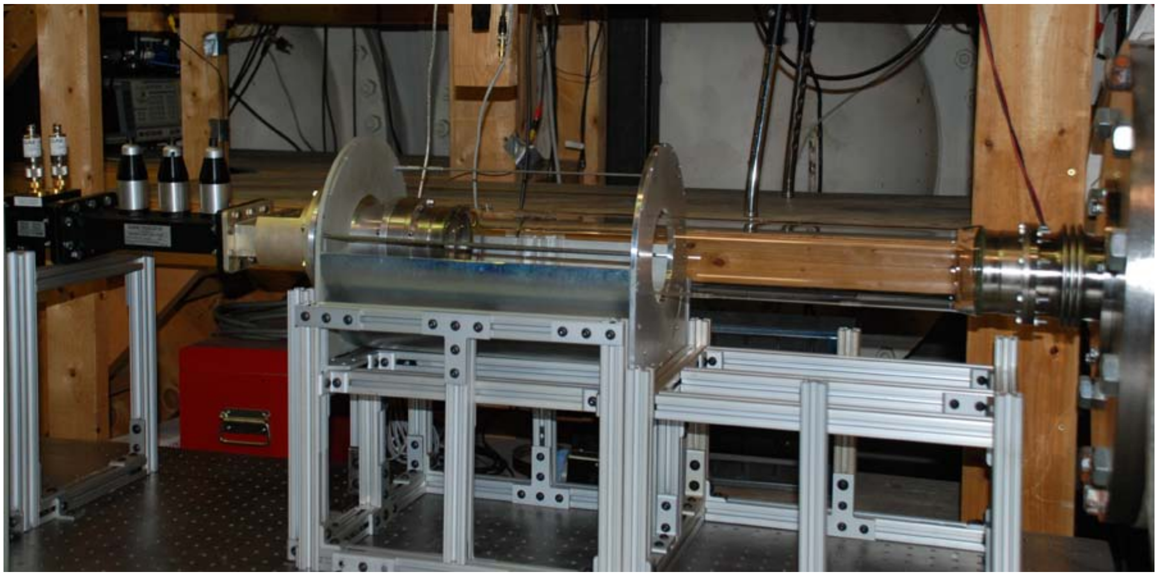

(a)

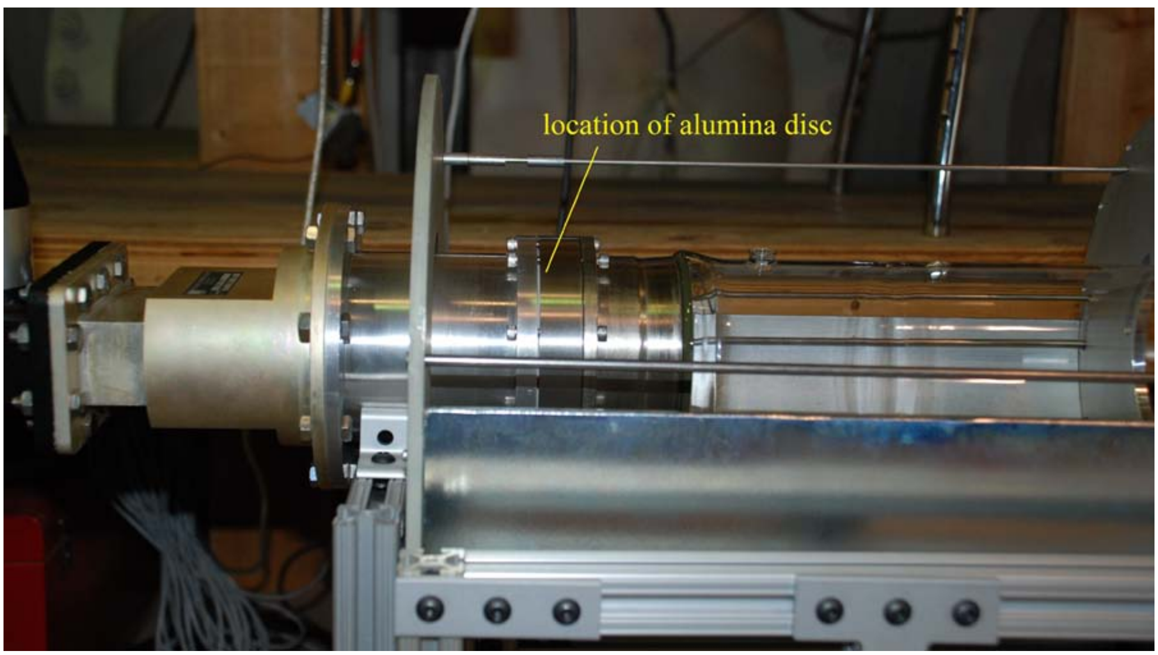

(b)

Figure 4.11. Photographs showing (a) the Pyrex tube connected to the rest of the setup, and (b) close-up of the mode converter, circular extension waveguide, and the microwave window flange. The position of the alumina disc is indicated in (b).

4.2.3 Magnetic Field Description

The design of the GDM magnetic field was driven by several desired characteristics and practical considerations. As described previously, the GDM has a mirror field with high magnetic fields at the upstream and downstream mirrors and a lower but relatively uniform central field. An additional requirement for our tests is that the downstream mirror field must be adjustable to an extent while remaining stronger than the central field. This allows the study of the effect of varying mirror ratios on the plasma. Though the upstream mirror field was held constant during testing, it must be sufficiently high to encompass the ECR zone (875 G). The central field must be uniform and lower than the mirror fields; in fact, it is desirable to keep it low enough to effectively produce a higher downstream mirror ratio given the current limits, but high enough to keep the ions magnetized. The primary practical constraint was the maximum driving current of 15 A for the magnets, as explained previously.

Three magnetic field settings were chosen to study the effects of varying mirror ratios. The mirror ratio can be varied by either varying the central field, the mirror field, or both. The upstream mirror needed to be driven with the maximum allowable current in order to satisfy the ECR zone location requirement mentioned above. The downstream mirror field was varied and the central field was kept constant in order to isolate the effects of varying just one parameter. Changing the central field would have affected both upstream and downstream conditions, complicating comparisons between settings. Table 4.2 shows the input currents for the three chosen magnetic field settings, where R_T denotes the exit mirror ratio, and Figure 4.12 shows the simulated centerline magnetic field profiles for the three settings.

Magnet Coil	Number of Turns	Spacing to Next Coil (inch)	Input Current (A)		
			Low B $R_T = 1.83$	Medium B $R_T = 2.40$	High B $R_T = 3.56$
1	365	0	15	15	15
2	363	0	15	15	15
3	362	0.5	15	15	15
4	359	0.75	3	3	3
5	363	0.75	3	3	3
6	354	0.75	3.8	3.8	3.8
7	363	0.5	3.6	3.6	3.6
8	373	0.5	3.3	3.3	3.3
9	374	0.5	3.7	3.5	3
10	369	0.5	1.2	0.5	0.5
11	372	0.5	7.5	10	15
12	371	–	7.5	10	15

Table 4.2. Input currents for the three magnetic field settings. Also shown are the number of wire turns for each of the coils and the spacing between coils.

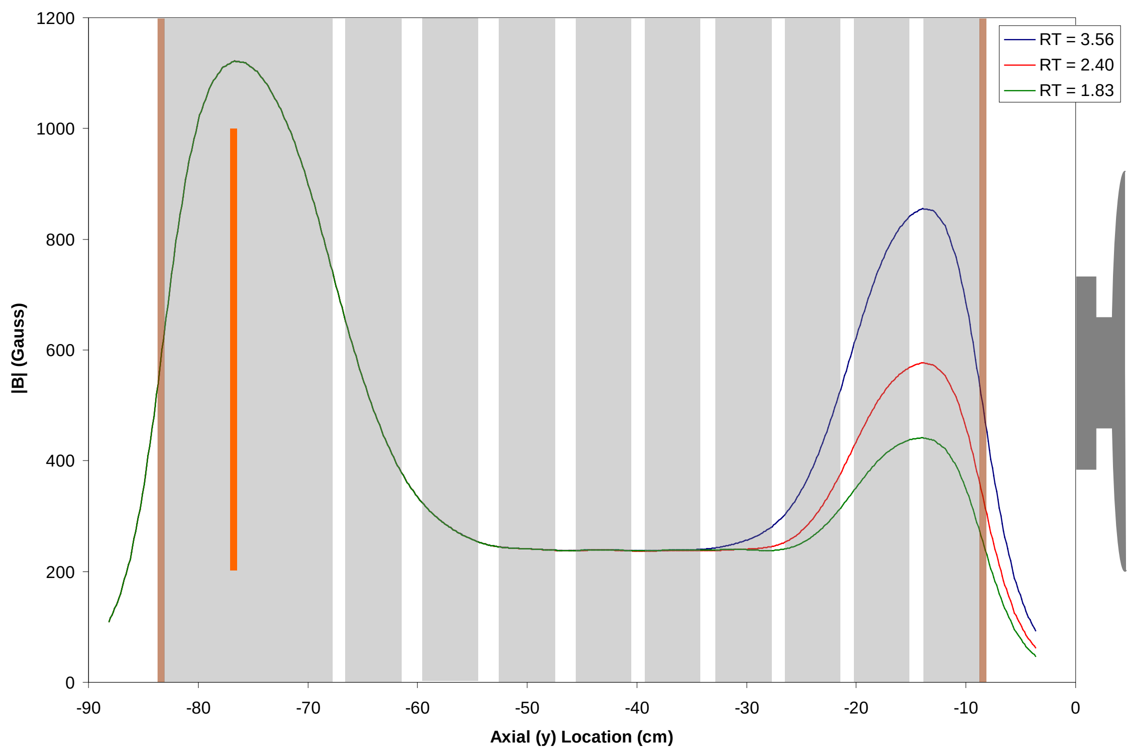

Figure 4.12. Simulated centerline magnetic field profiles for the three downstream mirror settings. y = 0 is the exit plane of the vacuum chamber flange. Light brown areas represent the steel magnet housing endcaps; silver areas represent the magnet coils; orange area represents the position of the alumina disc. Simulations carried out in MagNet 6.0.

The peak centerline field strength at the upstream mirror is ~1100 G, achieved by running the maximum current capacity of 15 A through the first three coils. The steel endcap closes the magnetic field lines, further enhancing the upstream field strength and ensuring that the ECR zone is located well beyond the downstream (vacuum) side of the microwave window. The alumina microwave window is positioned approximately where the axial magnetic field peaks. Adjustments to the central coil currents provide a uniform central field. The downstream mirror field is varied by adjusting the input currents to coils 9 through 12; this adjustment can be made without affecting the field at either the upstream mirror or the central section. Figure 4.13 shows magnetic field streamlines and the contour plots of the field strength predicted by MagNet simulations of the three magnetic field settings.

In order to verify the MagNet simulation on which the design was based, the centerline magnetic field of the GDM was mapped with a 3-axis Hall probe connected to a 3-channel gaussmeter. Figure 4.14 compares the Hall probe data with the simulation. Overall, the agreement is excellent.

4.2.4 Junior Test Facility

All testing was performed in the Junior Test Facility ("Junior") at the Plasmadynamics and Electric Propulsion Laboratory (PEPL) at the University of Michigan. The chamber, shown in Figure 4.15, is 3 m long and 1 m in diameter. A 60-cm-diameter gate valve connects this facility to the Large Vacuum Test Facility (LVTF). The pumping system consists of a E1M275 mechanical pump with a pumping speed of 180 cfm at 60 Hz, a EH500 blower with a pumping speed of 355 cfm at 60 Hz, and a

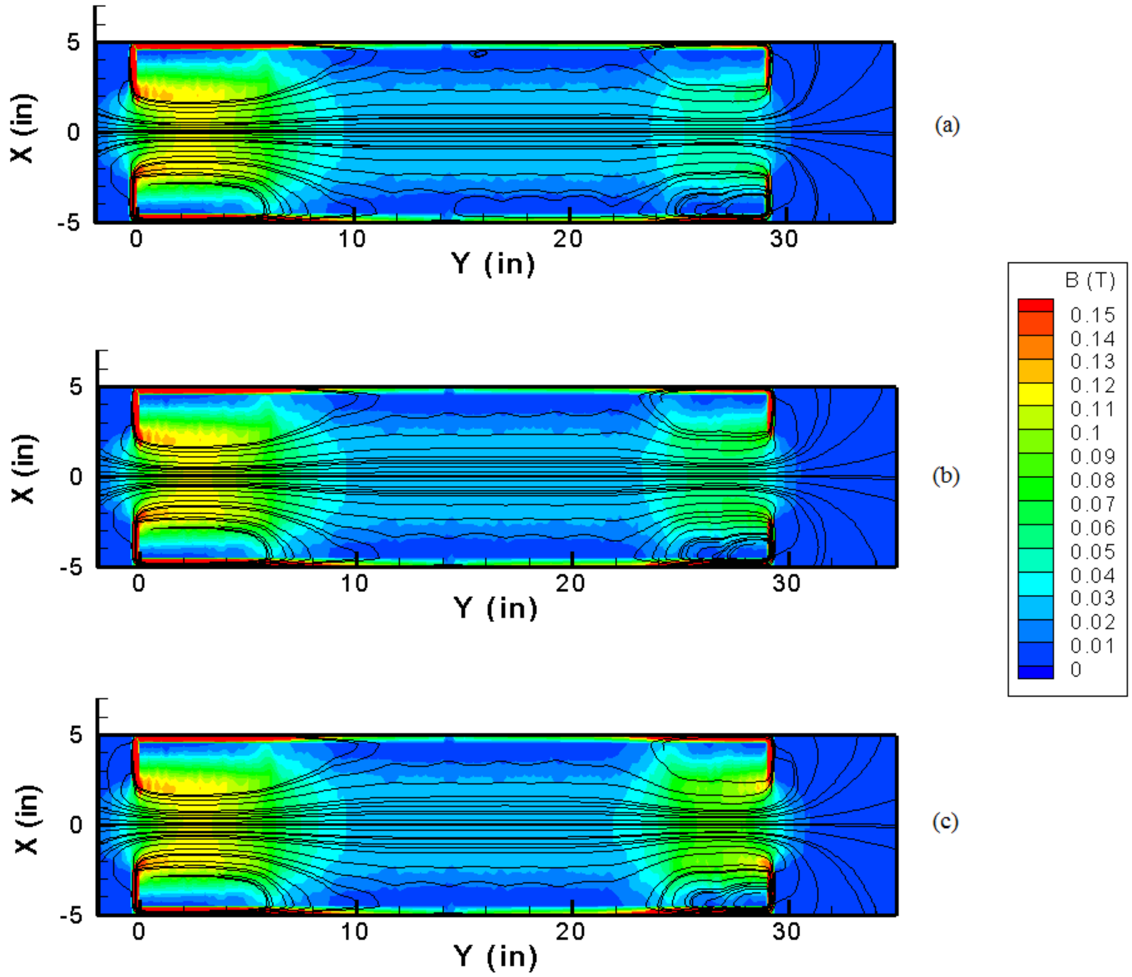

Figure 4.13. Contour plots of field strength along with field lines for (a) low, (b) medium, and (c) high B settings. Plots are shown across the z = 0 plane (where x = 0 and z = 0 is the radial centerline of the GDM). Note that y = 0 in these plots is the start location of the upstream mirror.

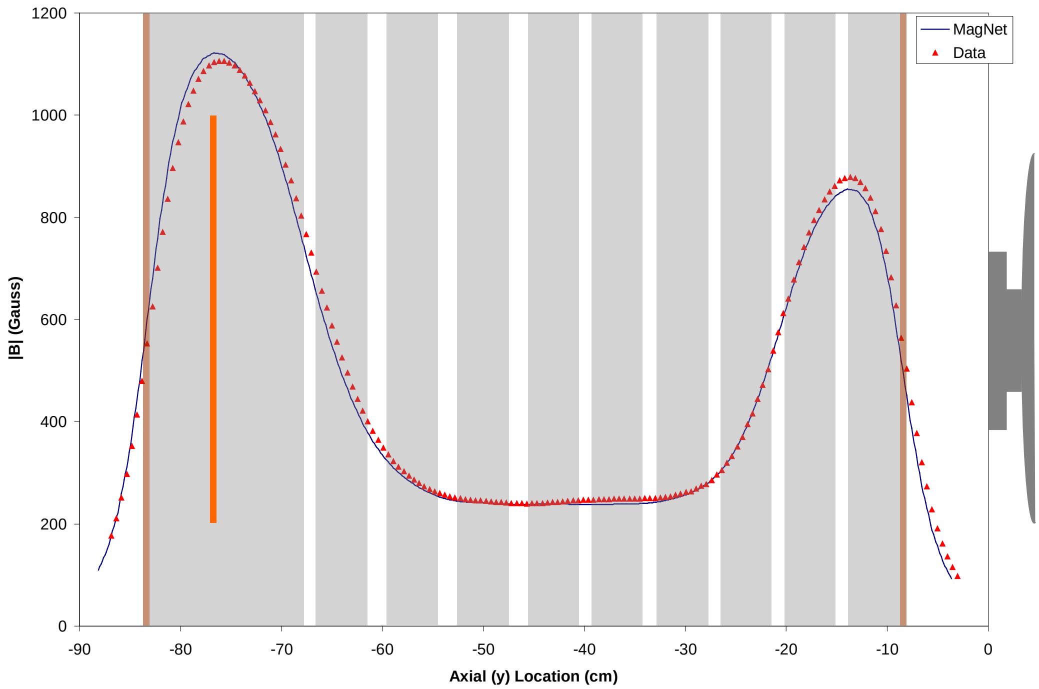

Figure 4.14. Centerline magnetic field comparison between modeled MagNet results and experimental data taken from a 3-axis Hall probe for the high field setting from Figure 4.12.

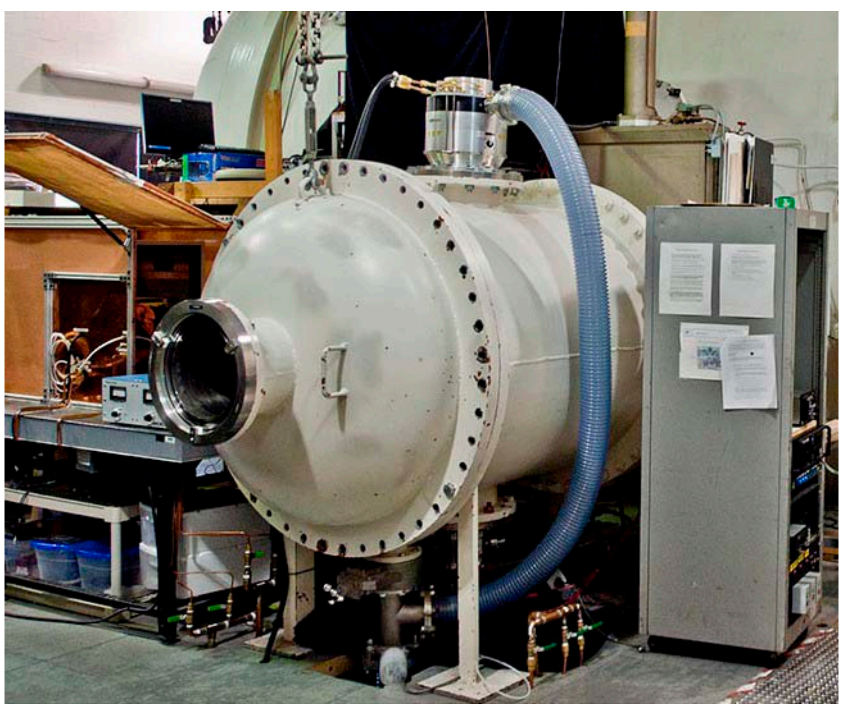

Figure 4.15. Photograph of the Junior Test Facility.

Leybold MAG W 2010 C turbopump with a pumping speed of 1650 $L \cdot s^{-1}$. The chamber can operate with the roughing pump alone, with the roughing pump backed by the blower, or with the turbopump backed by both the roughing pump and blower. The third option was used for all the testing.

At the beginning of a typical pumpdown, rough vacuum is reached using the roughing pump and the blower. When the chamber pressure reaches ~100 mTorr, the gate valve below Junior is closed and the turbopump is turned on. Closing the gate valve ensures that the roughing pump and blower are backing the turbopump correctly. The chamber can presently attain a pressure of $<10^{-5}$ Torr in about 40 minutes using all three pumping systems and can reach 10^{-6} Torr in about 1.5 to 2 hours. During testing with an argon flow rate of 250 sccm, the background pressure was around 2 mTorr.

4.2.5 Experimental Layout

Figure 4.16 shows a schematic of the experimental layout (see Figure 4.9 for photographs) and defines the coordinate system for the measurements. The Pyrex tube is bolted to a short section of bellows, which is then connected to a 13.5 cm diameter port on the 19″ diameter flange located on the side of Junior. Argon gas is fed into the system from an opening on the side of the Pyrex tube, located between magnet coils 3 and 4. Three high precision linear tables inside the vacuum chamber are controlled by an external motion controller via a LabVIEW interface. These tables allow for movement of the probes during testing. Measurements at various x and y locations were taken both inside and downstream of the GDM, providing a 2-dimensional sweep along the $z = 0$ plane. The Pyrex tube center line defines the x and z origins, while the y origin is located at the exit plane of the chamber flange. For internal (i.e., inside Pyrex tube) measurements, two of the motion tables are stacked linearly to extend the range of linear traverse. Even so, however, the furthest upstream that could be reached was y = -57 cm. Table 4.3 summarizes the data range.

4.3 Diagnostics

The main diagnostic tool used in these studies was a cylindrical Langmuir probe. Analysis of the resulting traces provided the ion number density, electron temperature, floating potential, and plasma potential.

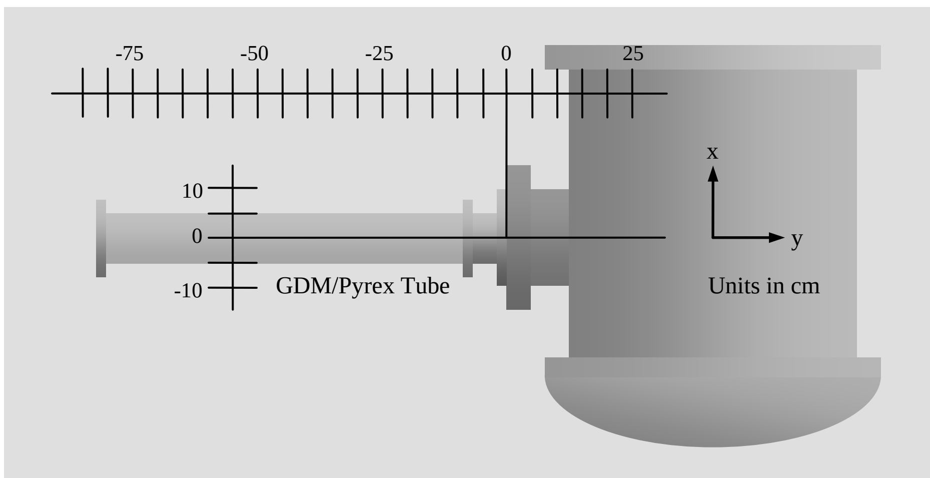

Figure 4.16. Experimental layout shown from looking down from the vertical (z) direction.

Location		Radial, x (cm)	Axial, y (cm)	Vertical, z (cm)	Mirror Ratio
Internal	Inside Magnets	-2 to 2	-57 to -8	0	Low Medium[1] High
	Downstream of Magnets		-8 to 0		
External	Inside Chamber	-3 to 3	0 to 11	0	Low Medium High

Table 4.3. Langmuir probe measurement domain.

[1]For the medium B setting, only x = 0 was measured, i.e only along centerline.

4.3.1 Single Langmuir Probe

The single Langmuir probe is the most basic plasma diagnostic tool and remains one of the most useful and ubiquitous tools used in plasma research. It was first applied by Irving Langmuir in 1926 [48,49]. The Langmuir probe, in its most basic form, is a conducting tip (e.g. a wire) inserted in the plasma. An external power supply applies a bias voltage to the probe, and an ammeter measures the current collected by the probe. This results in a current vs. voltage characteristic (I-V curve), from which various plasma properties can be deduced.

The representative Langmuir probe I-V curve shown in Figure 4.17 can be divided into three regions. Region 1 is where the applied probe voltage is below the floating potential. The floating potential, V_f, is the voltage at which the collected ion and electron currents are the same, resulting in zero net current to the probe. At probe voltages well below the floating potential, electrons are unable to overcome the large negative potential, and as a result only ions are collected. The amount of ion current collected is determined by the appropriate sheath condition. The resulting current is called the ion saturation current, and hence Region 1 is generally referred to as the ion saturation region.

As probe voltages increase, an increasing amount of electrons become capable of overcoming the potential difference and collected by the probe. At probe voltages above the floating potential (but below the plasma potential, V_p), the number of electrons that can be collected increases with increasing probe voltage; thus, collected current increases. This is Region 2. However, since the probe is still at a negative potential with respect to the surrounding plasma, electrons are not collected 'freely'; as a result, this region is called the electron retarding region.

Once probe voltage rises above the plasma potential (Region 3), the probe is now positive with respect to the surrounding plasma. Electrons become attracted to the probe, with ions increasingly being repelled. At voltages sufficiently above the plasma potential, all ions are repelled, and only electrons are collected. This current is referred to as the electron saturation current, and Region 3 is therefore called the electron saturation region.

4.3.2 Langmuir Probe Theory

Langmuir probe analysis is strongly tied to the operating regime of the probe. This regime can be characterized by two non-dimensional quantities. The first quantity,

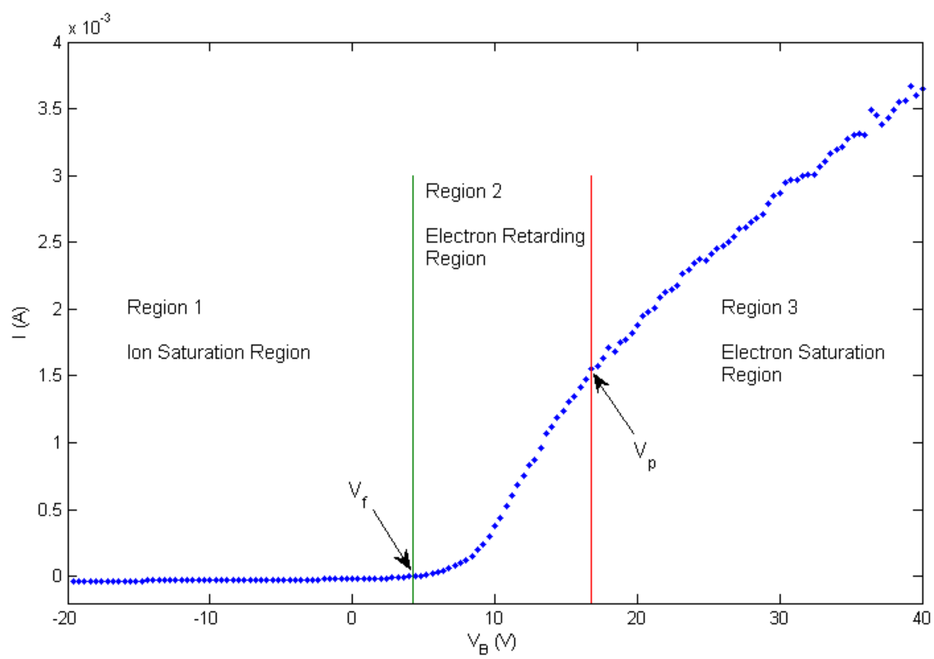

Figure 4.17. A typical Langmuir probe I-V characteristic showing how the probe current varies with probe potential.

the Knudsen number (K_n), determines whether the probe operates in the collisionless or collisional regime. The Knudsen number is the ratio of the ion and electron collisional mean free path (λ_{mfp}) and a characteristic length scale of the system, such as the Debye length (λ_D):

$$K_n = \frac{\lambda_{mfp}}{\lambda_D} \tag{4.5}$$

The particle mean free path is given by Eq. (4.6), while the Debye length, Eq. (4.7), is a measure of sheath thickness.

$$\lambda_{mfp} = \frac{1}{\sqrt{2}\sigma n} \tag{4.6}$$

$$\lambda_D = \sqrt{\frac{k_B T_e \varepsilon_0}{n_e e^2}} \tag{4.7}$$

In the above equations, σ is the collisional cross section for the relevant particle species, and n is the density. If the Knudsen number is much greater than one, then we have a collisionless sheath, and the probe is operating in the collisionless regime [50]. For the tests in these studies, the electron Debye length is very small, and the condition that $K_n >> 1$ is true. As a result, the Langmuir probe is operating in the collisionless regime.

Within the collisionless model of Langmuir probe theory, analysis can be further divided into two categories based on the ratio of probe radius to Debye length, r_p / λ_D. When $r_p / \lambda_D < 3$, the sheath is thick relative to the probe tip, and we have the so-called orbital motion limited (OML) regime [51]. In this regime, not all particles entering the sheath will ultimately hit the probe; instead, the orbital motion of particles entering the sheath is the governing factor, determining whether they will eventually be collected. Hence, current collection in the OML regime is independent of the thickness of the sheath. In fact, the sheath thickness in this regime increases as the probe voltage becomes more negative, thereby increasing the collected ion current. Laframboise developed methods to analyze the probe characteristic and deduce the ion number density in the OML regime for a collisionless and stationary plasma [52,53].

When $r_p / \lambda_D > 10$, the sheath is thin. This regime is aptly named the thin-sheath regime. Here the sheath thickness governs current collection, which can be determined without considering the orbital motion of the particles [50,51,54]. In this regime, unlike OML, it is necessary to calculate the sheath thickness to obtain the ion density.

Finally in the transitional regime (where $3 < r_p / \lambda_D < 10$), a combined approach is used, which will be discussed below.

4.3.3 Langmuir Probe Data Analysis

Every measured I-V curve was imported into Matlab for the following analysis. First, the floating potential was found directly from the I-V trace; this was the point where the collected current was zero. Then, a range of bias voltages (10 V to 40 V) below the floating potential was chosen for a linear fit to the ion saturation region. The resulting line (representing the ion current) was subsequently extrapolated to the full range of bias voltages. Subtracting this line from the original I-V curve provided an estimate of the electron current as a function of probe voltage.

With the ion current removed from the trace, the Maxwellian electron temperature could then be determined from the inverse slope of the natural log of the electron current as a function of probe bias voltage in the electron retarding region of the trace:

$$T_e(\mathrm{eV})\Big|_{inverse-slope} = \frac{dV_B}{d(\ln I_e)} = \frac{V_{B2} - V_{B1}}{\ln(I_{e2}/I_{e1})} \tag{4.8}$$

The inverse slope method is the one most typically used to determine the Maxwellian electron temperature. Another method that can be used to determine the Maxwellian electron temperature uses the plasma potential and floating potential directly in the following equation [55].

$$T_e(\mathrm{eV})\Big|_{potential} = (V_p - V_f) \Big/ \ln\left(\sqrt{\frac{m_i}{2\pi m_e}}\right) \tag{4.9}$$

Finally, for plasmas that may possess a non-Maxwellian distribution, an effective electron temperature, Eq. (4.10), can be defined [56] by partially integrating the first part of Eq. (4.8) and using the electron saturation current:

$$T_{e,eff}(\mathrm{eV}) = \frac{1}{I_{esat}} \int_{V_f}^{V_p} I_e(V_B)\,dV_B \tag{4.10}$$

For a truly Maxwellian plasma, the three methods should give equivalent electron temperatures.

Next for the ion density analysis, typically either the OML or the thin-sheath analysis was carried out depending on the operating regime of the Langmuir probe. Since this was not necessarily known beforehand in these studies due to the wide range of densities present, both techniques were carried out, and the most self-consistent values were chosen at the end.

First, the OML analysis was assumed. The ion number density for a cylindrical probe in this case is given by Eq. (4.11) [51,52,53],

$$n_{i,OML} = \frac{1}{A_p} \sqrt{\left|\frac{dI_i^2}{dV_B}\right| \frac{2\pi M_i}{1.27 e^3}} \tag{4.11}$$

where dI_i^2 / dV_B is the slope of the ion current squared with respect to bias voltage (using the ion current fit obtained in the beginning of this analysis). A_p is the probe tip surface area, and M_i is the ion mass.

Next the thin-sheath ion number density was calculated using Eq. (4.12) [50,51].

$$n_{i,TS} = \frac{|I_{isat}|}{0.61 A_s e} \sqrt{\frac{M_i}{T_e}} \tag{4.12}$$

Because the ion current fit found previously had a non-zero slope, its value varied as a function of probe voltage. In order to determine the thin-sheath ion density, a value needed to be chosen as the ion saturation current I_{isat}, preferably at a probe voltage well below the floating potential. For this analysis, the ion current value at 40 V below the floating potential was chosen as the ion saturation current. The sheath area A_s surrounding the probe tip is a function of the tip size and the sheath thickness. Since the sheath thickness is a function of the Debye length, it depends on both electron temperature and electron number density. As a result, an iterative process was needed to calculate the thin-sheath ion density. Initially, A_s was taken to be the probe tip surface area A_p. Using this initial A_s value and the electron temperature found previously, an estimated ion density $n_{i,TS}$ was calculated using Eq. (4.12). Assuming quasi-neutrality ($n_e = n_{i,TS}$), the Debye length was found using Eq. (4.7). The sheath thickness and the sheath area were then found using the following equations [50].

$$x_s = 1.02\lambda_D \left[\left(-\frac{1}{2}\ln\left(\frac{m_e}{M_i}\right) \right)^{\frac{1}{2}} - \frac{1}{\sqrt{2}} \right]^{\frac{1}{2}} \left[\left(-\frac{1}{2}\ln\left(\frac{m_e}{M_i}\right) \right)^{\frac{1}{2}} + \sqrt{2} \right] \tag{4.13}$$

$$A_s \approx A_p\left(1+\frac{x_s}{r_p}\right) \tag{4.14}$$

The thin-sheath ion density was then recalculated using the newly found value for A_s. The iterative process continued until $n_{i,TS}$ converged to a final value.

Once both the OML and thin-sheath ion density values were found, their respective Debye length and r_p/λ_D ratio were calculated. If the resulting ratios suggested that the probe was in the OML regime, the OML ion density was reported. On the other hand, if the ratios suggested the probe was in the thin-sheath regime, the thin-sheath density was reported. Otherwise, the data point fell in the transitional regime, and a weighted average based on the r_p/λ_D ratio was used to determine the correct ion density. Despite all this effort in ensuring the ion density was calculated properly, it turned out that all of the data fell in the OML regime since the probe radius was sufficiently small that the r_p/λ_D was always less than 3.

Finally, the last property that deduced from the I-V trace was the plasma potential, which is the potential of the undisturbed plasma surrounding the probe. Qualitatively, the plasma potential can be seen as the “knee” in the I-V trace between the electron retarding and electron saturation regions. To estimate the plasma potential more systematically and quantitatively, two methods were used. Both methods are illustrated in Figure 4.18.

The first method is referred to as the “log method”. The natural log of the electron current was plotted as a function of probe voltage. A line was fit to the electron retarding region; this was the same line used previously to calculate the electron

(a)

(b)

(c)

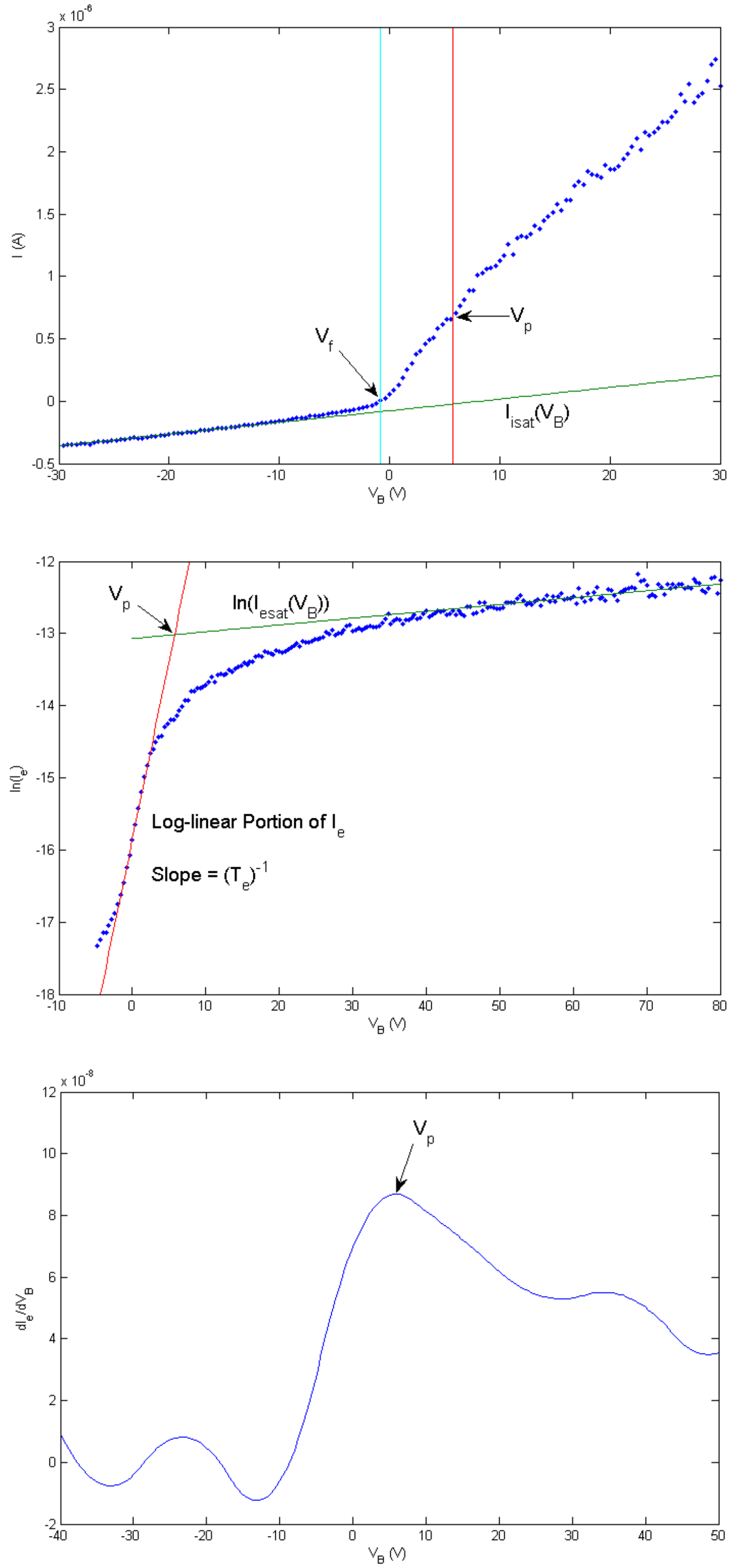

Figure 4.18. Various approaches for determining V_p: (a) 'knee' in the I-V trace, (b) log-linear method, (c) derivative method. I_{isat} and I_{esat} are the ion and electron saturation fit, respectively.

temperature. Another line was fit to the electron saturation region; this shows up in the semi-log plot as the region where the curve starts leveling off. The voltage at which the two lines intersect was taken to be the plasma potential.

The second method used to estimate the plasma potential is the "derivative method". In this method, the first derivative of the electron current as a function of probe voltage (i.e. dI_e/dV_B) was calculated. The voltage at which this first derivative is maximum is the plasma potential.

4.3.4 Langmuir Probe Setup

Figure 4.19 shows the Langmuir probe setup for the internal measurements. Two of the motion tables were stacked linearly to extend the axial range, while the last one was positioned to allow sideways (i.e. radial) motion. Figure 4.20 shows a close-up photograph and schematic of the probe tip, which is made of 0.005″ (0.127 mm) diameter by 1 mm long tungsten wire oriented perpendicular to the body of the Langmuir probe. The reason for this orientation is so that the collection electrode is oriented perpendicular to the external magnetic field, minimizing magnetic field effects.

The Langmuir probe was electrically connected to a Keithley 2410 Sourcemeter and operated via a LabVIEW VI. Using the Sourcemeter simplified the electrical connection substantially, since it can simultaneously source a voltage and measure the resulting current.

4.3.5 Magnetic Field Effects

The analysis outlined in Sections 4.3.2 and 4.3.3 assumes no magnetic field is present, so that the particle dynamics are governed by only the electric field. When a

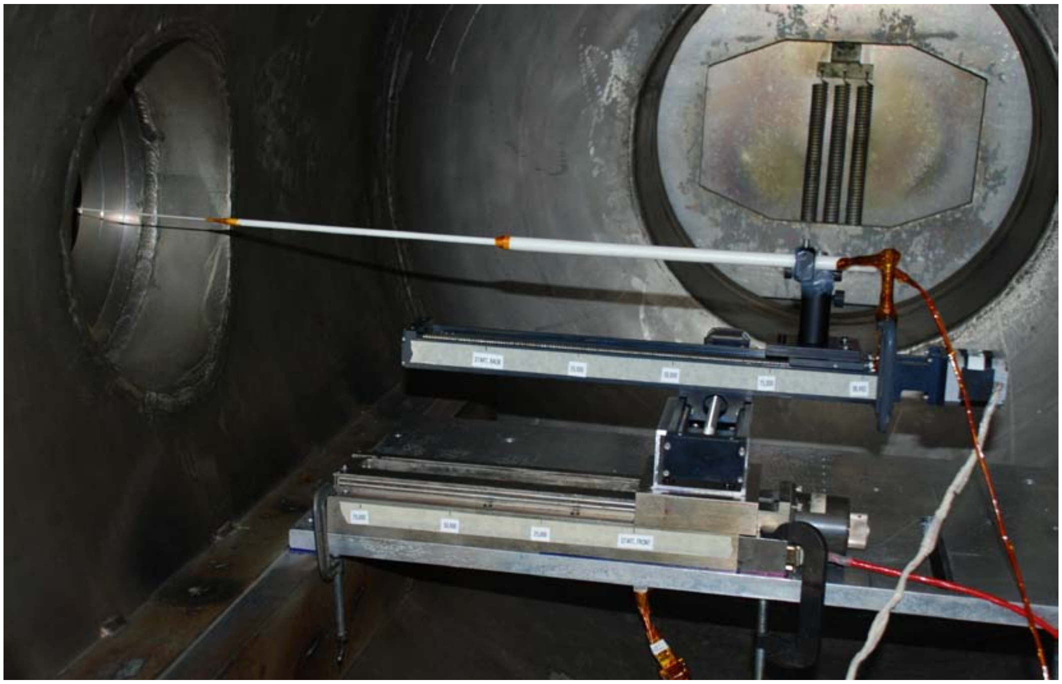

Figure 4.19. Langmuir probe setup for internal measurements.

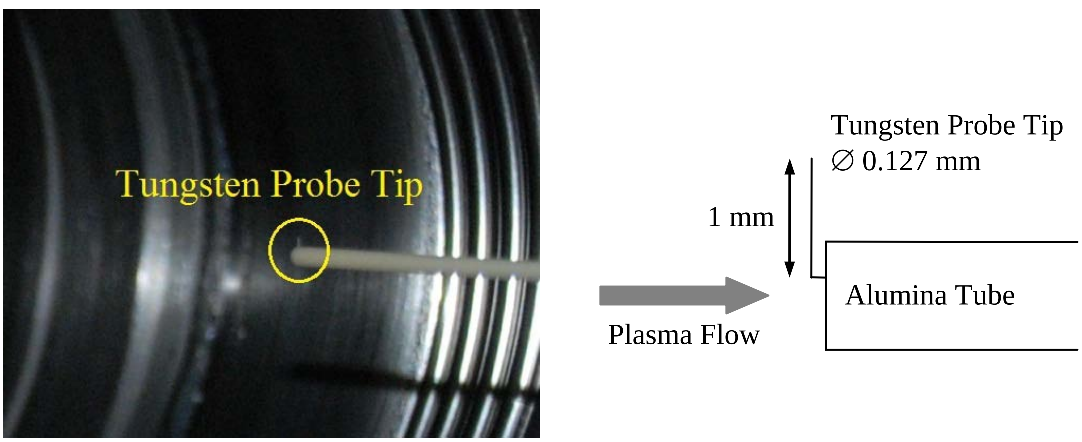

(a) (b)

Figure 4.20. Close-up photograph and schematic of the probe tip.

magnetic field is present, the problem becomes much more complicated. The magnetic field causes the plasma electrons and ions to gyrate along the magnetic field lines with a transverse radius called the cyclotron radius. This severely restricts particle motion across magnetic fields, although motion along field lines remains uninhibited.

Because particles cannot cross field lines without collisions, the sheath structure in a magnetic field can become distorted. One of the most notable effects when a magnetic field is present is that the electron saturation current is decreased below its value in the absence of the magnetic field [50,51,54]. This is presumably because the available electron current, which normally is that diffusing into a sphere of radius on the order of the Debye length around the probe, is now decreased to that diffusing at a reduced rate across *B* into a cylindrical tube defined by the lines of force intercepted by the probe [51].

The effect of a magnetic field on LP probe characteristics can be lessened by orienting the probe tip perpendicular to the magnetic field lines. Since the electron mass is so small, the effects on electron current collection often cannot be completely avoided unless *B* is very weak. On the other hand, the probe should be sized so that magnetic field effects on ion current collection are negligible.

In general, the importance of magnetic field effects is determined by the ratio of the particle cyclotron radius to a characteristic dimension of the probe, taken to be the probe radius here. If the cyclotron radius $r_c >> r_p$, then magnetic field effects can be neglected, and the techniques outlined previously for Langmuir probe analysis should apply. The cyclotron radius is given by Eq. (4.15),

$$r_c = \frac{v_\perp}{\omega_c} \tag{4.15}$$

where the perpendicular velocity $v_\perp$ is approximated by the particle thermal velocity, and ω_c is the cyclotron frequency.

$$v_\perp \approx v_{th} = \sqrt{\frac{8k_BT}{\pi m}} \tag{4.16}$$

$$\omega_c = \frac{qB}{m} \tag{4.17}$$

Table 4.4 summarizes the resulting cyclotron radii for electrons and ions at applied fields of 200 G and 1000 G, which encompass the range of field strengths expected in the test regions. Typical values for the electron and ion temperatures that can be expected were chosen in this calculation. The probe radius is $r_p = 0.064\,\text{mm}$. Near the central section where B is between 200-300 G and the electron temperature is expected to be 3-5 eV, the electron cyclotron raidus is larger than the probe radius ($r_{Le} > r_p$), and electron current collection should not be heavily affected. However, near the downstream mirror where B peaks at ~850 G for the high field setting, the electron cyclotron radius is near or lower than the probe radius ($r_{Le} \le r_p$). In this case, magnetic field effects would unavoidably come into play. By orienting the probe perpendicular to the applied magnetic field, the effect can be minimized.

		Magnetic Field (G)	
		200	1000
Electron Temperature (eV)	1	0.190 mm	0.038 mm
	5	0.425 mm	0.085 mm
Ion Temperature (eV)	0.1	16.2 mm	3.25 mm

Table 4.4. Electron and ion cyclotron radius. Probe radius is 0.064 mm. Blue indicates values larger than probe radius. Red indicates values less than or approximately equal to probe radius.

As Table 4.4 shows, the ion cyclotron radius $r_{Li} >> r_p$ for all regions, so magnetic field effects on ion current collection are negligible. Hence, the probe was sized such that the techniques outlined previously for analyzing Langmuir probe traces remain valid throughout the discharge.

Chapter 5

Experimental Results

Langmuir probe measurements were taken in order to examine the plasma characteristics inside and downstream of the GDM. Figure 5.1 shows a photograph of the argon plasma. The argon flow rate was fixed at 250 sccm, which translates to ~2 mTorr of tank pressure during operation. Input microwave power was between 700 and 800 W. The reflected microwave power was ~0 with proper tuning.

The primary goal of the measurements was to obtain the ion density, electron temperature and plasma potential throughout the measurement domain, which was summarized in Figure 4.16 and Table 4.3. The data domain was divided into two regions with respect to the GDM, which is labeled as internal and external. The internal region refers to the areas that are outside of the vacuum chamber, such as the Pyrex tube and bellows flange interior. The external region refers to the downstream areas inside the chamber.

Data were measured in a full 2D map in all cases but one. For internal measurement at the medium field setting, data were collected only along the GDM centerline. Specifically, the data domain is as follows:

Internal: $x = 0, \pm1, \pm2$ cm
$y = 0, -2, -4, \ldots, -56, -57$ cm

External: $x = 0, \pm1, \pm2, \pm3$ cm
$y = 0, 1, 2, 3, 7, 11$ cm

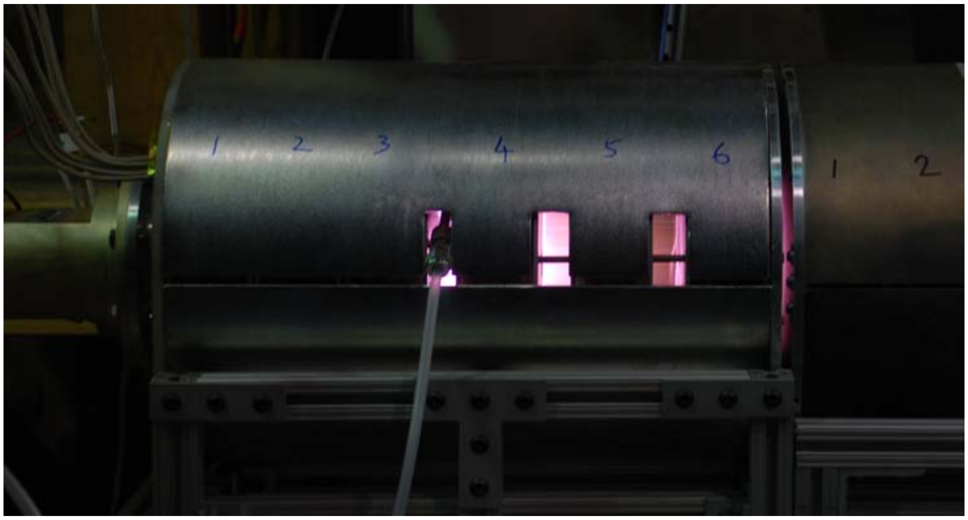

Figure 5.1. Photograph of the argon plasma inside the GDM.

5.1 Ion Number Density

5.1.1 Internal Measurements

Figure 5.2 shows the radial profile of the ion density at selected axial locations, while Figure 5.3 shows the axial profile at and off the device centerline. As expected, the density is generally highest at the center and drops off radially. The highest density observed is around 1.8×10^{17} m^{-3} for the low field setting and 1.6×10^{17} m^{-3} for the high field setting at y = -57 cm. However, the difference between these two peak densities is within the measurement uncertainty and is thus not statistically significant. Since only the exit mirror ratio was varied, it is doubtful that this variation would affect the upstream condition in any significant way. Due to the limitation mentioned previously regarding the axial distance that can be probed, the location of the highest observed density is still relatively far downstream from the main ECR zone. Therefore, this is most likely not the highest density achieved by the ECR plasma source inside the GDM, since y = -57 cm corresponds to the end of magnet 5. This location is just upstream of the central section, as can be seen in Figure 4.12. The density at this location would be expected to have dropped somewhat already compared to that produced closer to the ECR zone.

The axial density profiles further show that the density decreases rather rapidly as one moves downstream until y reaches approximately -30 to -20 cm. Between -20 and -10 cm, the density briefly increases. This ‘bump’ in the density profile coincides precisely with the location of the downstream mirror shown in Figure 4.12. This suggests

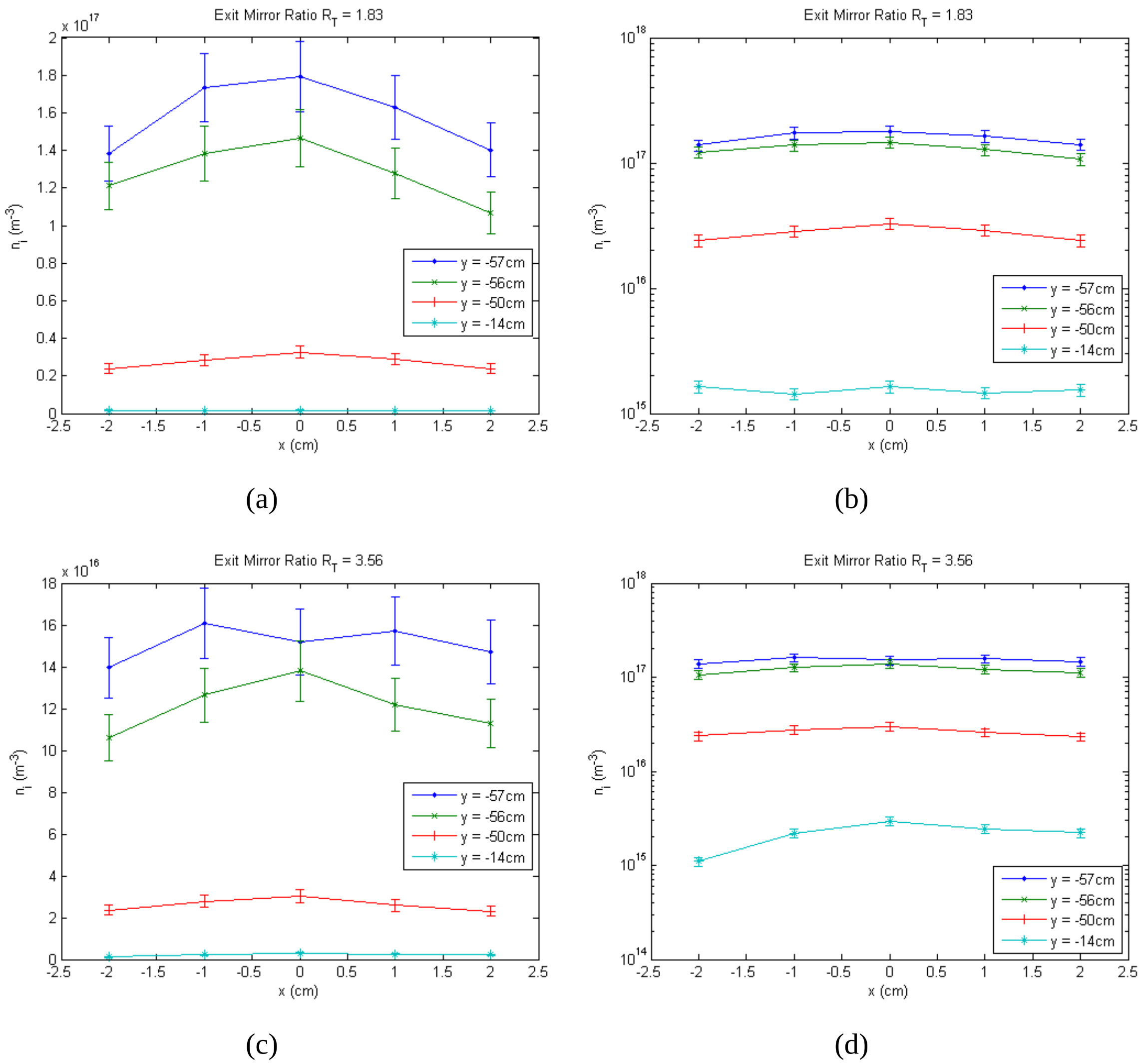

Figure 5.2. Radial ion density profiles for low (a, b) and high (c, d) field settings. The *y*-axis is plotted in both linear and log scale to better show the profiles at both upstream and downstream locations.

(a)

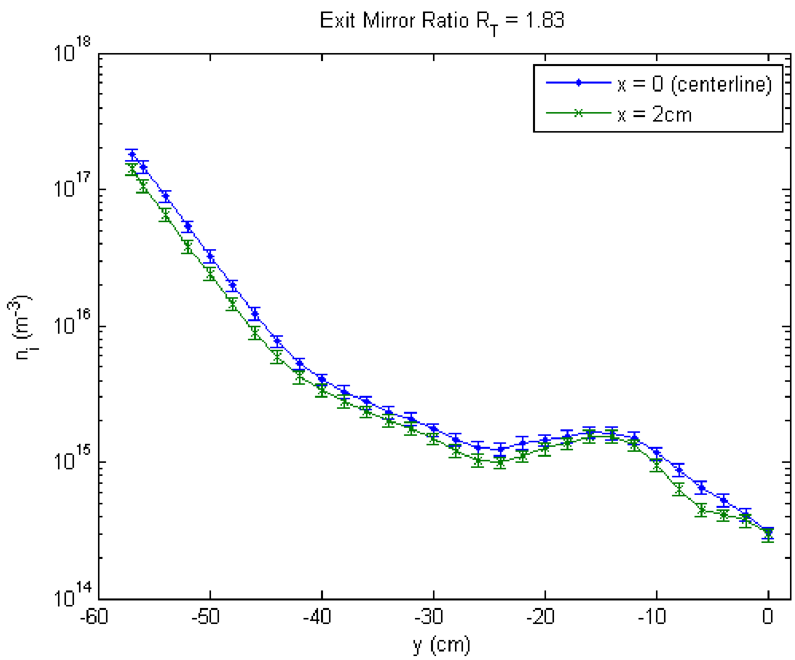

(b)

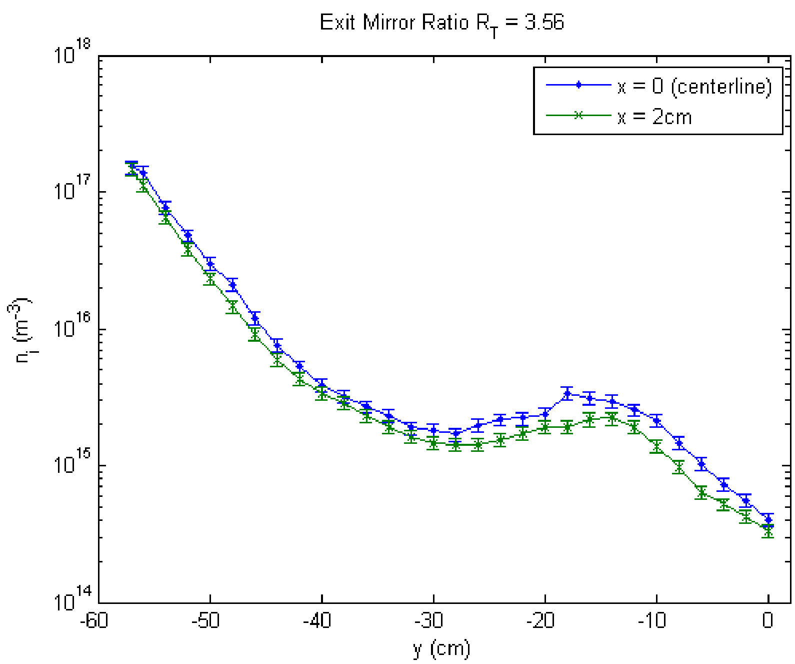

Figure 5.3. Axial ion density profiles for (a) low and (b) high *B* settings.

that some of the ions were being trapped by the stronger mirror field and can be considered as direct evidence that the ions were magnetized.

Finally, Figure 5.4 shows a 2D map of the density in the GDM. This shows that the density profile is fairly symmetric about the centerline throughout the measurement domain, and the trend is consistent across various exit mirror ratios.

5.1.1.1 Comparison between Mirror Ratios

Figure 5.5 compares the centerline density profiles for the three exit mirror ratios. As mentioned previously, the upstream density is not affected by the exit mirror ratio. However, the ion density near the downstream mirror at the high magnetic field setting ($R_T = 3.56$) is clearly higher than the ion density for either of the lower *B* settings. This is also evident in the contour plots in Figure 5.4, where the "warmer" color in (b) indicates a higher density across the radial direction for the same axial locations. This difference can be explained by the fact that the higher mirror field would trap more of the ions causing higher density not only at the mirror but also immediately upstream as the ions are being 'reflected'. Another factor that might possibly contribute to the large difference is that the maximum magnetic field strength for this mirror ratio setting (~850 G) was sufficiently close to the ECR magnetic field (875 G) that there was a secondary ECR zone present. This secondary ECR zone, however, would be much weaker due to the fact that most of the microwave energy would have been absorbed by the plasma upstream and that the microwave would be traveling against an increasing *B* field gradient at this location.

While Figure 5.5 also suggests a very slightly higher density at a medium *B* than

(a)

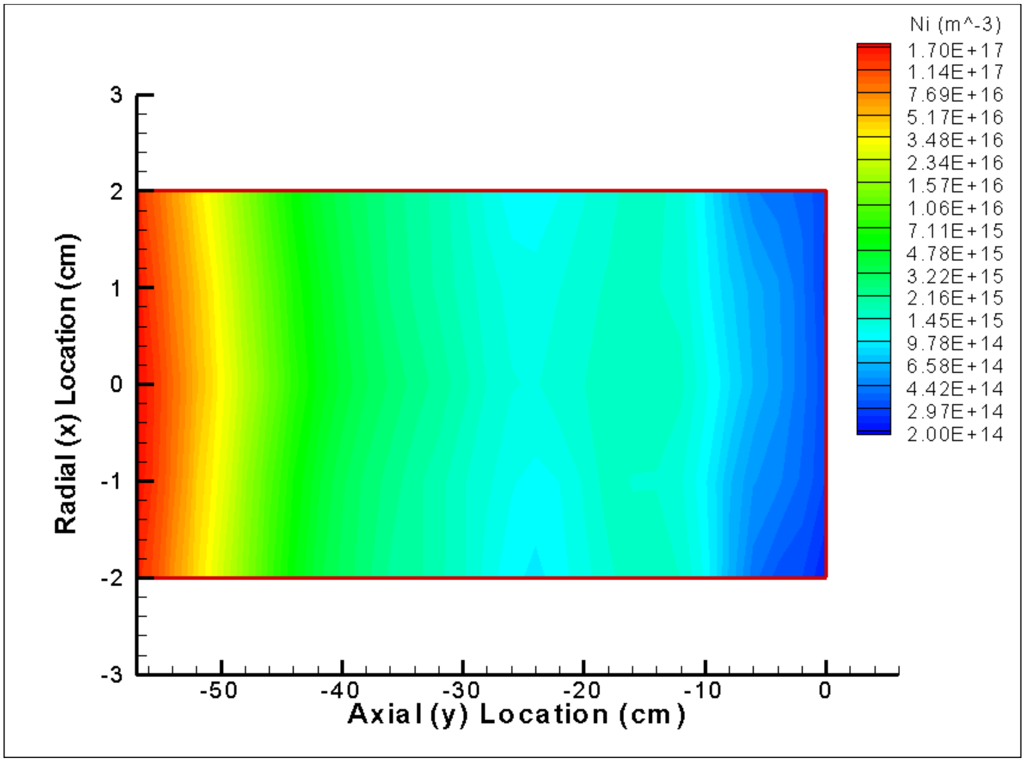

(b)

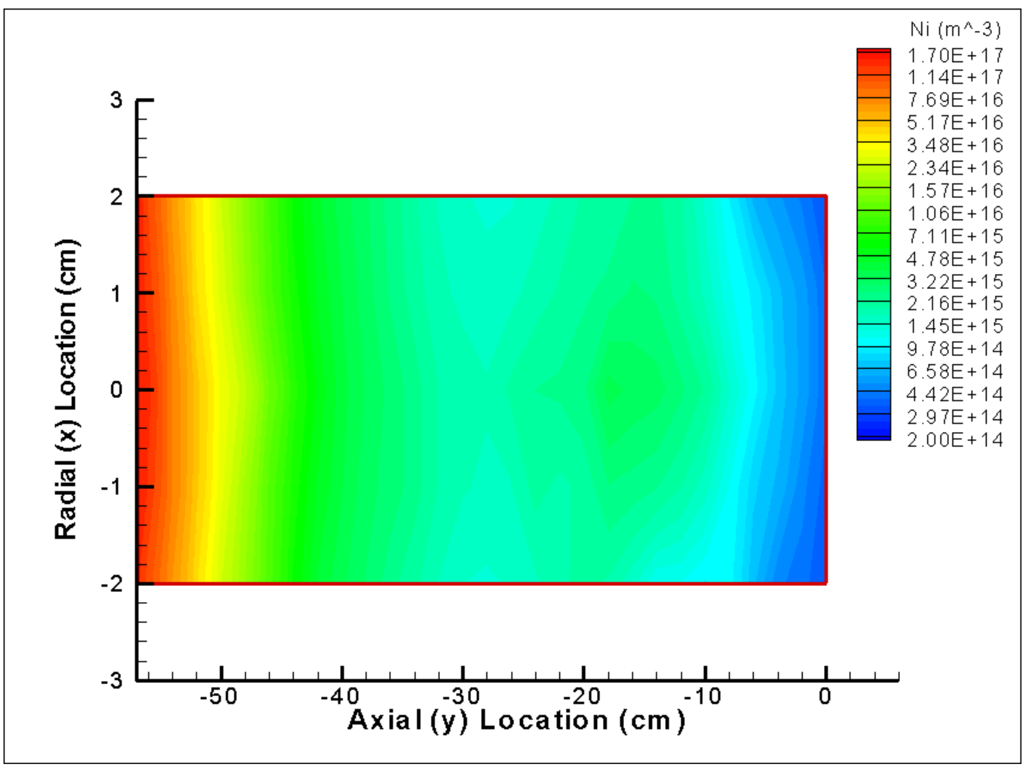

Figure 5.4. Contour plots of internal ion density for (a) low and (b) high *B* field settings.

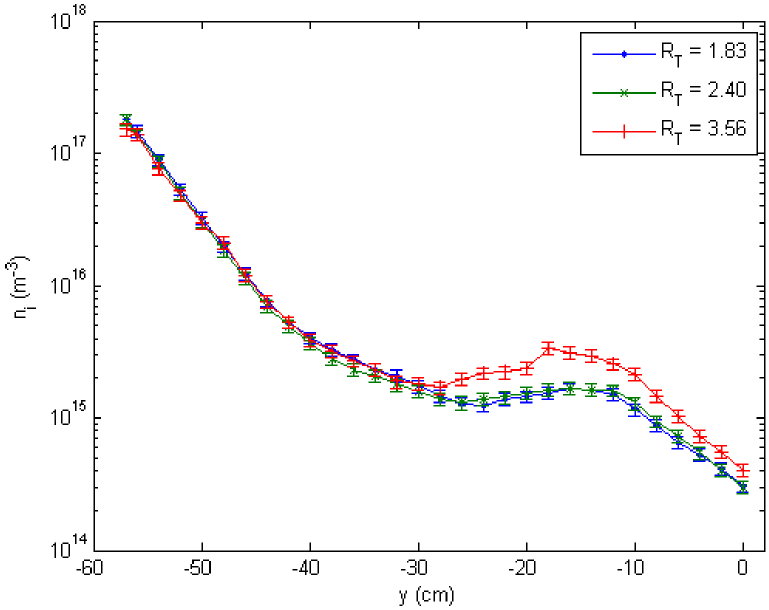

Figure 5.5. Centerline ion density for various exit mirror ratios.

at a low *B* setting, the difference is within the measurement uncertainty. Thus, the mirror ratio effects cannot be concluded for these cases.

Given an ion with sufficient energy to overcome both the low and high *B* field gradient, one effect of a higher *B* field is that it further slows down the parallel (to *B*) component of the ion velocity vector. As the ion climbs up and over the potential hill, the force acting on the particle is $\vec{F} = -\mu \nabla \vec{B}$. This could cause the local increase in the ion density shown by the higher density apparent in Figure 5.5 immediately downstream from the mirror for the higher *B* field setting. At the same time, however, the lower *B* would allow more ions to pass due to the lower energy threshold. At this point, it is not immediately clear what is the best explanation for the observed trend.

5.1.2 External Measurements

Figure 5.6 shows ion density results for the external measurement domain. Since

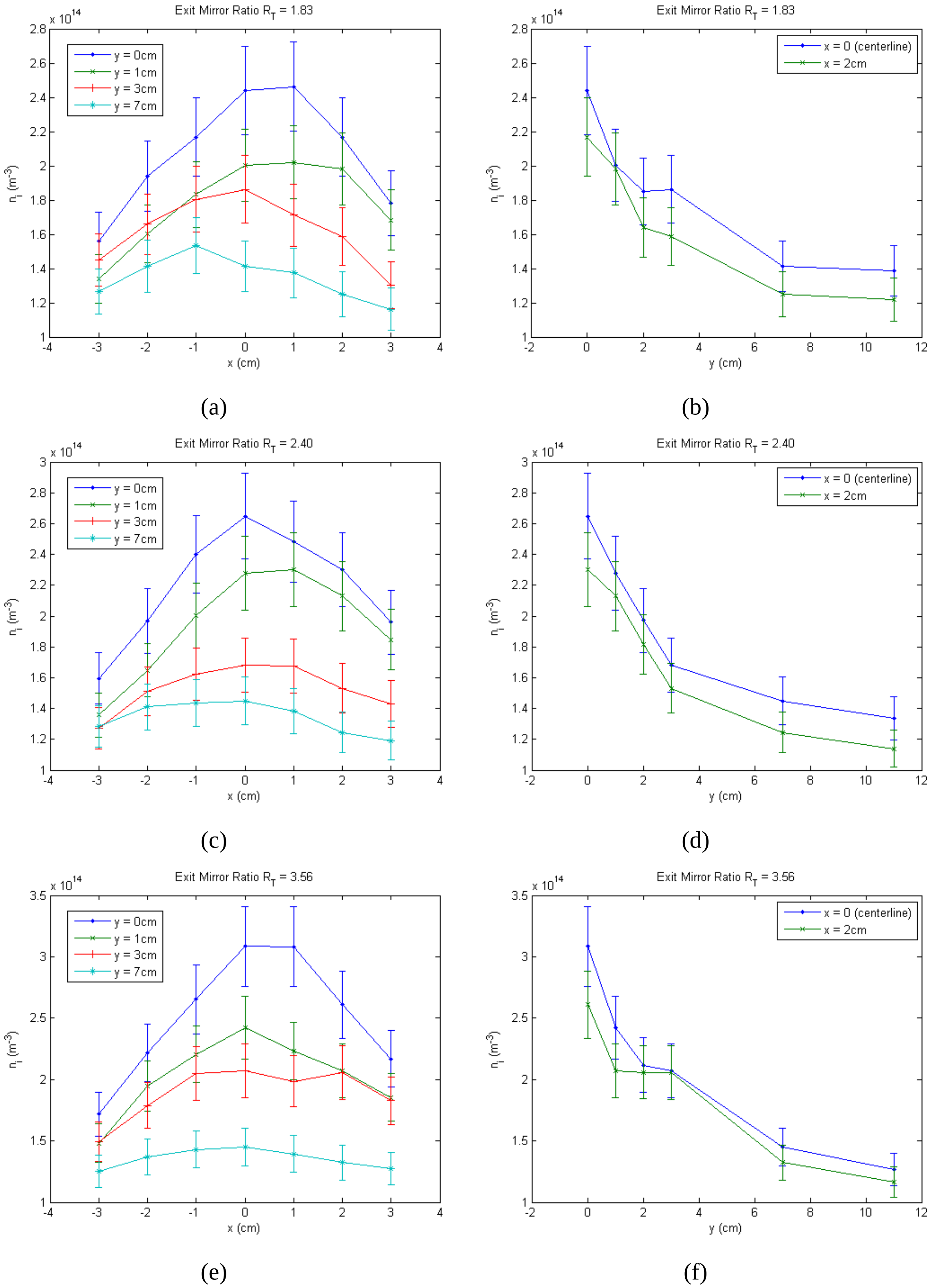

Figure 5.6. External radial and axial ion density profiles for low (a, b), medium (c, d) and high (e, f) *B* field settings. Note that the vertical scales of the plots are different for the three settings.

(a)

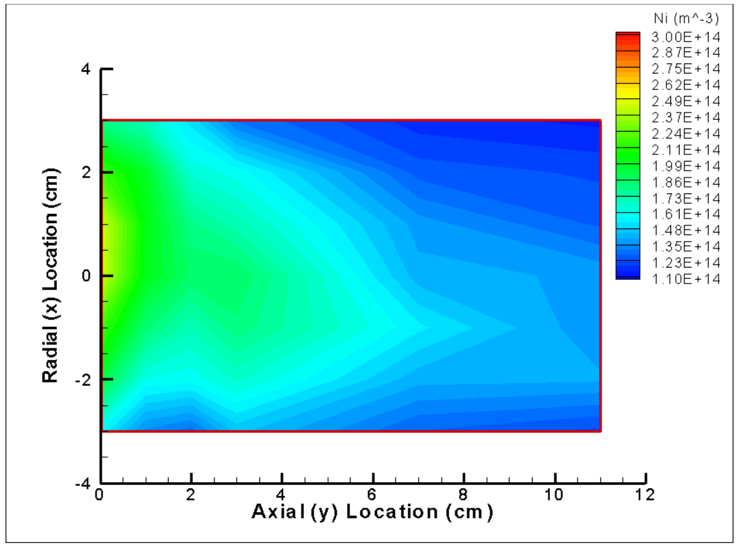

(b)

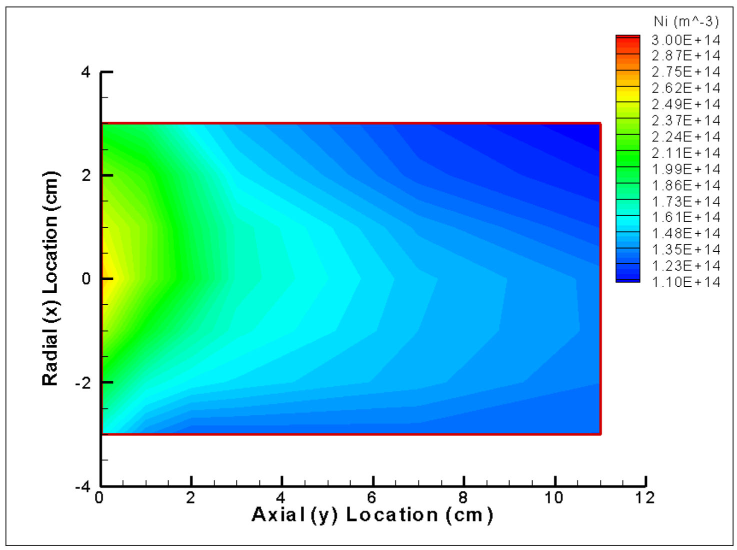

(c)

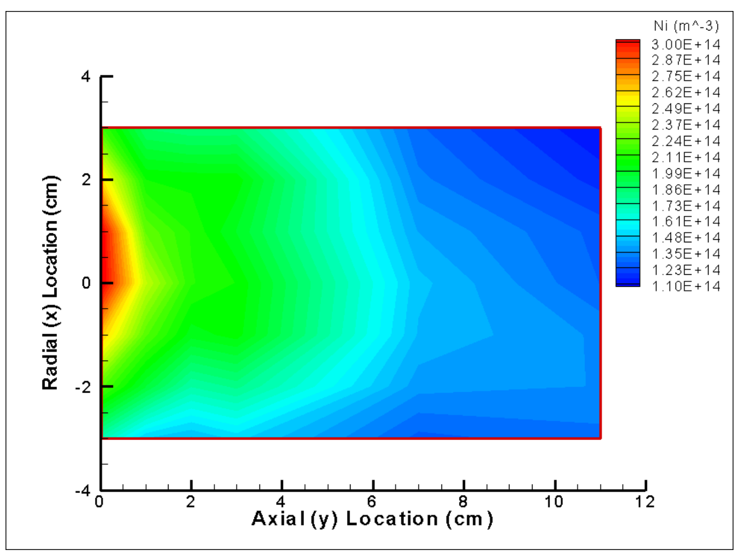

Figure 5.7. Contour plots of external ion density for (a) low, (b) medium and (c) high *B* settings.

the diagnostics setup was changed between the internal and external testing, the y = 0 results here are not quite identical to the y = 0 results from the internal measurements. However, the results from both sets of measurements do match up quite nicely within any measurement uncertainty, since the ECR plasma was very repeatable.

Once again, the ion density peaks at the centerline, dropping off both radially and axially as we move downstream. For all three mirror ratios, the ion density drops to around 1.3×10^{14} m^{-3} along the centerline at a location 11 cm into the chamber (which translates to ~19 cm downstream from the exit of the GDM magnets). The overall decrease throughout the axial range is quite modest.

The contour plots in Figure 5.7 shows that the ion density at y = 0 increases slightly with increasing R_T. This is consistent with the trend seen in Figure 5.5. This again reaffirms what was mentioned in the beginning of this section: that the results from the two sets of measurements (internal and external) were consistent with each other, and that the ECR plasma in these tests was highly repeatable.

5.2 Electron Temperature

As explained in Section 4.3.3, three approaches can be used to determine the electron temperature from Langmuir probe data. Typically the inverse-slope method is used, but the other methods can be applied to check for consistency and lend confidence to the results. There is a considerable uncertainty inherent in each approach and with the noisiness of the data. Furthermore, the electrons may not be completely Maxwellian (although in many cases this assumption is acceptable).

Figure 5.8 shows the electron temperatures determined using each of the three methods along the centerline inside the GDM for $R_T = 2.40$. The results seen here is representative of the results seen for other locations and other mirror ratios. As Figure 5.8 shows, the general trend in the axial electron temperature profile remains consistent among the various methods, which lends confidence to the observed trend. However, there are discrepancies of ≤ 2 eV in the values obtained by the inverse-slope method and by the potential method. Furthermore, the effective temperature obtained from the integral method depends on how the electron saturation current was chosen. The electron saturation current should be the current collected by the probe when it is at a sufficiently ion-repelling bias voltage; however, as Figure 4.17 shows, the electron current does continue to increase (albeit at an increasingly slower rate) as the probe bias voltage becomes increasingly positive. Thus, it is arguable what would be considered a proper

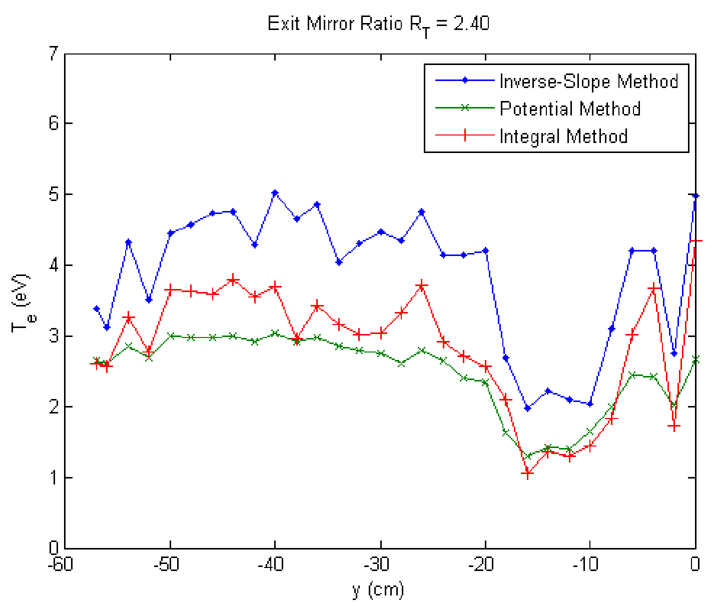

Figure 5.8. Comparison of the electron temperature calculation using Eqs. (4.8) – (4.10). For the integral method, $\ln I$ was plotted vs. V_B, and I_{esat} was chosen to be the current at the voltage $(V_{esat} + 10)$, where V_{esat} was the voltage at which the plot started leveling off in the semilog scale.

value for the electron saturation current, so long as the chosen value is sufficiently above the plasma potential.

As a result, the integral method was not used since we did not want to introduce yet another sort of arbitrariness in our analyses. Furthermore, the results from the potential method in this case were deemed to be less reliable than the inverse-slope method, since the potential method was essentially derived from two data points. By contrast, multiple data points were used to fit the electron retarding region in the inverse-slope method, providing more robustness and confidence in the result. Therefore, the inverse-slope method was chosen for the rest of the analyses. This study, however, did provide extra confidence in the trends obtained.

5.2.1 Internal Measurements

Figure 5.9 shows the axial and radial electron temperature profiles at selected *x* and *y* locations. On average, the uncertainty is around ±0.5 eV for T_e = 4 or 5 eV, which translates to about ±10 to 12% uncertainty. The radial profiles show that generally the edge appears to have an electron temperature that is as high as or higher than the temperature at the center, ignoring the error bars for the moment. Furthermore, while the profile does not exhibit a clear trend as the ion density does, a general pattern can still be deduced. The radial profiles shown here are consistent with previous GDM results [16].

The axial profiles meanwhile show that (within measurement uncertainty) the electron temperature inside the central section of the GDM remains fairly constant, around 4 to 5 eV. Recall that y = -57 cm approximately corresponds to the beginning of the central section. It is likely that further upstream (closer to the ECR zone) the electron temperature was higher. Unfortunately, it was not possible with the diagnostics setup to probe areas any further in than what was probed. More interesting, however, is that there is a clear decrease in electron temperatures between $y = -20$ to -10 cm, corresponding to the exit mirror location (see Figure 4.12). This can be seen clearly in the contour plots in Figure 5.10, which also shows the fairly uniform temperatures in the central section of the GDM. The local ‘hot spots’ were most likely a result of measurement uncertainties together with the slight spatial fluctuation that was seen in the radial profiles.

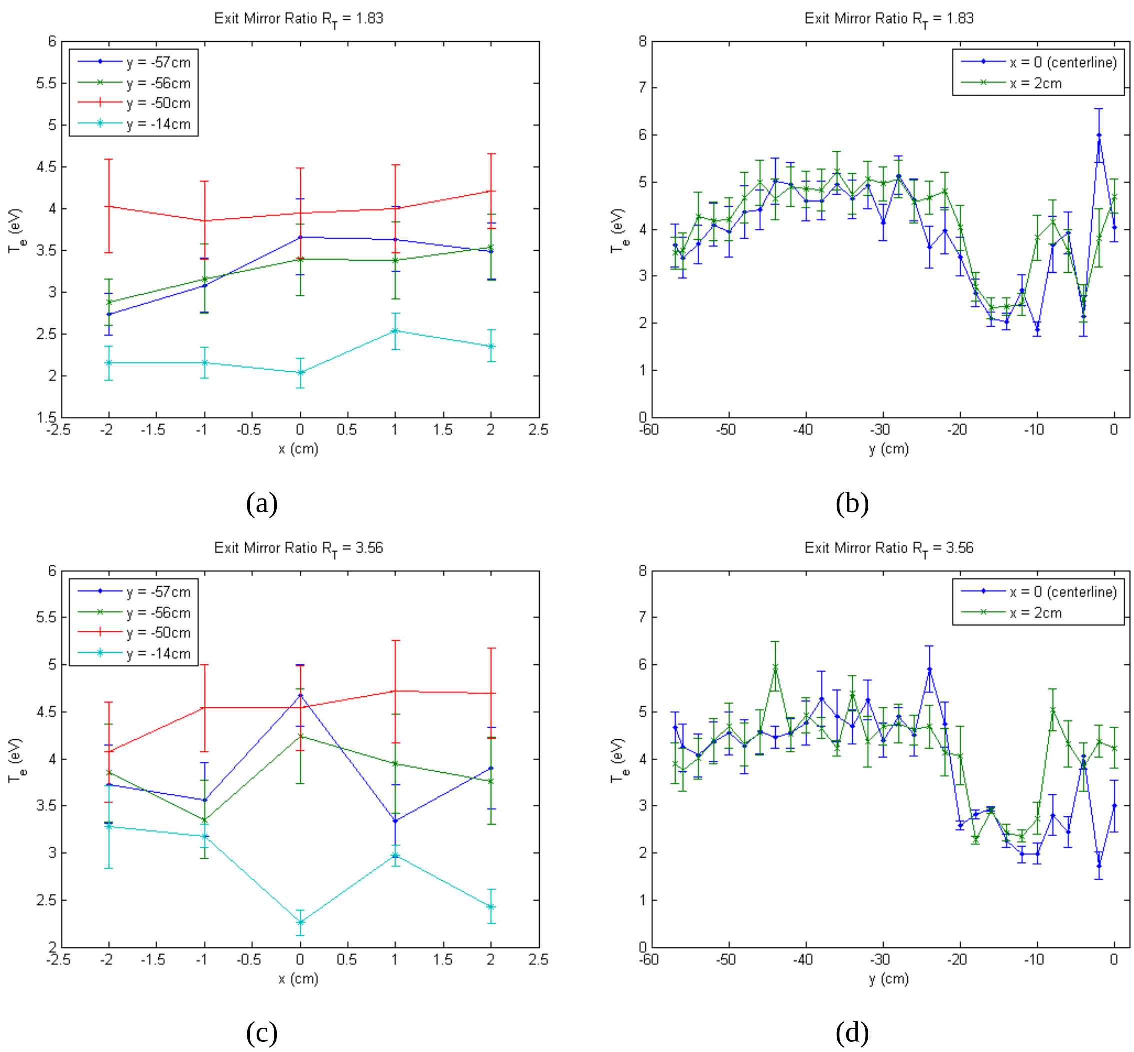

Figure 5.9. Internal radial and axial electron temperature profiles for low (a, b) and high (c, d) B field settings.

(a)

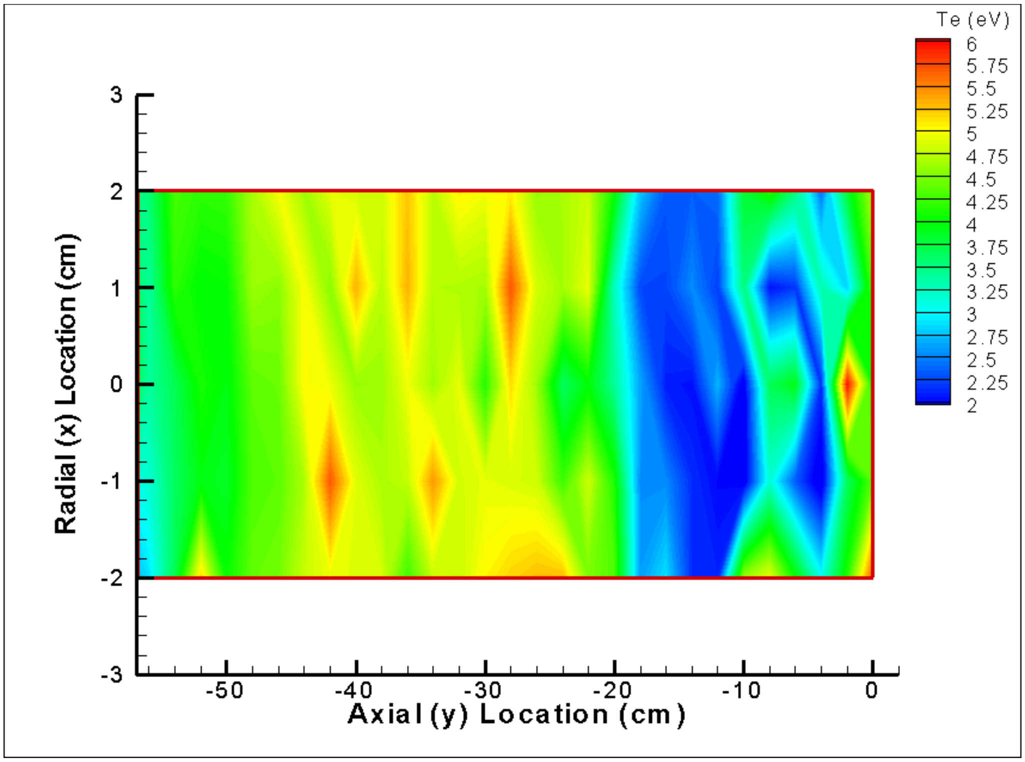

(b)

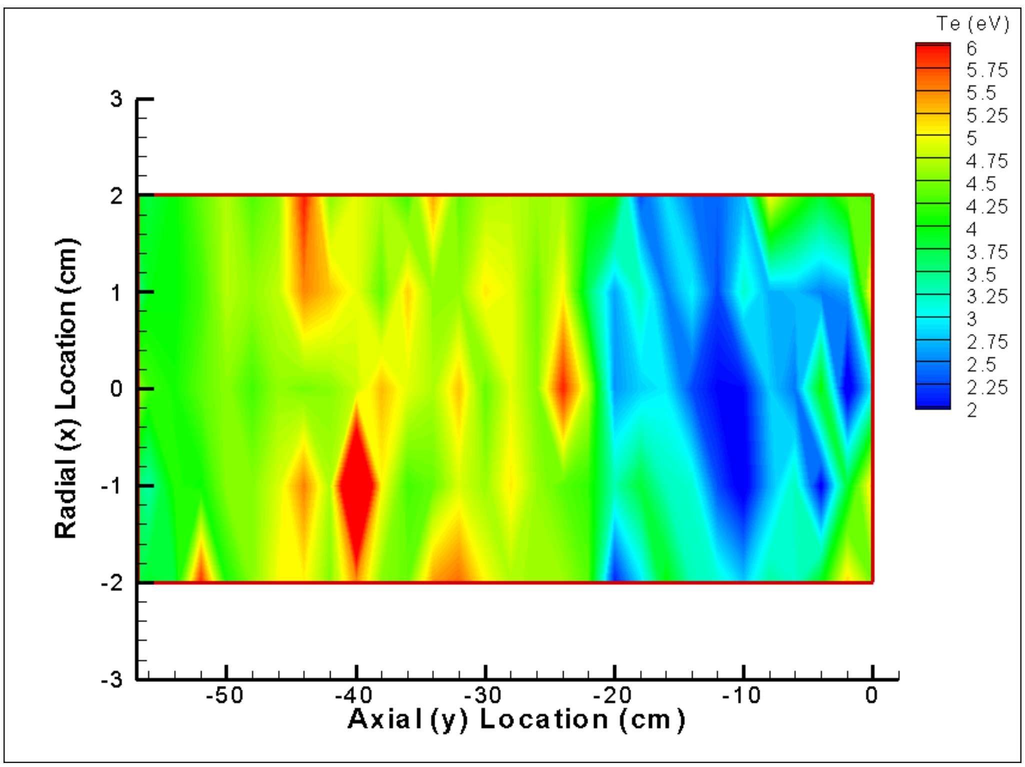

Figure 5.10. Contour plots of the electron temperature inside the GDM for (a) low and (b) high B field settings.

The electron temperature does not have a strong dependence on the exit mirror ratio, as is evident in the contour plots and in Figure 5.11, which compares the centerline profiles for the three magnetic field settings for the exit mirror. Even without error bars, the three curves generally overlap each other, except for the region immediately downstream from the GDM magnets ($y \geq -8$ cm) where variations and fluctuations become larger. This variation generally agrees with the comments made in Chapter 3 that the electron dynamics inside the GDM are not much affected by the mirror ratios due to the small mass and high energy of the electrons. Within the limits of what could be tested, this appears to be the case.

5.3 Plasma Potential

The plasma potential was determined using the combination of methods outlined previously in Section 4.3.3. First, the derivative method was used, in which the plasma

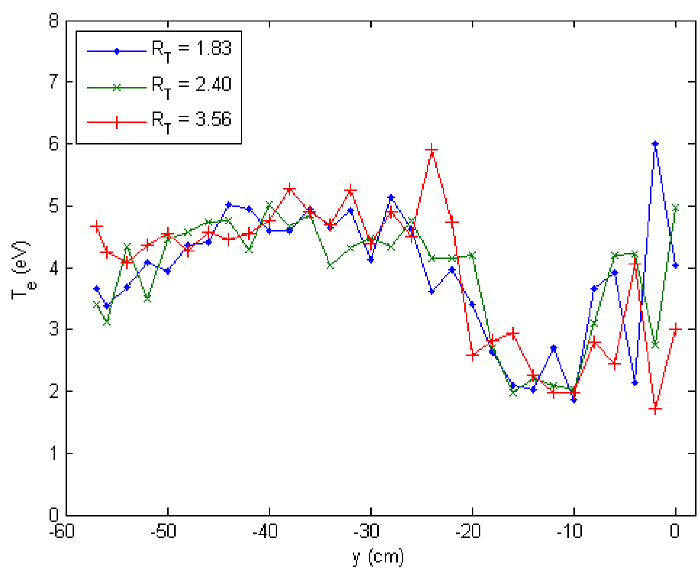

Figure 5.11. Comparison of the centerline electron temperature profile for the three exit mirror magnetic field settings. Error bars were not shown to avoid cluttering.

potential was taken to be the bias voltage at which the derivative dI_e/dV_B reaches a maximum, corresponding to the 'knee' in the I-V trace. The second method used took the plasma potential to be the voltage at which linear curve fits to the electron retarding and saturation regions intersect in the $\ln I_e$ vs. V_B plot. The values obtained from both methods were then compared to ensure consistency. The inverse slope of the electron retarding region curve fit was then reported for the electron temperature, while the intersection voltage was reported for the plasma potential.

5.3.1 Internal Measurements

Figure 5.12 compares the plasma potential at three magnetic field settings along the centerline locations inside the GDM. In general, the plasma potential was not strongly affected by the exit mirror ratio setting; or, at the very least, the exit mirror ratio settings achieved were not enough to observe a statistically significant change in the

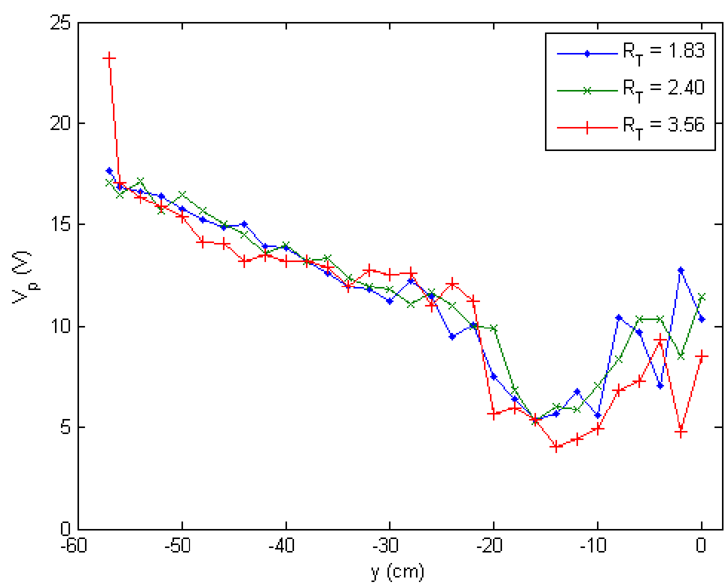

Figure 5.12. Comparison of the centerline plasma potential for the three exit mirror magnetic field settings.

plasma potential. In particular, the profiles for $R_T = 1.83$ and $R_T = 2.40$ agree much more closely with each other than they do with the $R_T = 3.56$ profile. This is consistent with previous observations of the ion number density (Figure 5.5). Furthermore, the plasma potential decreases downstream at a steady rate until we reach the exit mirror, where the potential drops dramatically. This could be an indication that the accelerating electric field in the vicinity of the exit mirror was created by the ambipolar potential, as described by the physics model in Chapter 3.

Finally, Figure 5.13 shows contour plots of the plasma potential inside the GDM for the low and high magnetic field settings. The plots show that the plasma potential mainly varies axially and does not have a strong radial dependence.

5.4 Ambipolar Electric Field

Since the electric field $\vec{E} = -\nabla V_p$, the increased rate of decrease of the plasma potential (decreasing $\left|\nabla V_p\right|$) immediately upstream of the exit mirror would cause an increase in the local electric field magnitude $\left|\vec{E}\right|$ in that area. The axial electric field $E_y = \vec{E} \cdot \hat{y}$ caused by the gradient in the plasma potential can be determined by computing the first derivative of the smoothed potential along the axial direction. Figure 5.14 shows the axial profile across different radial positions, while Figure 5.15 shows the 2D contours. The axial electric field is largely independent of the radial location, as can be expected from the mostly uniform radial profiles for the plasma potential and electron temperature. However, it starts to become less uniform immediately downstream of the exit mirror, slightly past the location of the peak magnetic field.

(a)

(b)

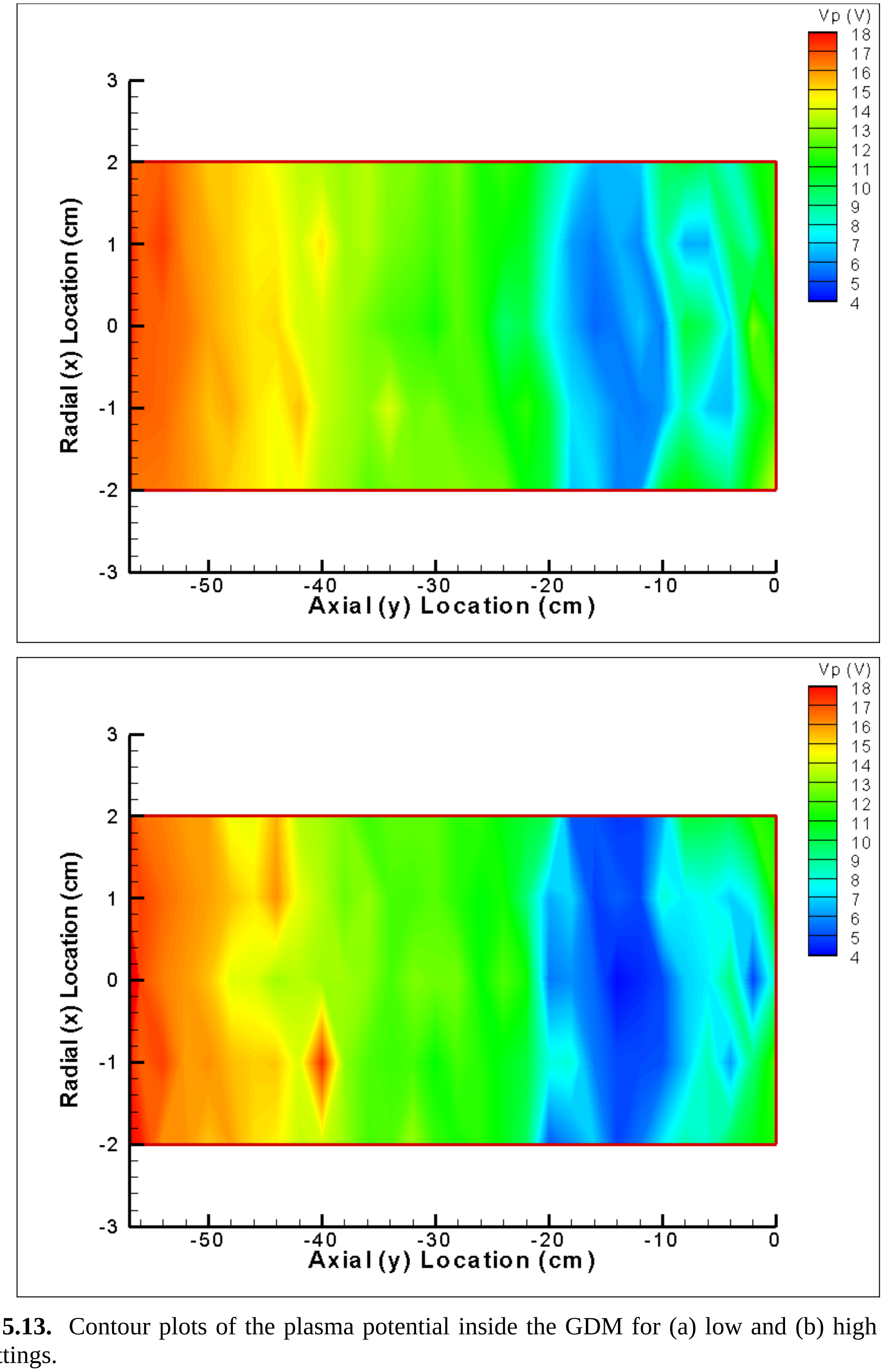

Figure 5.13. Contour plots of the plasma potential inside the GDM for (a) low and (b) high *B* field settings.

(a)

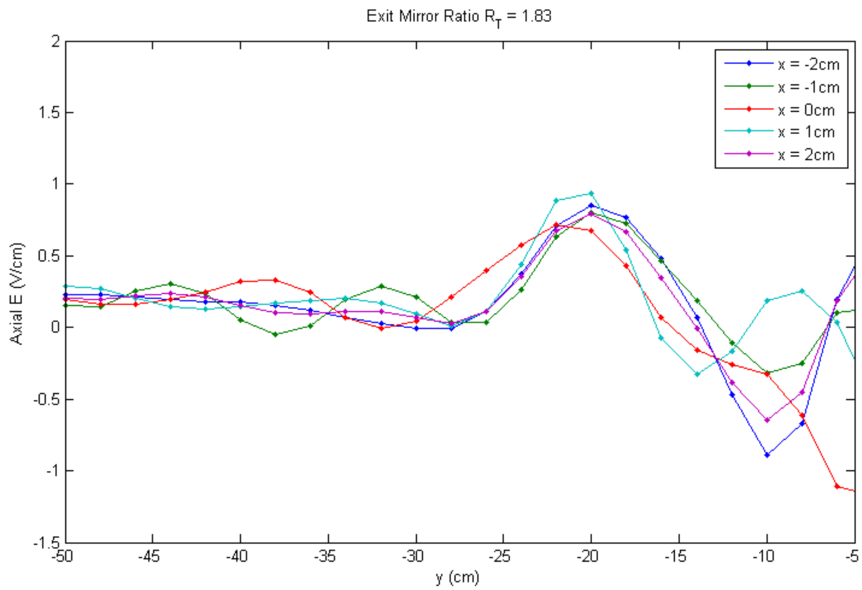

(b)

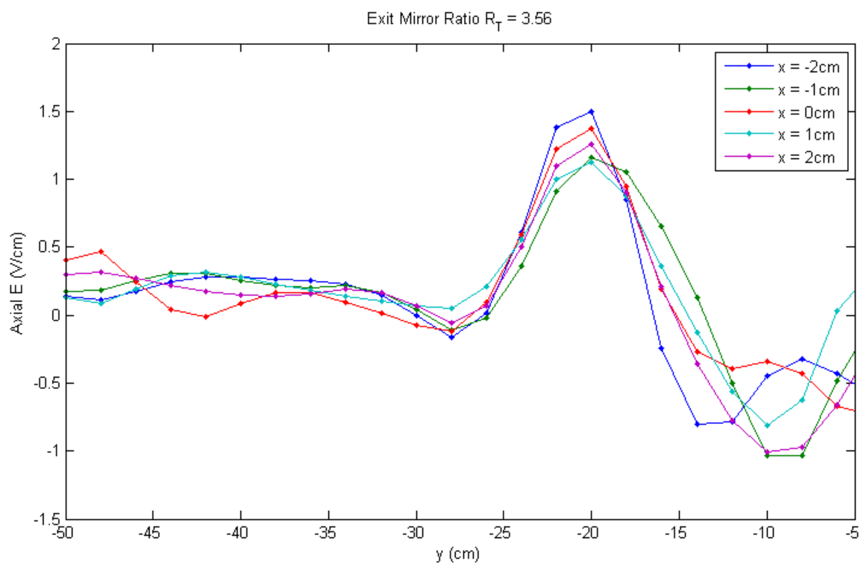

Figure 5.14. Profiles of the local axial electric field inside the GDM for (a) low and (b) high *B* field settings across different radial positions.

(a)

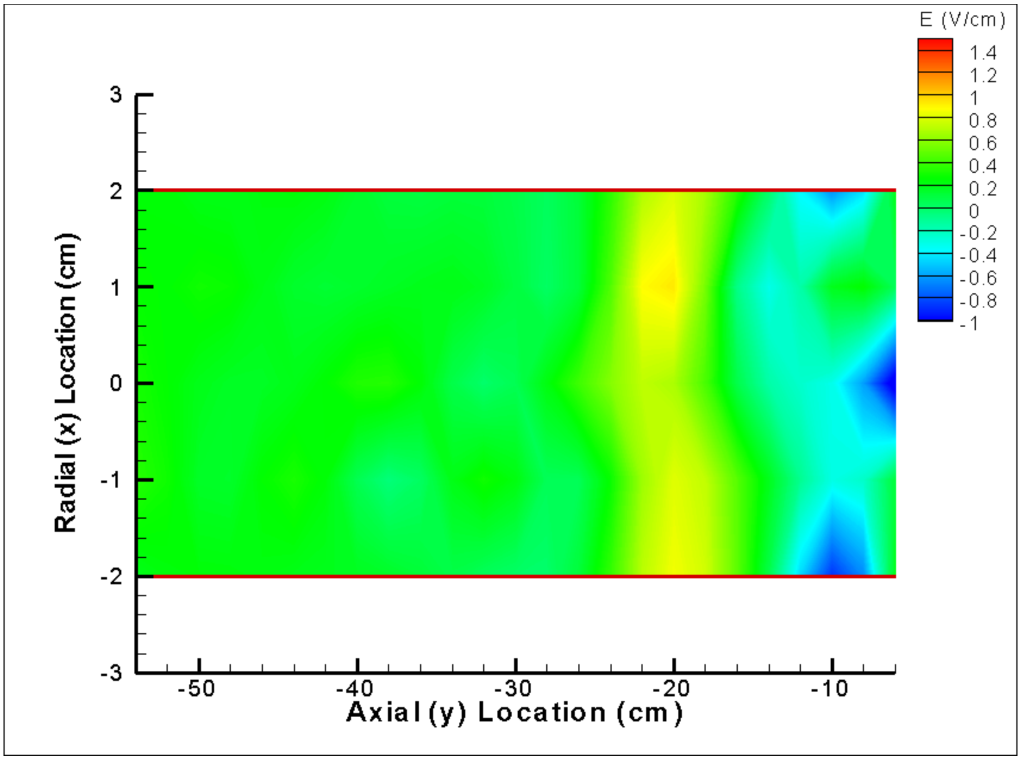

(b)

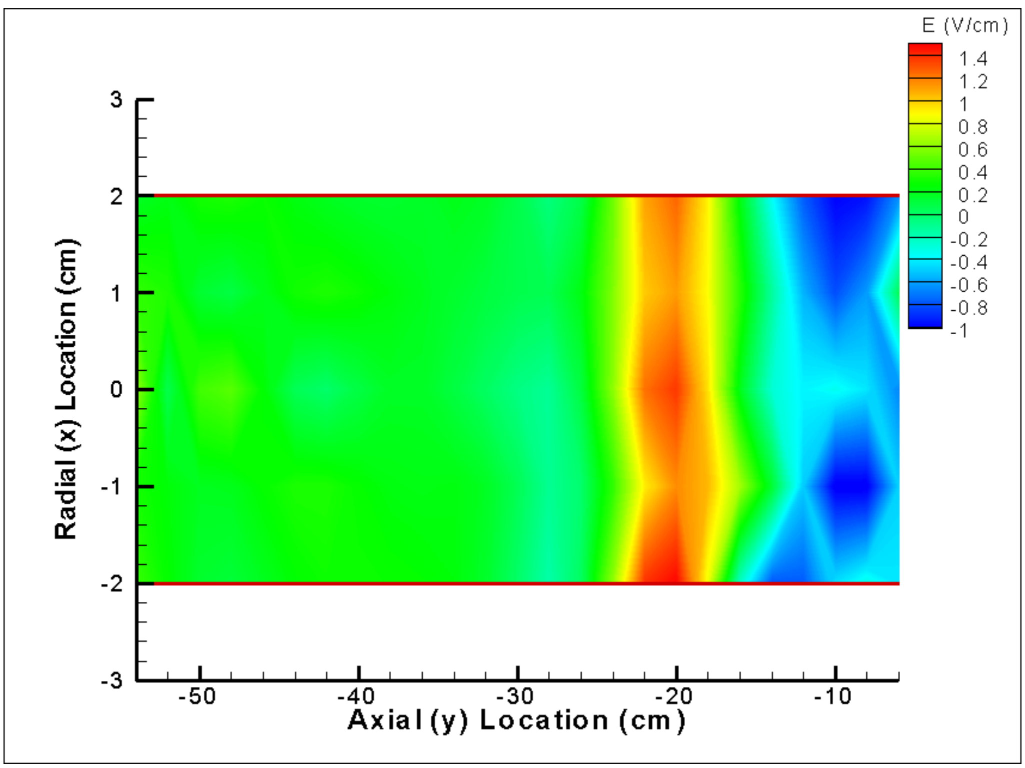

Figure 5.15. Contour plots of the local axial electric field inside the GDM for (a) low and (b) high *B* field settings.

Immediately upstream of the exit mirror, the results show a clear trend of increasing electric field strength in the positive direction (i.e., downstream). As explained in Chapter 3, electrons do not respond to mirror confinement as readily as the ions. As electrons escape the system and leave the ions behind, separation of charges establishes a positive electric field (i.e. pointed downstream). By definition, this electric field can be described by a potential field with a negative gradient, since $\vec{E} \equiv -\nabla\phi = -\nabla V_p$. This charge separation most likely accounts for the sudden additional drop of the plasma potential in this region. The amount of potential drop associated with this electric field is about 8.5 V for the high field setting and 7 V for the low field setting. The peak electric field is higher for the high field setting. These values, however, seem to be too low to directly represent the ambipolar potential, which will be made clear in the next section; however, the relative magnitudes are consistent between the two mirror ratios. The higher the mirror *B* field, the more ions would be trapped, while the electrons would likely not be significantly effected by magnetic field strength. As a result, a higher mirror *B* field causes a larger charge separation, leading to a stronger electric field and a larger plasma potential drop.

5.5 Comparison with GDM Code Results

As the sample output in Appendix A shows, the computational study carried out in this work is more of an overall system study/design based on a physics-based model than a full-blown MHD simulation. As such, it would be impossible to directly compare the experimental results, which yield a 2D map of plasma properties, with the computational results. However, using the appropriate experimental data and supplying them to the GDM code, some system-level comparisons can be performed.

In particular, the code requires the ion density, ion temperature, plasma radius, and the plasma β as inputs. The maximum ion density was taken from the experimental data as the input to the program, while the Pyrex tube radius was taken as the plasma radius. The β value was calculated according to Eq. (2.13), using an average magnetic field magnitude from the experimental setup, assuming quasi-neutrality ($n_e = n_i$), and using an average electron temperature found in the experiments (~4.6 eV). Outputs from the program included the GDM core and mirror magnetic field strengths, and the β value was fine-tuned until the output field strengths and the experimentally measured field strengths were consistent. The ion temperature was unknown, so reasonable values were tried until the program output a plasma length that was consistent with the physical length of the system.

Of the output values produced by the program, of particular interests were plasma parameters such as the electron temperature and the ambipolar potential, since these were ones that could be compared with experimental values. The results are summarized in Table 5.1.

While not exactly identical, the electron temperatures between data and code were in the same order of magnitude. Considering that assumptions and simplifications were necessary in the physics-based model to make the problem tractable, and given the gross approximate nature of the input values to the program, the output electron temperature was fair.

Although the relative magnitude of the plasma potential data for the two mirror ratio settings agrees with the relative magnitude of the ambipolar potential produced by the code, a direct comparison cannot be made. Results from the code suggested that the ambipolar potential for the system should be quite large. However, this was not directly reflected by the values of the measured plasma potential. As a result, conclusions regarding the ambipolar potential cannot be readily drawn. Measurements of the ion energy/velocity distribution using diagnostics such as laser-induced fluorescent (LIF) would be necessary to obtain a more direct comparison.

	$R_T = 1.83$		$R_T = 3.56$	
	Data	Code	Data	Code
n_i (m^{-3})	1.8×10^{17}	1.8×10^{17}	1.5×10^{17}	1.5×10^{17}
T_i (eV)	–	0.16	–	0.13
T_e (eV)	4.6	7.1	4.6	7.35
ϕ (V)	7^*	47.6	8.5^*	49.9

Table 5.1. Comparisons between main experimental and computational results.
*Note that the value listed for experimental data was simply ΔV_p found in Section 5.4.

Chapter 6

Conclusions and Future Work

6.1 Research Summary

The goal of this research was to study a novel propulsion concept called the gasdynamic mirror (GDM). Of particular interests are the plasma dynamics inside such a device, and a physics-based model was developed towards that end. The model is based on electron and ion fluxes in the GDM and takes into account the effects of diffusion due to collisions, as well as the effects of a self-induced electric field on the plasma particles. This electric field is the primary acceleration mechanism of the GDM and is produced by charge separation between the ions and electrons. This charge separation occurs because electrons will initially escape from the system rapidly, leaving behind an excess of ions. This model allows numerical studies of the plasma parameters inside the GDM such as particle energies, confinement times, and magnitude of the ambipolar potential. It also allows one to predict design parameters, such as the plasma length and system mass. Since the GDM was originally proposed as a fusion propulsion concept, the model provides a means to study the physical and performance characteristics of such a system and to assess its merits; it also facilitates a feasibility study of other related GDM concepts, such as a hybrid fusion-fission system.

Although the model focused on a fusion system, the GDM is primarily a plasma confinement and acceleration device. As such, it should have the ability to function as an electrodeless plasma thruster, if an external power source is used to drive the system. If the GDM were ever to be developed, its most likely near term application would be as a plasma thruster. A microwave power source appears to be the perfect candidate for such an application. In particular, ionization and plasma heating is achieved via electron cyclotron resonance heating (ECRH). Energy from the microwave is coupled to the free electrons in the gas. The electrons gain energy and eventually cause the gas to breakdown and form a plasma.

In order to study the ECR-GDM concept and characterize an ECR plasma inside the GDM, a microwave source was assembled and a proof-of-concept model of the GDM was built at the Plasmadynamics and Electric Propulsion Laboratory (PEPL) at the University of Michigan. The primary goal of the experiments were to map out the plasma density and temperature profiles inside the GDM, in an attempt to validate the GDM concept. The magnetic circuit used in these experiments was designed to produce a maximum magnetic field strength of over 1 kG in the upstream mirror, a uniform central field of approximately 250 G, and a downstream exit mirror field with a maximum of about 850 G. Testing was done with an input microwave power of around 700-800 W. Langmuir probe data showed that the ion (argon) number density exceeds 10^{17} m^{-3}, with a relatively uniform electron temperature between 4-5 eV in the central section of the GDM. However, the maximum density and temperature inside the GDM were believed to be higher than measured, since the diagnostics were not able to reach far enough upstream to probe the ECR zone. The plasma potential profile inside the GDM suggested the existence of an acceleration zone at the exit mirror. This acceleration zone points to the presence of the ambipolar potential that is central to operation of the GDM as a propulsion device.

6.2 Future Work

During testing, attempts were made to study the ion energy distribution at the exit plane using the PEPL micro-RPA (retarding potential analyzer). However, attempts were unsuccessful – we were unable to obtain the proper RPA traces. One study for the immediate future would be to diagnose and fix the RPA problems by putting it on a theta stage. This would allow for more accurate alignment with the GDM axis, since the RPA can be sensitive to alignment issues. The goal is to quantify the effect of the ambipolar potential on the ion energy distribution, showing whether the ions are being accelerated. Alternatively, laser diagnostics such as laser-induced fluorescent (LIF) could be used to obtain the same data; this would perhaps be preferable, due to the non-intrusive nature and high accuracy of LIF.

Another area of future work is to build a higher-power system with a larger aspect (plasma length-to-radius) ratio. The current system has an aspect ratio of ~8. A large aspect ratio is desirable in order to prevent MHD instability. Although this is not critical when operating the GDM as a plasma thruster, a high aspect ratio is essential when operating the GDM as a self-sustaining fusion device. Flute instabilities resulting from a low aspect ratio can cool the plasma due to wall heating and therefore extinguish the fusion reaction. Having a larger aspect ratio device would also open up the possibility of studying confinement in the GDM.

As for the system power, currently the microwave source can output a maximum of 1.5 kW to 2 kW. However, a maximum of 800 W was used during testing due to the Pyrex used for the plasma container. Using quartz for the plasma container, for instance, would allow higher operating power due to its higher melting point.

An area of improvement that would expand the testing parameter space is to use magnets that are actively cooled. Currently, the magnets are passively cooled by air. Together with the magnet wire gauge, this cooling method limits the amount of current that can be applied and, hence, the magnetic field strength that can be achieved. In order to compensate for this, a steel housing and endcaps were used in the magnet design to enhance the field. By having an actively cooled system, a substantially higher magnetic field and hence a higher mirror ratio can be achieved. The mirror ratio plays an important role in the confinement characteristics of the GDM. This would also offer a wider range of mirror ratios for investigation in order to validate the physics-based model for the GDM.

Furthermore, the presence of a steel endcap at the exit of the current device closes the magnetic field lines and drastically decreases the magnetic field strength downstream from the exit. This would likely have an adverse effect on the 'nozzle' characteristics of the device and affect the plasma downstream, preventing the study of the device's performance characteristics. This could be one possible cause for the micro-RPA not yielding proper traces, as the effect of the steel endcap on the magnetic field profile downstream from the GDM could ultimately affect the plasma.

Future research can also focus more on building a device that is more amenable to performance study. The current set up was aimed at understanding an ECR plasma, as well as laying the groundwork for understanding the operation of a GDM and validating some of its key concepts. We did not have a "thruster" in mind when building the system. Once a better fundamental understanding is acquired, the next step would be to build a GDM thruster with a magnetic nozzle so that better study of its performance as a thruster could be carried out.

High plasma density and temperature are key aspects to making the GDM plasma thruster competitive, especially when compared with other RF-powered thruster concepts. A helicon thruster employing a helicon source, for instance, would be capable of sustaining a plasma density on the order of 10^{16}-10^{18} m^{-3} with an electron temperature in the range of 5 to 10 eV. A GDM employing a 2.45 GHz microwave source can achieve similar plasma characteristics, as the results of this work showed. However, the advantage of the GDM is that it is not limited to the plasma characteristics observed in this work. As long as the magnets can produce the required magnetic field strength for ECRH, higher frequency microwave can be used with little to no expected difficulty. Since higher frequency can lead to a higher density plasma, a GDM driven by higher frequency microwave, such as 5.8 GHz or even 10 GHz, can potentially produce a much higher plasma density and temperature than other RF-powered thrusters. In this regard, the GDM is highly scalable. Future research can study how microwave frequency affects performance by building a GDM thruster with a high enough upstream mirror magnetic field strength to employ microwave sources of different frequecies.

Appendix A

Sample Output from the GDM Code

In the program, the designation "1" and "2" refer to the upstream (direct converter end) and exit (thrusting end) mirrors of the GDM, respectively. In the sample output below, the smaller confinement times of the exit mirror reflect the lower exit mirror ratio compared to the upstream mirror ratio.

```
INPUT PARAMETERS:
---------------------------------------------------------------------------
Ion Mass            =  2.500 amu
Ion Charge State    =  1.000              Power Plant Eff            =  0.000
Plasma Density      =  1.000E+17 per cc   Wall Reflectivity          =  0.900
Ion Temperature     = 10.00000   keV      Injection Eff              =  1.000
Plasma Radius       =  5.0000    cm       Rad Fraction Inj Power     =  0.000
Shield-Magnet Gap   = 10.0000 cm          Plasma Mirror Ratio 1      = 50.000
Shield Thickness    = 42.0000 cm          Plasma Mirror Ratio 2      = 25.000
Halo Thickness      = 10.0000 cm          Thermal Converter Eff      =  0.300
Sigma-V Average     =  1.128E-16 cc/sec   Fraction to Direct Conv    =  0.352
One Way Trip Dist   =  7.800E+12 cm       Plasma Beta Value          =  0.950
Antiproton Density  =  0.000E+00          Direct Conversion Eff      =  0.800

CALCULATED PARAMETERS:
---------------------------------------------------------------------------
Electron Temperature      =  7.78379   keV    Gain Factor  Q =    2.425E+00
Electrostatic Potential   = 29.44451   keV    Plasma Length =   179.8148 m
Ion Confinement 1  =   9.102E-03 sec     Ion Confinement 2 =    4.551E-03 sec
Ambipolar Confinement 1 = 7.609E-03 sec Ambipolar Confinement 2 = 4.145E-03 sec
Ion Escape Energy 1   =  19.18016   keV  Ion Escape Energy 2   =  19.55347   keV
Electron Escape Energy    = 60.70507   keV
Injection Energy          = 54.90267   keV
Injection Source          =  3.727E+19 per cc per sec
Plasma Volume             =  1.412E+06 cc
Source * Volume           =  5.263E+25 per sec
Fusion Alpha Energy:
  Fraction to Ions = 0.13419    to Electrons = 0.86581
```

Injected Ion Energy:
Fraction to Ions = 0.92621 to Electrons = 0.07379
Magnetic Fields (Tesla):

Core Vacuum	= 20.57397	Core Plasma	= 4.60048
Mirror Vacuum 1	= 230.34532	Mirror Plasma 1	= 230.02399
Mirror Vacuum 2	= 115.65333	Mirror Plasma 2	= 115.01199
Antiproton Trap	= 0.00000		

Vacuum Mirror Ratio 1 = 11.1960 Vacuum Mirror Ratio 2 = 5.6213
Mean Free Path = 1.253E+03 cm
Mean Free Path/(R1*Length) = 1.394E-03 Mean Free Path/(R2*Length) = 2.787E-03
Larmor Radius = 5.604E-01 cm Plasma Radius/Larmor Radius = 8.923E+00

POWERS:	Per Unit Volume	Total
Fusion/Preheat	= 1.331E+01	
Preheat Power	= 3.727E+20 keV/cc-sec	= 8.432E+04 MW
Total Injected Power	= 2.046E+21 keV/cc-sec	= 4.629E+05 MW
Added Injection Power	= 0.000E+00 keV/cc-sec	= 0.000E+00 MW
Recirculated Power	= 2.046E+21 keV/cc-sec	= 4.629E+05 MW
Fusion Power	= 4.961E+21 keV/cc-sec	= 1.122E+06 MW
Bremsstrahlung Power	= 3.181E+19 keV/cc-sec	= 7.196E+03 MW
Synchrotron Rad Power	= 2.035E+19 keV/cc-sec	= 4.603E+03 MW
Neutron Power	= 3.969E+21 keV/cc-sec	= 8.980E+05 MW
Alpha Power	= 9.923E+20 keV/cc-sec	= 2.245E+05 MW
Power to Direct Convert	= 1.050E+21 keV/cc-sec	= 2.375E+05 MW
Thrust Power	= 1.936E+21 keV/cc-sec	= 4.381E+05 MW
Net Electric Power	= 0.000E+00 keV/cc-sec	= 0.000E+00 MW

ROCKET:

Specific Impulse Isp	= 2.007E+05 sec	Thrust	= 2.783E+05 N
GDM Reactor Mass	= 1410.00 Mg	Thermal Conv Mass	= 1128.00 Mg
Injector Mass	= 581.54 Mg	Direct Conv Mass	= 550.35 Mg
Sum (= Engine Mass)	= 1991.54 Mg	Radiator Mass	= 9950.55 Mg
Power Reactor Mass	= 0.00 Mg	Payload Mass	= 0.00 Mg
Antiproton Trap Mass	= 0.000E+00 Mg	Total Vehicle Mass	= 13620.44 Mg
1-way Propellant	= 558.46 Mg	1-way IMLEO	= 14178.89 Mg
1-way Trip Time	= 45.68 days	Round Trip Time	= 92.28 days

Bibliography

1. Hill, P.G. and Peterson, C.R., *Mechanics and Thermodynamics of Propulsion*, Prentice Hall, Upper Saddle River, NJ, 1991.

2. Sutton, G.P. and Biblarz, O., *Rocket Propulsion Elements*, 7th Ed., John Wiley & Sons, Inc., New York, 2001.

3. Frisbee, R.H., "Advanced Space Propulsion for the 21st Century," *Journal of Propulsion and Power*, Vol. 19, No. 6, 2003, pp. 1129-1154.

4. Jahn, R.G., *Physics of Electric Propulsion*, McGraw-Hill, New York, 1968.

5. Rayman, M.D., Varghese, P., Lehman, D.H., and Livesay L.L., "Results from the Deep Space 1 Technology Validation Mission," *Acta Astronautica*, Vol. 47, 2000, pp. 475.

6. Kuninaka, H., Nishiyama, K., Funaki, I., Yamada, T., Shimizu, Y., and Kawaguchi, J., "Powered Flight of Electron Cyclotron Resonance Ion Engines on Hayabusa Explorer," *Journal of Propulsion and Power*, Vol. 23, No. 3, 2007, pp. 544-551.

7. Choueiri, E., "Scaling of Thrust in Self-Field Magnetoplasmadynamic Thrusters," *Journal of Propulsion and Power*, Vol. 14, No. 5, 1998, pp. 744-753.

8. Chang Diaz, F.R., "The VASIMR Rocket," *Scientific American*, Vol. 283, No. 5, 2000, pp. 90-97.

9. Chang Diaz, F.R., Squire, J.P., Ilin, A.V., McCaskill, G.E., Nguyen, T.X., Winter, D.S., Petro, A.J., Goebel, G.W., Cassady, L., Stokke, K.A., Dexter, C.E., Carter, M.D., Baity, F.W., Barber, G.C., Goulding, R.H., Sparks, D.O., Schwenterly, S.W., Bengtson, R.D., Breizman, B.N., Jacobson, V.T., Sagdeev, R.Z., Karavasilis, K., Novakovski, S.V., Chan, A.A., Glover, T.W., "The Development of the VASIMR Engine", in *Proceedings of the International Conference on Electromagnetics in Advanced Applications*, Torino, Italy, 1999.

10. Humble, R.W., Henry, G.N., and Larson, W.J., *Space Propulsion Analysis and Design*, McGraw-Hill, New York, 1995.

11. Foster, J.E., Haag, T., Kamhawi, H., Patterson, M., Malone, S., Elliot, F., Williams, G.J., Jr., Sovey, J.S., and Carpenter, C., “The High Power Electric Propulsion (HiPEP) Ion Thruster,” *40th AIAA/ASME/SAE/ASEE Joint Propulsion Conference and Exhibit*, Fort Lauderdale, FL, 2004. AIAA-2004-3812.

12. Racca, G.D., “Capability of Solar Electric Propulsion for Planetary Missions”, *Planetary and Space Science*, Vol. 49, 2001, pp. 1437-1444.

13. White, R.J. and Averner, M. “Humans in Space”, *Nature*, Vol. 409, 2001, pp. 1115-1118.

14. Martinez-Sanchez, M. and Pollard, J.E., "Spacecraft Electric Propulsion – An Overview," *Journal of Propulsion and Power*, Vol. 14, No. 5, 1998, pp. 688-699.

15. Emrich, W.J., Jr., “Plasma Instabilities in the Gasdynamic Mirror Propulsion Experiment,” *40th AIAA/ASME/SAE/ASEE Joint Propulsion Conference and Exhibit*, Fort Lauderdale, FL, 2004. AIAA-2004-3538.

16. Emrich, W.J., Jr., *Plasma Stability Studies of the Gasdynamic Mirror Fusion Propulsion Experiment*, Ph.D. Dissertation, Dept. of Mechanical and Aerospace Engineering, The University of Alabama, Huntsville, AL, 2003.

17. Gott, Y.V., Ioffe, M.S., and Tel’kovskii, V.G., “Nuclear Fusion Supplement,” Vol. 3, 1962, pp. 1045.

18. Kammash, T. and Lee, M. J., “Gasdynamic Fusion Propulsion System for Space Exploration,” *Journal of Propulsion and Power*, Vol. 11, No. 3, 1995, pp. 544-553.

19. Mirnov, V.V. and Ryutov, D.D., “Linear Gasdynamic System for Plasma Confinement,” *Soviet Technical Physics Letters*, Vol. 5, 1979, pp.279.

20. Kammash, T., *Fusion Reactor Physics – Principles and Technology*, Ann Arbor Science Publishers, Inc., Ann Arbor, MI, 1977.

21. Bagryanskij, P.A., Ivanov, A.A., Klesov, V.V., Koz'minykh, Yu.L., Kotel'nikov, I.A., Krasnikov, Yu.I., Podyminogin, A.A., Rogozin, A.I., Roslyakov, G.V., and Ryutov, D.D., “First Experiments on the Gasdynamic Trap,” *Proceedings of the 11th International Conference on Plasma Physics and Controlled Nuclear Fusion Research*, Vol. 3, 1986, pp. 467–476.

22. Nagornyj, V.P., Ryutov, D.D., and Stupakov, G.V., “Flute Instability of Plasma in a Gasdynamic Trap,” *Nuclear Fusion*, Vol. 24, No. 11, 1984, pp. 1421-1438.

23. Zhitlukhin, A.M., Safronov, V.M., Sidnev, V.V., and Skvortsov, Yu.V., “Confinement of a Hot Plasma with $\beta \sim 1$ in an Open Confinement System,” *JETP Letters*, Vol. 39, No. 6, 1984, pp. 293-296.

24. Kammash, T., "Some Approaches to Mass Reduction of the Gasdynamic Mirror Fusion Rocket," *34th AIAA/ASME/SAE/ASEE Joint Propulsion Conference and Exhibit*, Cleveland, OH, 1998. AIAA-1998-3587.

25. Kammash, T. and Flippo, K., "Magnetic Configuration of a Reduced-Mass Gasdynamic Mirror Fusion Propulsion System," *35th AIAA/ASME/SAE/ASEE Joint Propulsion Conference and Exhibit*, Los Angeles, CA, 1999. AIAA-1999-2698.

26. Kammash, T. and Lee, M.J., "Fission-Assisted Or Self-Sustaining Gasdynamic Mirror Propulsion System," *32nd AIAA/ASME/SAE/ASEE Joint Propulsion Conference and Exhibit*, Lake Buena Vista, FL, 1996. AIAA-1996-3066.

27. Lawson, J.D., "Some Criteria for a Power Producing Thermonuclear Reaction," *Proceedings of Physical Society of London*, Section B, Vol. 70, 1957, pp. 1-6.

28. Miley, G.H., Towner, H., and Ivich, N., *Fusion Cross Sections and Reactivities*, University of Illinois Report COO-2218-17, Urbana, IL, 1974.

29. *NRL Plasma Formulary*, Washington, DC, 2007. NRL/PU/6790—07-500.

30. Hofmann, P., Iljinov, A.S., Kim, Y.S., Mebel, M.V., Daniel, H., David, P., von Egidy, T., Haninger, T., Hartmann, F.J., Jastrzebski, J., Kurcewicz, W., Lieb, J., Machner, H., Plendl, H.S., Riepe, G., Wright, B., and Ziock, K., "Fission of Heavy Nuclei Induced by Stopped Antiprotons. I. Inclusive Characteristics of Fission Fragments," *Physical Review C*, Vol. 49, No. 5, 1994, pp. 2555-2568.

31. Kim, Y.S., Iljinov, A.S., Mebel, M.V., Hofmann, P., Daniel, H., von Egidy, T., Haninger, T., Hartmann, F.J., Machner, H., Plendl, H.S., and Riepe, G., "Fission of Heavy Nuclei Induced by Stopped Antiprotons. II. Correlations between Fission Fragments," *Physical Review C*, Vol. 54, No. 5, 1996, pp. 2469-2476.

32. Bocquet, J.P., Malek, F., Nifenecker, H., Rey-Campagnolle, M., Maurel, M., Monnand, E., Perrin, P., Ristori, C., Ericsson, G., Johansson, T., Tibell, G., Polikanov, S., Krogulski, T., and Mougey, J., "Prompt Fission Induced by Antiproton Annihilation At Rest on Heavy Nuclei," Z. Phys. A – Hadrons and Nuclei, Vol. 342, No. 2, 1992, pp. 183-189.

33. Morgan, D.L., Jr., "Annihilation Localization in Gas-Core and Plasma-Core Annihilation Rocket Engines," *Acta Astronautica*, Vol. 21, No. 1, 1990, pp. 23-27.

34. Jackson, G., "Antiproton Powered Fusion Propulsion System," Technical Communication, Hbar Technologies, LLC, 2005.

35. Frank, F.C., "Hypothetical Alternative Energy Sources for the Second Meson Events," *Nature*, Vol. 160, No. 4068, 1947, pp. 525-527.

36. Alvarez, L.W., Bradner, H., Crawford, F.S., Jr., Crawford, J.A., Falk-Vairant, P., Good, M.L., Gow, J.D., Rosenfeld, A.H., Solmitz, F., Stevenson, M.L., Ticho, H.K., and Tripp R.D., "Catalysis of Nuclear Reactions by μ Mesons," *Physics Review*, Vol. 105, 1957, pp. 1127-1128.

37. Zel'dovich, Y.B. and Sakharov, A.D., "Reactions Produced by μ-Mesons in Hydrogen," *Soviet Physics, JETP*, Vol. 5, 1957, pp. 775-777.

38. Jackson, J.D., "Catalysis of Nuclear Reactions between Hydrogen Isotopes by μ^- Mesons," *Physics Review*, Vol. 106, 1957, pp. 330-339.

39. Jones, S.E., Anderson, A.N., Caffrey, A.J., Van Siclen, C.DeW., and Watts, K.D., "Observation of Unexpected Density Effects in Muon-Catalyzed D-T Fusion," *Phys. Rev. Lett.*, Vol. 56, No. 6, 1986, pp. 588-591.

40. Petrov, Y.V., "Conceptual Scheme of a Hybrid Mesocatalytic Fusion Reactor," translated from *Atomnaya Energiya*, Vol. 63, No. 5, 1987, pp. 333-341.

41. Kammash, T. and Tang, R., "Muon-Boosted Fusion Propulsion System," *43rd AIAA/ASME/SAE/ASEE Joint Propulsion Conference and Exhibit*, Cincinnati, OH, 2007. AIAA-2007-5609.

42. Rose, D. J. and Clark, M., *Plasma and Controlled Fusion*, John Wiley & Sons, Inc., New York, NY, 1961, pp. 66.

43. Lieberman, M.A. and Lichtenberg, A.J., *Principles of Plasma Discharges and Materials Processing*, John Wiley & Sons, Inc., New York, NY, 1994.

44. Allis, W.P., Buchsbaum, S.J., and Bers, A., *Waves in Anisotropic Plasmas*, MIT Press, Cambridge, MA, 1963.

45. Gerling, J.F., "Waveguide Components and Configurations for Optimal Performance in Microwave heating Systems," Technical Document, Gerling Applied Engineering, Inc., 2000. http://www.2450mhz.com.

46. Laverghetta, T.S., *Handbook of Microwave Testing*, Artech House, Inc., Dedham, MA, 1981.

47. Bathker, D.A., "A Stepped Mode Transducer Using Homogeneous Waveguides," *IEEE Transactions on Microwave Theory and Techniques*, Vol. 15, No. 2, 1967, pp. 128-130.

48. Mott-Smith, H.M. and Langmuir, I., "The Theory of Collectors in Gaseous Discharges," *Physical Review*, Vol. 28, No. 4, 1926, pp. 727-763.

49. Langmuir, I., “The Interaction of Electron and Positive Ion Space Charges in Cathode Sheaths,” *Physical Review*, Vol. 33, No. 6, 1929, pp. 954-989.

50. Hutchinson, I.H., *Principles of Plasma Diagnostics*, Cambridge University Press, New York, NY, 2002.

51. Chen, F.F., “Electric Probes,” in *Plasma Diagnostic Techniques*, Academic Press, 1965, pp. 113-200.

52. Laframboise J. and Parker, L., “Probe Design for the Orbit-Limited Current Collection,” *Journal of Fluids*, Vol. 6, 1973, pp. 629-636.

53. Laframboise, J. and Rubinstein, J., “Theory of a Cylindrical Probe in a Collisionless Magnetoplasma,” *Journal of Fluids*, Vol. 19, 1976, pp. 1900-1908.

54. Hershkowitz, N., “How Langmuir Probes Work,” in *Plasma Diagnostics*, Academic Press, 1989, pp. 113-183.

55. Swift, J.D. and Schwar, M.J.R., *Electrical Probes for Plasma Diagnostics*, American Elsevier Publishing, New York, NY, 1970.

56. Lobbia, Robert B., *A Time-resolved Investigation of the Hall Thruster Breathing Mode*, Ph.D. Dissertation, Dept. of Aerospace Engineering, The University of Michigan, Ann Arbor, MI, 2010.